8& %HUNHOH\

8& %HUNHOH\ (OHFWURQLF 7KHVHV DQG 'LVVHUWDWL

7LWOH
3KDVH 6WDELOLW\ DQG 7UDQVIRUPDWLRQV LQ 9DQDGLXP 2[LGH 1D

3HUPDOLQN
KWWSV HVFKRODUVKLS RUJ XF LWHP ZK M[

$XWKRU
%HUJHUXG $P\ -R

3XEOLFDWLRQ 'DWH

3HHU UHYLHZHG_7KHVLV GLVVHUWDWLRQ

Phase Stability and Transformations in Vanadium Oxide Nanocrystals

By

Amy Jo Bergerud

A dissertation submitted in partial satisfaction of the

requirements for the degree of

Doctor of Philosophy

in

Engineering - Materials Science and Engineering

in the

Graduation Division

of the

University of California, Berkeley

Commitee in charge:

Professor Delia Milliron, Co-Chair
Professor Junqiao Wu, Co-Chair
Professor Mark Asta
Professor Michael Crommie

Summer 2016

Phase Stability and Transformations in Vanadium Oxide Nanocrysals

by

Amy Jo Bergerud

Doctor of Philosophy in Materials Science and Engineering

University of California, Berkeley

Professor Delia Milliron, Co-Chair

Professor Junqiao Wu, Co-Chair

Vanadium oxides are both fascinating and complex, due in part to the many compounds and phases that can be stabilized as well as the phase transformations which occur between them. The metal to insulator transitions (MITs) that take place in vanadium oxides are particularly interesting for both fundamental and applied study as they can be induced by a variety of stimuli (*i.e.*, temperature, pressure, doping) and utilized in many applications (*i.e.*, smart windows, sensors, phase change memory). Nanocrystals also tend to demonstrate interesting phase behavior, due in part to the enhanced influence of surface energy on material thermodynamics. Vanadium oxide nanocrystals are thus expected to demonstrate very interesting properties in regard to phase stability and phase transformations, although synthesizing vanadium oxides in nanocrystal form remains a challenge.

Vanadium sesquioxide (V_2O_3) is an example of a material that undergoes a MIT. For decades, the low temperature monoclinic phase and high temperature corundum phase were the only known crystal structures of V_2O_3. However, in 2011, a new metastable polymorph of V_2O_3 was reported with a cubic, bixbyite crystal structure. In Chapter 2, a colloidal route to bixbyite V_2O_3 nanocrystals is presented. In addition to being one of the first reported observations of the bixbyite phase in V_2O_3, it is also one of the first successful colloidal syntheses of any of the vanadium oxides. The nanocrystals possess a flower-like morphology, the size and shape of which are dependent on synthesis time and temperature, respectively. An aminolysis reaction mechanism is determined from Fourier transform infrared spectroscopy data and the bixbyite crystal structure is confirmed by Rietveld refinement of X-ray diffraction (XRD) data. Phase stability is assessed in both air and inert environments, confirming the metastable nature of the material. Upon heating in an inert atmosphere above 700°C, the nanocrystals irreversibly transform to the bulk stable corundum phase of V_2O_3 with concurrent particle coarsening. This, in combination with the enhanced stability of the nanocrystals over bulk, suggests that the bixbyite phase may be stabilized due to surface energy effects, a well-known phenomenon in nanocrystal research.

In Chapter 3, the reversible incorporation of oxygen in bixbyite V_2O_3 is reported, which can be controlled by varying temperature and oxygen partial pressure. Based on XRD and

thermogravimetric analysis, it is found that oxygen occupies interstitial sites in the bixbyite lattice. Two oxygen atoms per unit cell can be incorporated rapidly and with minimal changes to the structure while the addition of three or more oxygen atoms destabilizes the structure, resulting in a phase change that can be reversed upon oxygen removal. Density functional theory (DFT) supports the reversible occupation of interstitial sites in bixbyite by oxygen and the 1.1 eV barrier to oxygen diffusion predicted by DFT matches the activation energy of the oxidation process derived from observations by *in situ* XRD. The observed rapid oxidation kinetics are thus facilitated by short diffusion paths through the bixbyite nanocrystals. Due to the exceptionally low temperatures of oxidation and reduction, this material, made from earth-abundant atoms, is proposed for use in oxygen storage applications, where oxygen is reversibly stored and released.

Further oxidation of bixbyite V_2O_3 under controlled oxygen partial pressure can lead to the formation of nanocrystalline vanadium dioxide (VO_2), a material that is studied for its MIT that occurs at 68°C in the bulk. This transformation is accompanied by a change in crystal structure, from monoclinic to rutile phase, and a change in optical properties, from infrared transparent to infrared blocking. Because of this, VO_2 is promising for thermochromic smart window applications, where optical properties vary with temperature. Recently, alternative stimuli have been utilized to trigger MITs in VO_2, including electrochemical gating. Rather than inducing the expected monoclinic to rutile phase transition as originally proposed, electrochemical gating of the insulating phase was recently shown to induce oxygen vacancy formation in VO_2, thereby inducing metallization, while the characteristic V-V dimerization of the monoclinic phase was retained. In Chapter 4, the preparation and electrochemical reduction of VO_2 nanocrystal films is presented. The nanocrystalline morphology allows for the study of transformations under conditions that enhance the gating effect by creating a large VO_2-electrolyte interfacial area and by reducing the path length for diffusion. The resulting transitions are observed optically, from insulator to metal to insulator and back, with *in situ* visible-near infrared spectroelectrochemistry and correlated with structural changes monitored by Raman and X-ray absorption spectroscopies. The never-before-seen transition to an insulating phase under progressive electrochemical reduction is attributed to an oxygen defect induced phase transition to a new phase. This is likely enabled by the nanocrystalline nature of the sample, which may enhance the kinetics of oxygen diffusion, support a higher degree of lattice expansion-induced strain, or simply alter the thermodynamics of the system.

I would first like to thank my advisor Delia for being a great teacher and role model, for allowing me pursue what interested me, even though the first few years were a bit rough, and to help me see the big picture when I got too caught up in the details. Your vision and drive are truly an inspiration!

Next, I'd like to thank all of the members of the Milliron group that I've worked with over the years. I'd especially like to thank Raffa for being a wonderful mentor and kitty-matchmaker. To Evan, who's been with me since the beginning, thanks for being a great co-worker, classmate, trivia partner, and friend. To Gary- you've been a great ACG hoodmate and a true friend. To Clay and Rob, Sebastien, Memo, Anna, Natacha, Lauren, Gabriel, Ajay, and the rest of the past and present students and post docs in the group- thanks for the friendship, interesting conversations, and cool science.

To my friends in Berkeley- Sibel, Felicia, Paul, Kyle, Seth, Hermann, and Joel- thanks for making grad school so much fun!

I'd also like to extend my thanks to the rest of my dissertation committee- Junqiao Wu, Michael Crommie, and Mark Asta.

Tusen Takk to Sverre, Sandra and everyone else at NTNU that helped me during my time in Norway- I really enjoyed meeting all of you and learning DFT!

To my family- Mom, Dad, and Chrissy- thank you for being so supportive throughout my life. I wouldn't have gotten to this point without your encouragement.

Last, but certainly not least, I want to acknowledge my husband, Ben. Thank you so much for believing in me, for following me to California then Texas, for taking care of me when I was sick, and keeping my spirits up when school and research seemed impossible. I couldn't have done it without you.

1.1.1 Motivation

Solid-solid phase transformations play a pivotal role in many applications. These range from the martensite-to-austenite transformation in nickel titanium alloys for shape memory applications to the amorphous-to-crystalline transformation of germanium antimony telluride for non-volatile phase change memory to lithium intercalcation in battery electrodes for energy storage. Clearly, understanding and controlling the thermodynamics and kinetics of such transformations is important for their use in application. The transformations that occur in the oxides of vanadium are particularly interesting due to the rich and complex nature of the vanadium oxygen system. Because of the many oxidation states and coordination environments available to vanadium, there exist many vanadium oxide compounds in the vanadium-oxygen phase diagram, as shown in Figure 1.1.[1] Furthermore, a given compound can have several stable and metastable phases depending on extrinsic factors such as temperature, pressure, doping, and size. Several vanadium oxides, including V_2O_3 and VO_2, are known to undergo metal-to-insulator transformations (MITs).[2] These transformations are often accompanied by a change in structure, magnetic, or optical properties. For this reason, these MITs are promising for applications such as sensors, phase change memory, and smart windows.[3–7]

1.1.2 Vandium Dioxide

VO_2 is an example of a vanadium oxide which undergoes a MIT.[2] Below 68°C, the insulating, monoclinic phase is stable, while above this temperature, the metallic, rutile phase is stable.[8,9] Structurally, these two polymorphs are quite similar, as shown in Figure 4.5 in Chapter 4, with vanadium atoms evenly spaced along the c-axis in the rutile phase and dimerized in the monoclinic phase, leading to a doubling in the size of the unit cell. Whether this structural transformation triggers the insulating behavior of VO_2 at low temperatures, as expected for a Peierls insulator, or electron correlation effects dominate, as with a Mott-Hubbard insulator, is still subject to extensive debate.[10–12]

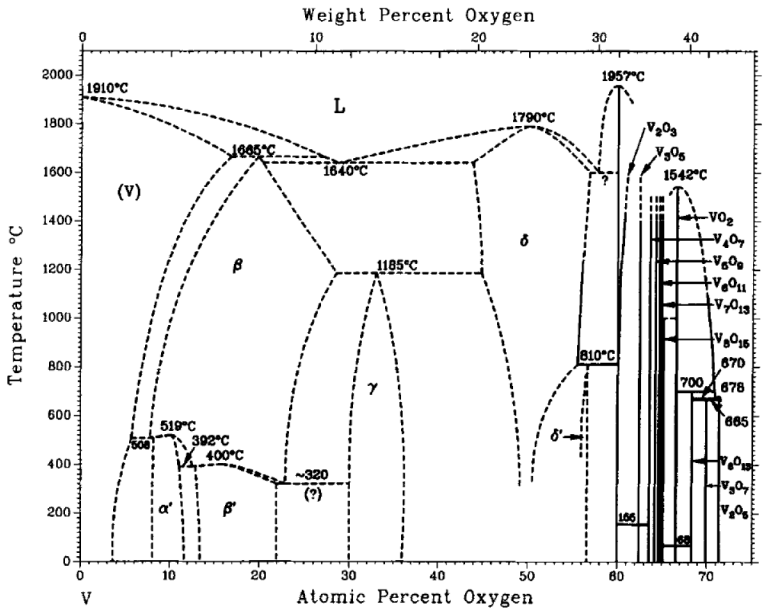

Figure 1.1: Vanadium-Oxygen phase diagram. Adapted from Wriedt.[1]

The MIT temperature in VO_2 can be tuned via the application of strain or the presence of dopants, such as tungsten or magnesium, thus making it promising for applications requiring switchable properties near room temperature.[13–15] One such application is thermochromic windows coatings.[6] In the metallic state, VO_2 absorbs infrared (IR) light while in the insulating state, IR light is transmitted. In this way, the transmittance of IR light (and thus, heat) can be controlled such that it is blocked at high temperatures and allowed to pass through at low temperatures.

In addition to the stable monoclinic and rutile polymorphs, there exists many metastable phases of VO_2. Another insulating monoclinic phase (M2), in which half the vanadium atoms are dimerized, has been observed as an intermediate between monoclinic and rutile during the MIT.[16–18] The monoclinic VO_2-B phase is studied for use as a battery electrode due to its ability to reversibly intercalate lithium ions.[19,20] Additionally, there have been reports of a tetragonal (A) phase, a third monoclinic (M3) phase, and a triclinic (T) phase of VO_2.[19,21,12]

1.1.3 Vanadium Sesquioxide

V_2O_3 is another vanadium oxide which undergoes a MIT accompanied by a phase transformation. At temperatures below 170 K, an antiferromagnetic, insulating phase with a monoclinic crystal structure is stable. Above this temperature, the paramagnetic and metallic corundum phase is stable.[2,22,23] Like VO_2, the MIT temperature in V_2O_3 is sensitive to the presence of dopants and the application of pressure, as shown in Figure 1.2. Indeed, increased pressure, titanium doping, or the presence of excess oxygen have all been shown to decrease MIT temperature.[24–26] Furthermore, a MIT can be induced without the accompanied change in phase when chromium dopants are present, resulting in the stabilization of an insulating, corundum phase.[27] This is considered to be textbook example of a Mott transition, and thus, V_2O_3 is a system of great interest in condensed matter physics.[28]

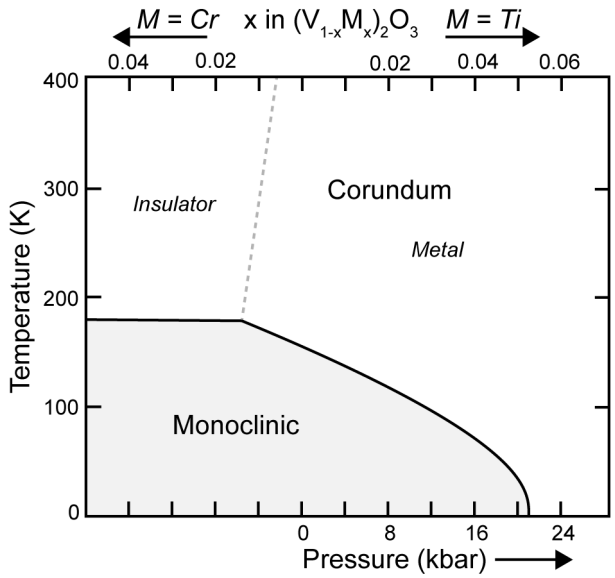

Figure 1.2: Pressure-temperature phase diagram of V_2O_3. Adapted from McWhan *et al.*[24]

For many decades, the monoclinic and corundum phases were the only known polymorphs of V_2O_3. Recently, however, a new phase with a cubic bixbyite crystal structure was observed.[29] This new phase is the subject of the majority of this dissertation, with an emphasis on its mechanism of phase stabilization (Chapter 2) and the interesting properties and useful phase transformations (Chapter 3) that are observed in bixbyite nanocrystals.

1.2.1 Phase Stability in Bulk Materials

The stable phase of a system is determined by its Gibbs free energy, G, a function of the temperature and pressure of a system:

$$G = H - TS \tag{1.1}$$

Where T is temperature, S is entropy, a measure of disorder in the system, and H is enthalpy, a measure of the heat content of a system, which is defined as:

$$H = E + PV \tag{1.2}$$

Where E is internal energy, P is pressure, and V is volume.

A phase is said to be in stable equilibrium at a given temperature and pressure when Gibbs free energy is minimized and the following is satisfied such that there is no driving force for the system to change state,

$$dG = 0 \tag{1.3}$$

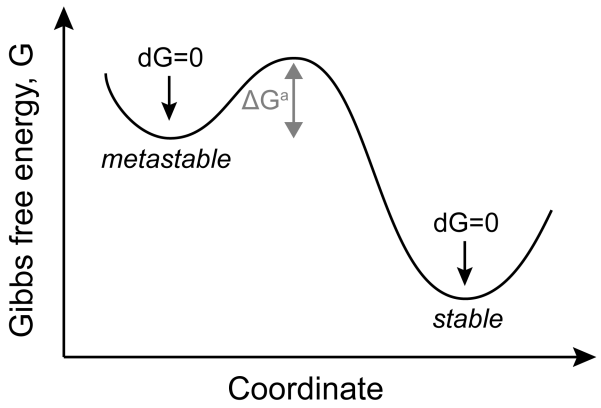

Figure 1.3: Cartoon demonstrating global and local minima in Gibbs free energy, indicating stable and metastable state, respectively.

When equation 1.3 is satisfied but Gibbs free energy is not minimized on a global scale, the system is said to be in a metastable state. This is demonstrated in Figure 1.3. A state is said to be unstable when $dG \neq 0$, and thus, will only exist transiently.

1.2.2 Phase Transformations in Bulk Materials

A phase transformation is possible when it results in a lowering of Gibbs free energy, such that:

$$\triangle G = G_{\mathsf{final}} – G_{\mathsf{initial}} < 0 \tag{1.4}$$

Where ΔG is the change in Gibbs free energy and driving force for transformation. Although equation 1.4 can be used to determine whether a transformation is energetically favorable, it does not describe the kinetics of the transformation. As the system transitions from the initial to final state, it must pass through an activated state where Gibbs free energy is greater than that of the initial and final states. This energy barrier can be overcome by thermal fluctuations in the system, and thus, rate of transformation can be described as a function of temperature. This relation is known as the Arrhenius rate equation:

$$rate \propto \exp\left(-\frac{\triangle G^{\mathsf{a}}}{RT}\right) \tag{1.5}$$

Where R is the universal gas constant and ΔG^{a} is activation energy, as shown in Figure 1.3. The likelihood of transition from a metastable to stable state is thus dependent on the activation energy barrier separating the two. Indeed, many metastable phases can persist indefinitely due to high barriers to transformation. Diamond phase carbon is the canonical example of this, which exists at ambient conditions even though graphite phase has a lower Gibbs free energy.

Phase transformations can be categorized according to the Ehrenfest classification, in which a transformation is assigned an order corresponding to the lowest order differential of Gibbs free energy which exhibits discontinuity.[30] Therefore, a first-order phase transition

is discontinuous in the first derivative of Gibbs free energy with respect to temperature or pressure (or in other words, discontinuous in entropy or volume) across a phase boundary whereas a second-order transformation is discontinuous in the second derivative. An example of the former is solidification, where volume changes discontinuously between solid and liquid phases. Examples of latter include conducting-superconducting transitions and ferromagnetic transitions. The solid-solid phase transformations discussed in this dissertation are first-order in nature.

1.2.3 Phase Stability and Transformations in Nano Materials

In nanomaterials, an additional surface energy term must be added to the expression for Gibbs free energy:

$$G = G_{\mathsf{bulk}} + G_{\mathsf{surf}} = H - TS + A\gamma \tag{1.6}$$

Where γ is surface energy, the energy required to form one unit area of new surface, and A is surface area. As the latter is an extensive property, which depends on the size of the system, this equation is usually considered on a per unit volume basis. In bulk materials, the ratio of surface area to volume is low and the G_{surf} term is negligible. However in nano materials, this is not the case and the additional surface term can have a large influence on Gibbs free energy. In some cases, Gibbs free energy in nanomaterials is altered to the extent that the stable bulk phase no longer has the lowest Gibbs free energy and a different polymorph becomes stable. One of the first and most highly cited examples of this is the stabilization of γ-alumina. Reported in 1997 by McHale *et al.*, this low surface energy phase was found to be stable at surface areas greater than 125 m^2/g, while the bulk stable α corundum phase regained stability at surface areas below this value.[31] Since then, size stabilized polymorphs of cobalt, indium oxide, and lead antimony telluride have been reported, highlighting a great advantage of nanocrystals over their bulk counterparts- the opportunity to stabilize phases under conditions in which they are normally not stable.[32–34]

Arguably, the most famous example of a size stabilized polymorph is the metastable anatase phase of titania which can be stabilized at ambient conditions when synthesized in nanocrystal form. Figure 1.4 shows enthalpy[1] as a function of surface area for three phase of titania- rutile, brookite, and anatase. At low surface areas (large particle sizes), the rutile phase is shown to have the lowest enthalpy. However, at large surface areas (small particle sizes), anatase bypasses rutile and brookite phases to become the lowest enthalpy, and therefore stable, phase. This is made possible by the low surface energy of the anatase phase as compared to the other two polymorphs, represented by the slope of the lines in Figure 1.4.

A detailed thermodynamic analysis of nanocrystalline titania was previously performed by Zhang and Banfield.[36] Taking into account bulk Gibbs free energy, surface energy, and

[1]

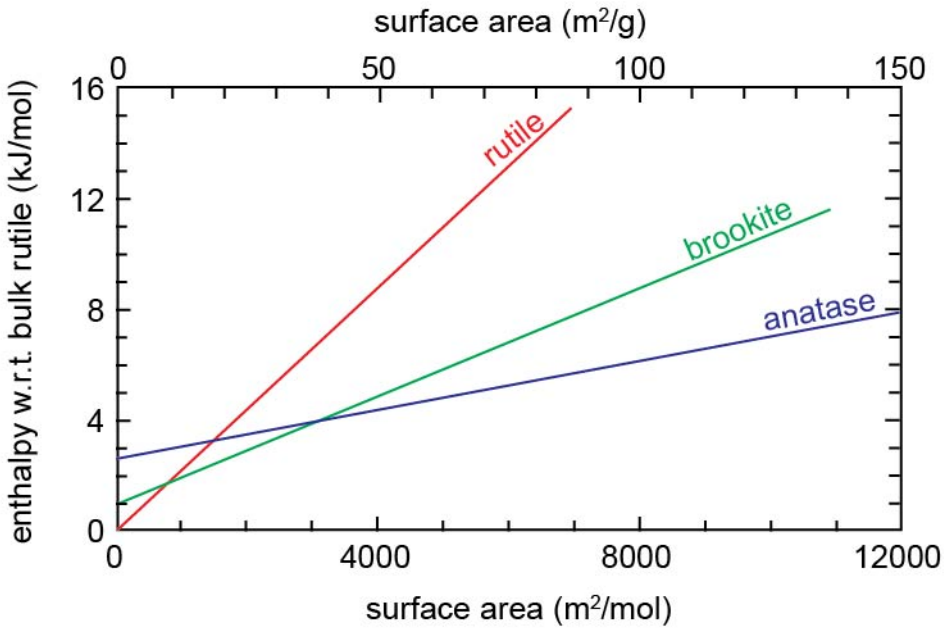

Figure 1.4: Enthalpy as a function of surface area for the three phases of titania: rutile (red), brookite (green), and anatase (blue). Figure adapted from Ranade *et al.*[35]

excess pressure due to curvature, the following expression describing the ΔG of the anatase to rutile transformation was derived:

$$\triangle G = \triangle_{\mathrm{f}} G(T, rutile) - \triangle_{\mathrm{f}} G(T, anatase) + A_{\mathrm{R}}\gamma_{\mathrm{R}} - A_{\mathrm{A}}\gamma_{\mathrm{A}} + \triangle P_{\mathrm{R}} V_{\mathrm{m;R}} - \triangle P_{\mathrm{A}} V_{\mathrm{m;A}} \quad (1.7)$$

Which, through substitution, can be reduced to:

$$\triangle G = \triangle_{\mathrm{f}} G(T, rutile) - \triangle_{\mathrm{f}} G(T, anatase) + (2t+3)\frac{M}{r}\left(\frac{\gamma_{\mathrm{R}}}{\rho_{\mathrm{R}}} - \frac{\gamma_{\mathrm{A}}}{\rho_{\mathrm{A}}}\right) \quad (1.8)$$

With $\triangle_{\mathrm{f}} G(T, phase)$ denoting the Gibbs free energy of formation of the noted phase at temperature T, ρ the density of the phase, M the molar mass of titania, t the ratio of surface stress to surface energy, and r the radius of the nanocrystal. By plugging in known thermodynamic and material constants, setting ΔG to zero, and solving for r, a critical size of stability was calculated to be ~14 nm in diameter, which is in good agreement with experimental observations of phase stability in titania.[37] Unfortunately, a thermodynamic analysis like this is often impossible owing to the difficulty in measuring thermodynamic values such as enthalpy and entropy. However, a few observations can be garnered from the analysis. First, the size stabilized polymorph must have a lower ratio of surface energy to density than the bulk stable polymorph.[2] Second, transformation from one phase to another

[2] 38

requires a change in particle size or surface energy. These ideas will be important in the Chapter 2 of this thesis where it is proposed that bixbyite V_2O_3 is an example of a size stabilized polymorph.

1.3.1 Synthetic Methods

With its many oxidation states and structures and the fact that nanoscaling can alter relative phase stability, vanadium oxide nanocrystals are expected to demonstrate interesting phase behavior. However the factors contributing to vanadium oxide's interesting thermodynamics also have the undesired consequence of making it very difficult to stabilize a specific phase. Careful control of precursor selection, oxygen chemical potential, and temperature is therefore required to obtain the desired product. There are many methods by which nanocrystals are synthesized, several of which have been successfully applied to vanadium oxides. These include physical vapor deposition (PVD) coupled with ion beam lithography or thermal treatment, ion implantation, and hydrothermal synthesis. The first two methods have been utilized to study the size dependence of the MIT in VO_2, but this is invariably influenced by strain associated with the fact that the nanocrystals are confined to the surface of a substrate, as in the case of PVD prepared VO_2,[39,40] or embedded in a matrix, as with ion implantation.[41]

Solution processing is often desired over methods requiring high vacuum for its low cost and scalability. It is also possible to form nanocrystal suspensions or powders via solution methods, thereby facilitating the study of size dependent properties without the influence of a substrate. Vanadium oxide nanocrystals have been prepared by hydrothermal synthesis previously, however, the resulting nanoparticles are often of mixed phase or polydisperse in size, thereby preventing the study of size dependent properties.[42,43]Unfortunately, this technique is a "black box" in that it is nearly impossible to know how the reaction proceeds, and thus, difficult to know which factors to tune in order to achieve a monodisperse, phase pure product. Thus, a more tunable method is required to prepare monodisperse vanadium oxide in nanocrystal form.

1.3.2 Colloidal Synthesis

Colloidal nanocrystals differ from other types of nanocrystals in that their synthesis is highly controllable.[44] Additionally, their binding organic ligands render them dispersible in organic solvent for easy functionalization and film deposition. The controllability afforded by colloidal synthesis stems from the classic materials science concepts of nucleation and growth. Figure 1.5 demonstrates La Mer and Dinegar's model to describe nucleation and growth of sulfur colloids.[45] The model is often used to describe the three stages of a colloidal nanocrystal reaction, which begins with precursor, ligand, solvent, and an optional initiating agent in a flask. As the flask is heated to the desired reaction temperature, the precursor decomposes or reacts with the initiating agent to form monomer, active atomic or molecular units which act as the building blocks of nanocrystals. As monomer concentration increases, it

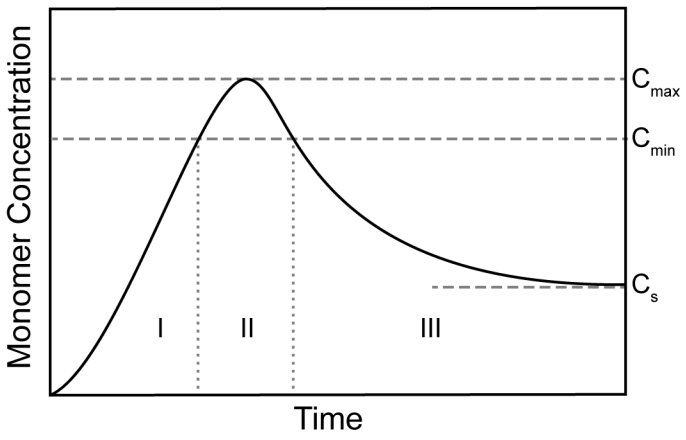

Figure 1.5: La Mer and Dinegar's model applied to nucleation and growth of colloidal nanocrystals. Adapted from La Mer and Dinegar.[45]

eventually becomes favorable for nanocrystal seeds to nucleate. Organic ligands bind to the surface of the newly formed seeds, thus preventing particle aggregation and controlling the addition of monomer to the growing nuclei. As growth continues, monomer concentration eventually becomes saturated, such that the monomer in solution is in equilibrium with the surrounding particles.

As will be seen in Chapter 2 of this dissertation, colloidal synthesis does not always proceed in this simple manner. However, a few guiding principles are evident from the model that aid in synthetic development. In order to achieve a monodisperse product, it is desirable to minimize the time during which nucleation occurs (Part II in Figure 1.5). In a well-controlled reaction, this nucleation will happen as a "burst," usually by injecting precursor or monomeric species into hot solvent, thereby quickly depleting monomer and making further nucleation unfavorable. Remaining monomer in solution contributes instead to the growth of the already formed particles. However, as monomer concentration reaches saturation, a redistribution of particle size, known as Ostwald ripening, can occur. Driven by the energetic advantage of minimizing surface area, smaller particles decrease in size, releasing monomer in solution which then contributes to the growth of larger particles. In this way, particle size becomes polydisperse and therefore, it is desirable to terminate the reaction before this stage is reached.

In order to understand how reaction conditions can influence nanocrystal characteristics like shape and size, one must first understand the driving force for particle nucleation. Nucleation occurs when the energetic advantage of lowering Gibbs free energy (the volumetric term) outweighs the energetic penalty of forming new surfaces (the surface term). Assuming spherical nuclei with radius r, the change in energy upon nucleation is given by:

$$\triangle G(r) = -\frac{4}{3}\pi r^3 \triangle G_{\mathrm{v}} + 4\pi r^2 \gamma \tag{1.9}$$

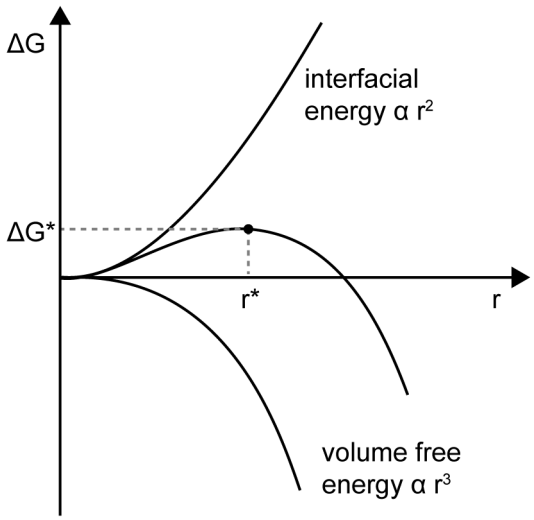

Figure 1.6: Free energy change of nucleation of a spherical particle as a function of radius, including volume and surface contributions. Figure adapted from "Phase Transformations in Metals and Alloys."[46]

Where $\triangle G_{\mathrm{v}}$, the Gibbs free energy difference per unit volume between solid and monomer in solution, is:

$$\triangle G_{\mathrm{v}} = \frac{RT\left(\ln C_{0} - \ln C\right)}{V_{\mathrm{m}}} = -\frac{RT\ln S}{V_{\mathrm{m}}} \tag{1.10}$$

Where V_m is the molar volume of the crystal and S is saturation, the ratio of monomer concentration in solution (C) to equilibrium monomer concentration (C_0).

The r^2 dependence of the surface term, r^3 dependence of the volumetric term, and sum of the two are shown in Figure 1.6. As r increases, the free energy of nucleation initially increases, then decreases. The radius at this transition is the critical radius, r*, which describes the minimum size of a stable nucleus in the system. Hence, a nucleus with radius $r<r^*$ will immediately dissolve back into solution while one with $r>r^*$ will grow. r* can be determined by setting the derivative of the Gibbs free energy of nucleation with respect to r to zero and solving for r, yielding:

$$\frac{dG}{dr} = -4\pi r^2 \triangle G_{\mathrm{v}} + 8\pi r\gamma = 0 \tag{1.11}$$

$$r* = \frac{-2\gamma}{\triangle G_{\mathrm{v}}} = \frac{2\gamma V_{\mathrm{m}}}{RT\ln S} \tag{1.12}$$

The critical nucleus size can thus be controlled by altering temperature and monomer concentration, with higher temperatures and higher concentrations favoring smaller nuclei.

Temperature and monomer concentration also influence particle growth, as they determine whether thermodynamics or kinetics are favored.[44] During thermodynamic growth, particle shape is that which minimizes Gibbs free energy, and thus, G_{surf}. When surface energy is isotropic, only surface area must be minimized leading to the formation of spherical

particles. However, when crystal planes have differing surface energies, the equilibrium shape will be one in which the product of surface energy and surface area is minimzed. This equilibrium shape is often demonstrated by means of a Wulff construction. On the other hand, in the kinetic regime, growth preferentially occurs at high energy facets, yielding metastable, anisotropic shapes like nanorods. These two regimes can be accessed via control of temperature and monomer concentration, with high temperature and low monomer concentration favoring thermodynamic growth and low temperature and high monomer concentration favoring kinetic growth.

1.4.1 Thermodynamics of Oxidation

Because of the many oxidation states that exist and the ease by which oxidation state can change, vanadium oxides are very sensitive to oxygen, readily transforming to a more or less oxidized phase as oxygen partial pressure and temperature are varied. Ellingham diagrams are a useful construct for gauging the stability of a material against oxidation, in which the free energy change of an oxidation reaction, for example $M + O_2 = MO_2$, is plotted as a function of temperature. From equation 1.1, it is clear that the slope of such a plot is equal to $-\Delta S$ of the reaction and the intercept at $T=0$ is ΔH. As high entropy oxygen gas is consumed in the reaction, the overall entropy change is negative, and thus the slope is positive. In other words, oxides become less stable compared to their corresponding metals or oxides with lower oxidation state as temperature increases. As entropy is only weakly dependent on temperature, the slope is a constant straight line as long as the material phase is kept constant (*i.e.*, it doesn't melt or boil). Ellingham diagrams can be used to determine the stable oxide at a given temperature and oxygen partial pressure. This is achieved by drawing a straight line between the desired value of pO_2 on the right axis of the graph and the point labeled 'O' left of the graph. The region through which the line passes at the desired temperature is thus the stable phase under those particular conditions.

Figure 1.7 shows the Ellingham diagram for vanadium oxide. As this Ellingham diagram is constructed with thermodynamic data for select bulk, stable oxides, it is not very useful in for determining stability in metastable nanocrystals. However, a few helpful observations can be made. At the oxygen partial pressure corresponding to air, V_2O_5 is stable through the entire range of temperatures plotted. Therefore, it is the tendency of vanadium metal and oxides of lower oxidation state to oxidize to V_2O_5 when stored in air, although the kinetics of this process may be slow. Furthermore, oxides with lower oxidation state become stable as oxygen partial pressure decreases and as temperature increases. These ideas will become important in this dissertation as bixbyite nanocrystals are shown to oxidize readily in air. In Chapter 3, oxidation and oxidation reversal will be demonstrated by control of oxygen partial pressure and temperature, while in Chapter 4, the controlled oxidation of bixbyite V_2O_3 at low oxygen partial pressures leads to the formation of nanocrystalline VO_2, which is then utilized for smart window applications.

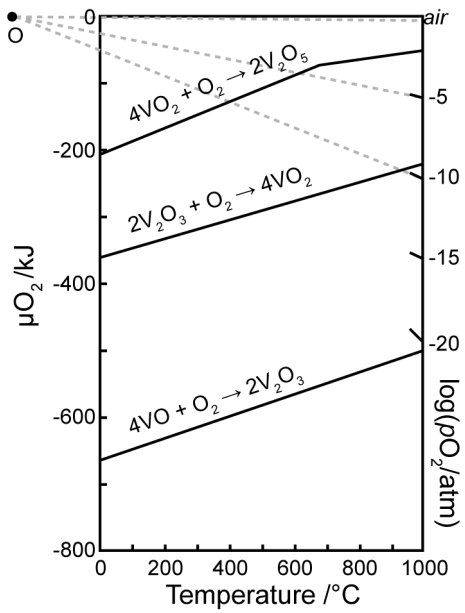

Figure 1.7: Ellingham diagram of the V-O system with dashed lines included for determination of oxide stability at $pO_2 = 0.21$ (air), 10^{-5}, and 10^{-10} atm. Adapted from Yamaguchi *et al.*[47]

1.4.2 Oxygen Defects

When a point defect, such as a vacancy, forms in a material, both internal energy (enthalpy) and entropy increase. The former is associated with changes in bonding while the latter is due to an increase in number of possible atomic configurations in the crystal. The contribution of configurational entropy dominates at low defect concentration, resulting in an initial decrease then increase in Gibbs free energy with vacancy concentration. Therefore, defects are present in all materials at some equilibrium concentration which depends on changes in enthalpy and entropy associated with their formation.

Defects can be divided into two types- intrinsic or extrinsic. Intrinsic defects involve the addition, loss, or misplacement of a constituent atoms of the crystal, while an extrinsic defect forms as a result the addition of an impurity atom in the host crystal. Intrinsic defects can be further characterized as either being stoichiometric, where the ratio of the constituent atoms does not change, or nonstoichiometric, where it does. In all cases, both mass and charge must be preserved as neither can be created or destroyed. Defect reactions are often described using Kroger-Vink notation, where a defect is expressed with a main symbol, denoting the defective element, a subscript, denoting the defect site, and a superscript, denoting the effective defect charge. The following defect reaction describes the formation of an oxygen vacancy:

$$O_O^x \rightarrow \frac{1}{2}O_2(g) + V_O^{\bullet\bullet} + 2e^{'} \tag{1.13}$$

In the case where the host crystal contains cations with more than one stable oxidation state, the following may occur instead:

$$O_{\mathsf{O}}^{\mathsf{x}} + M_{\mathsf{M}}^{\mathsf{x}} \rightarrow \frac{1}{2}O_2(g) + V_{\mathsf{O}}^{\bullet\bullet} + 2M_{\mathsf{M}}^{'} \tag{1.14}$$

This demonstrates that the formation of an oxygen vacancy can either donate electrons to the conduction band of the material, known as delocalized compensation, or reduce cations in the host material, known as localized compensation, in order to maintain charge neutrality. For the formation of oxygen interstitials, these two compensation mechanisms are demonstrated as follows:

$$\frac{1}{2}O_2(g) \rightarrow O_{\mathsf{i}}^{''} + 2h^{\bullet} \tag{1.15}$$

$$\frac{1}{2}O_2(g) + 2M_{\mathsf{M}}^{\mathsf{x}} \rightarrow O_{\mathsf{i}}^{''} + 2M_{\mathsf{M}}^{\bullet} \tag{1.16}$$

Where holes are donated to the valence band or vanadium atoms are oxidized. In the case of vanadium oxides, the small energies associated with changes in oxidation state means that localized compensation of oxygen defects is expected. Both oxygen vacancies and interstitials will be discussed in this dissertation. In Chapter 3, the formation of oxygen interstitials in bixbyite V_2O_3 upon air exposure will be discussed, while in Chapter 4, the formation of oxygen vacancies in VO_2 upon the application of a reducing electrochemical potential will be discussed.

This work focuses on two oxides of vanadium and their phase transformations. The first is the metastable bixbyite phase of V_2O_3 synthesized in colloidal nanocrystal form and the second is nanocrystalline VO_2 in the monoclinic phase, prepared by the controlled oxidation of bixbyite V_2O_3. In Chapter 2, a colloidal route to bixbyite V_2O_3 is presented. Synthetic parameters such as reaction temperature and time are tuned to control shape and size, respectively, while an aminolysis reaction mechanism is elucidated from Fourier transform infrared spectroscopy data. The stability of the resulting phase is examined in both air and an inert environment. Structural changes and weight gain upon air exposure suggest oxidation readily occurs. When heated in inert gas, the bixbyite phase slowly transforms to corundum, the bulk stable phase of V_2O_3, accompanied by particle coarsening. This coarsening and the fact that higher temperatures are required to induce a phase transformation in nanoscale bixbyite than in the bulk suggest that this is an instance in which stability is enhanced due to surface energy effects.

In Chapter 3, the oxidation of bixbyite V_2O_3 nanocrystals is examined in more detail. Rietveld refinement of X-ray diffraction (XRD) data suggests that oxygen interstitials fill the inherently vacant 16c positions in the bixbyite lattice, which is also supported by static energy mapping by density functional theory (DFT). The kinetics of the oxidation process and resulting phase transformation are observed by *in situ* XRD. The resulting transformation rates are fit to an Arrhenius relation, yielding an activation energy of about 1 eV for the

oxidation process. It is reasoned, and supported again by DFT, that the rate limiting step of the process is oxygen diffusion. Surprisingly, the oxidation and phase transformation of bixbyite is found to be reversible by annealing in inert gas at elevated temperature. The low temperature and reversibility of oxidation suggest that bixbyite V_2O_3 could be useful for oxygen storage applications.

In Chapter 4, V_2O_3 is oxidized at low oxygen partial pressures to yield VO_2, which demonstrates the characteristic MIT when heated and cooled. When electrochemically reduced, the nanocrystalline film demonstrates a transition from IR transparent to IR blocking behavior, as previously observed in ionic liquid gated thin films, followed by a unexpected transition back to IR transparency as reduction continues. These optical changes are tracked *in situ* via variable temperature spectroelectrochemistry and the differing optical states are characterized by X-ray absorption and Raman spectroscopies. A shift in vanadium absorption edge is observed, suggesting oxygen vacancy formation accompanies reduction. Extended X-ray absorption fine structure data suggests that the IR blocking state is structurally similar to the monoclinic phase while the subsequent IR transparent phase is likely an entirely new phase.

Finally, in Chapter 5, future work is suggested, including strategies to improve bixbyite phase stability and to improve the performance of thermochromic smart windows made from nanocrystalline VO_2.

2 3

The formation of metastable phases in metal oxide nanomaterials is a well documented phenomenon, examples of which include the stabilization of gamma Al_2O_3, anatase TiO_2, and rhombohedral In_2O_3 below some critical size.[31,36,33] This reversal in stability is thought to be due to the increased influence of surface energy and surface stress at reduced dimensions, which can overcome differences in the bulk Gibbs free energy. Reduction of size not only allows for the tuning of structural and electronic properties of known materials, it can lead to the discovery of entirely new structures that are thermodynamically unfavorable in the bulk.[31,49,34,50,51]

Vanadium oxides are particularly intriguing when contemplating the stabilization of new compounds and phases at the nanoscale. These technologically important materials are studied for their unique optoelectronic, electrochemical, catalytic, and structural properties and well as the property-altering phase transformations that can be thermally initiated in several of the oxides.[52–55] The high surface-to-volume ratio which alters the thermodynamics of nanostructured vanadium oxides is also desirable in batteries and electrochromic devices, where the intercalation of lithium ions is enhanced by increased surface area, and catalysts, where an increase in active sites leads to improved catalytic activity.[56–60] However, the study of these transition metal oxides at the nanoscale is often complicated by the challenges associated with their synthesis. The variety of oxidation states and coordination environments possible in binary vanadium oxide leads to a highly complex phase diagram and many metastable phases, making it difficult to obtain a desired phase.[1] Several metastable phases

have previously been reported in nanoscale vanadium dioxide, such as the structures known as M2, A, and B, which also undergo phase transitions upon heating.[61–63] The study of phase stability in vanadium oxide is therefore a significant, yet challenging problem, particularly in nanostructures where size is expected to alter the thermodynamics of the system.

In comparison to the bulk, phase transformation temperature and kinetics are altered in nanostructured vanadium oxides, as measured by structural, optical, magnetic, and electrical means. Because of its unique properties and phase transformation near room temperature, vanadium dioxide is the most widely studied of the vanadium oxides in terms of phase stability. As size is decreased, the number of structural defects, which serve as heterogeneous nucleation sites for transformation, are invariably reduced. Indeed, the phase transformation of vanadium dioxide, which occurs at 68°C in the bulk, exhibits reduced transformation temperatures and increased hysteresis width as size is reduced, a result which is ascribed to a reduction in structural defects, although interfacial contributions likely affect the transition as well.[2,41,64,65] The stabilization of the metastable M2 phase has been demonstrated in strained VO_2 microbeams as well as in VO_2 nanobeams grown in oxygen-rich conditions, while M2 nanoparticles can be stabilized by their deposition on certain substrates, demonstrating the importance of strain and composition on phase stability.[63,13,66] Magnetic characterization of corundum V_2O_3, another vanadium oxide which experiences a phase transformation, shows a gradual onset of antiferromagnetic ordering in nanocrystals, as compared to the sharp transition observed in the bulk.[67] The gradual nature is thought to be due to the large particle size distribution, rendering it impossible to determine the size-dependence of transition temperature. Clearly, improved synthetic methods for vanadium oxide nanocrystals are necessary in order to control factors such as strain, composition, and monodispersity, while eliminating the influence of interfacial effects present in lithographic approaches.

Several approaches to producing nanostructured vanadium oxide have been reported in the last decade, the majority of which yield anisotropic morphologies, namely nanorods, nanowires, and nanoribbons. Isotropic nanostructures are reduced in an additional dimension as compared to 1D nanomaterials and therefore are more likely to exhibit phases unstable in the bulk. Unfortunately, synthetic routes to isotropic vanadium oxide nanostructures are scarce and those that have been reported suffer from limited size control and particle dispersibility, factors which have hindered in depth study of size-dependent phase stability.[59,41,67,68,43] A colloidal route to vanadium oxide nanocrystals is desirable due to the high degree of size control that is possible with a well designed synthesis and the presence of a ligand shell, which allows for dispersion in various solvents. Additionally, colloidal chemistry allows for the tuning of chemical potential as an additional parameter in the controlling phase stability.[69] However, the published colloidal syntheses of vanadium oxides are limited to amorphous nanoparticles, which crystallize to monoclinic VO_2 only after a post-synthetic annealing treatment, rendering them non-dispersible, and one example of V_2O_3 nanocrystals, which occur in the corundum phase.[70,71] A well controlled colloidal synthesis is therefore necessary to begin to systematically understand influence of size on the stability of vanadium oxides at the nanoscale.

Here we report a colloidal route to V_2O_3 nanocrystals with a cubic bixbyite structure, a common phase for some main group metal oxides including In_2O_3 and Y_2O_3 as well as mixed metal vanadates such as $InVO_3$, but only recently observed in V_2O_3 as a metastable phase.[29,72] The synthetic conditions are varied to tune morphology from porous nanoflowers

to dense pseudospherical nanocrystals and the reaction and formation mechanism are explored. Over the course of several days and weeks, the nanocrystals oxidize slightly under ambient conditions while retaining their bixbyite structure, only transforming to V_3O_7 at 250°C and to V_2O_5 at 400°C when annealed in air. When annealed in an inert atmosphere, V_2O_3 bixbyite persists as a single phase up to 700°C, after which the structure begins to transform to the corundum phase stable in bulk V_2O_3. This transformation occurs concurrently with slight particle coarsening of the nanocrystals.

2.2.1 Synthetic Methods

In a typical synthesis using standard Schlenk line techniques, a 50 ml three-neck flask containing 0.265 g (1 mmol) vanadyl acetylacetonate (Strem Chemicals, 98%), 1.07 g (4 mmol) oleylamine (Sigma Aldrich, 70%), and 1.13 g (4 mmol) oleic acid (Sigma Aldrich, 98%) in 8 ml squalane (Sigma Aldrich, 99%) was degassed under vacuum at 110°C for 1 hour. The mixture was then heated, under nitrogen flow, to the desired growth temperature (between 310°C and 370°C) and held at this temperature for 1 hour. The nanocrystals were cleaned by repeated flocculation with isopropanol and redispersion in hexanes.

2.2.2 Transmission Electron Microscopy

Transmission electron microscopy (TEM) was used to determine the size and morphology of the nanocrystals. Nanocrystals dispersed in hexane were dropped onto a 400-mesh copper grid covered with an ultrathin carbon film and allowed to dry. Low resolution images were acquired using a JEOL-2100 microscope with a LaB_6 filament operating at 200 kV and equipped with a Gatan digital camera. A JEOL-2100F FETEM microscope operating at 200 kV was used to capture high resolution images and electron diffraction patterns.

2.2.3 X-ray Diffraction

The structure and crystallite size were determined by X-ray diffraction (XRD). θ-2θ scans were collected at room temperature using a Bruker D8-Advance x-ray diffractometer equipped with a GADDS area detector operating at the Cu Kα wavelength, 1.54 Å. Rietveld refinement was completed using the GSAS-EXPGUI package, using data collected on a Bruker D8-Advance X-ray diffractometer in Bragg-Brentano geometry equipped with an air free sample holder and point detector and also operating at the Cu Kα wavelength, 1.54 Å.[73,74] Data for the refinement was collected at room temperature with a step size of 0.01°. Peak profiles were fitted with a Pseudo-Voigt function and the background was fitted with a 24-term shifted Chebyschev polynomial. Instrumental profile terms were determined by the refinement of a lanthanum hexaboride standard. In situ XRD patterns were collected while annealing in a helium atmosphere at the National Synchrotron Light Source at Brookhaven National Laboratory, beamline X20C. The nanocrystals were heated at a rate of 5°C/sec up to the desired temperature then held for 20 minutes with simultaneous XRD data collection by a linear diode array detector using a photon energy of 6.9 keV (λ = 1.797 Å).

2.2.4 Additional Techniques

Fourier transform infrared spectroscopy (FTIR) measurements were done on a Perkin Elmer Spectrum One FTIR Spectrometer equipped with a 45° ZnSe attenuated total reflection (ATR) crystal. The optical properties of the nanocrystals dispersed in tetrachloroethylene (>99%, Aldrich) were analyzed with UV-Vis spectroscopy, using a Shimadzu UV-3600 dual beam spectrophotometer. Thermogravimetric analysis (TGA) was performed using a Q5000IR thermogravimetric analyzer from TA Instruments.

2.3.1 The Influence of Growth Temperature on Nanocrystal Morphology

Low and high resolution TEM images of nanocrystals synthesized for 1 hour at different temperatures are shown in Figure 2.1, along with the corresponding electron diffraction patterns which can all be indexed to the bixbyite phase. When synthesized at 310°C, the resulting structure was that of a nanoflower with distinct "petals" and a porous internal structure. In addition to nanoflowers, small nanoparticles, 4 to 15 nm in size, were also produced, which could be separated from the nanoflowers by size-selective precipitation (Figure A.1). At higher reaction temperatures, the particles were denser and by 370°C, the nanocrystals lost all flower-like qualities and appeared spherical. Highly faceted nanocrystals with truncated octahedron morphology were apparent as a minority product in the yield obtained at the highest reaction temperatures (Figure A.2). These, like the nanoflowers, appear to also possess the bixbyite phase based on lattice spacing measured by high-resolution TEM. The high temperatures necessary to form these faceted structures suggest that kinetic factors favoring the nanoflower morphology must first be overcome before the nanocrystal can achieve this presumably lower energy shape.

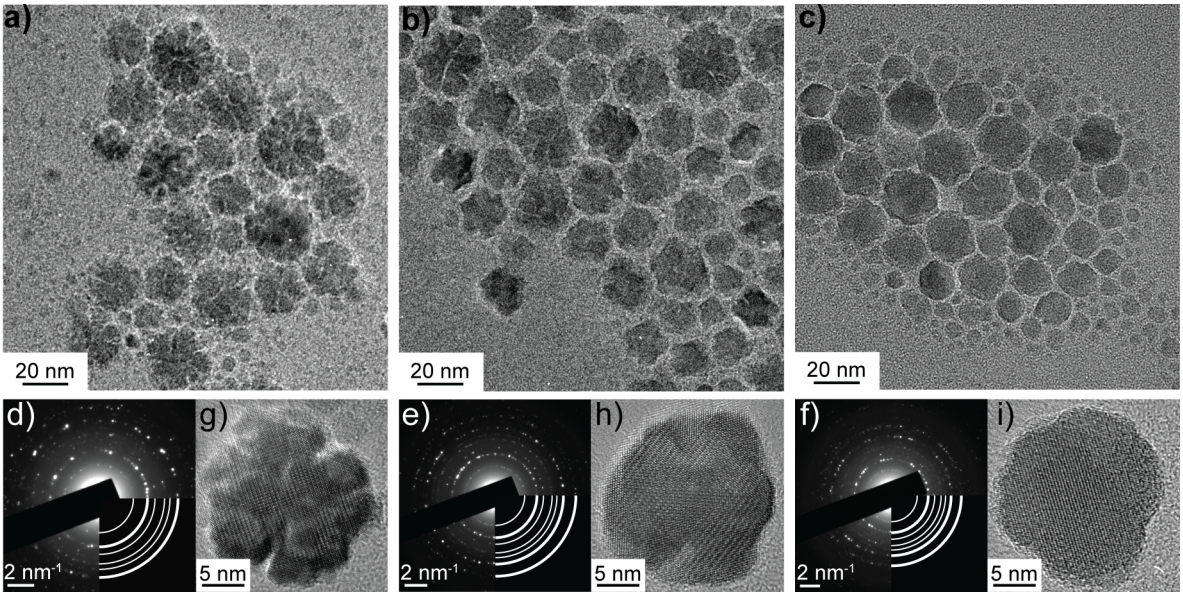

Figure 2.1: Low (a, b, c) and high (g, h, i) resolution TEM images and electron diffraction patterns (d, e, f) of nanocrystals synthesized at 310°C (a, d, g), 340°C (b, e, h), and 370°C (c, f, i)

2.3.2 Determination of Nanoflower Growth Mechanism

To elucidate the nanoflower formation mechanism, reaction time was varied and the resulting product was characterized by TEM. Figure 2.2 shows TEM images of nanocrystals synthesized by holding the reaction temperature at 340°C for 0 minutes, 4 hours, and 24 hours. Spherical particles, with an average diameter of 8.0 ± 1.9 nm, were obtained when a small aliquot of reaction solution was rapidly quenched immediately after reaching 340°C (Figure 2.2a). The nanoflower morphology emerged with any amount of extended heating so that it was not possible to quench the full reaction volume without flowers forming. Nanoflower diameter was found to increase with heating time, with an average diameter of 18.5 nm ± 4.3 after 0 minutes at 340°C (Figure 2.2b), 19.4 nm ± 4.6 after 1 hour of heating (Figure 2.1b), 22.9 nm ± 6.8 after 4 hours (Figure 2.2d), and 32.4 nm ± 7.5 after 24 hours (Figure 2.2e)(Figure A.3). The number of small particles in the product also appeared to decrease with heating time, suggesting that the growth of the flowers progressed by the attachment of smaller particles and flowers.

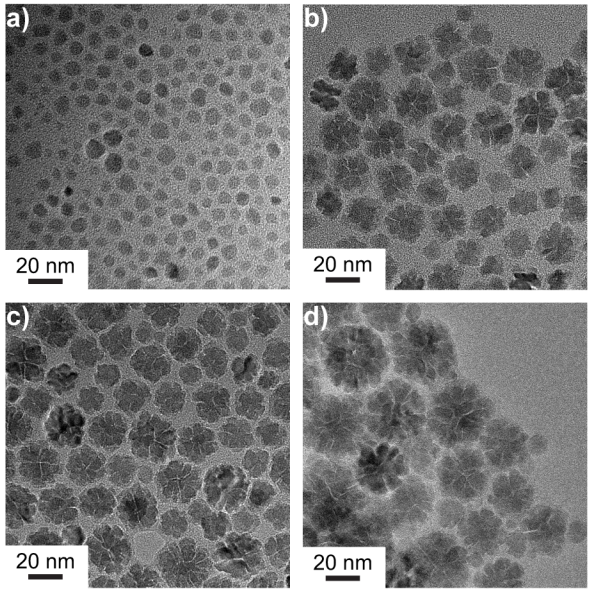

Figure 2.2: TEM images of nanocrystals heated at 340°C for a) 0 minutes followed by rapid quench, b) 0 minutes followed by slow cooling, c) 4 hours, and d) 24 hours

The observation of smaller, more regular particles early in the reaction suggests that the formation of nanoflowers occurs by the nucleation and growth of primary nanocrystals in the early stages of heating, followed by the aggregation of several primary crystals to form flowers. This cluster-mediated growth mechanism has previously been postulated to explain the formation of Au-Pd nanoflowers.[75] Under the given reaction conditions, the aggregation was limited so that the maximum V_2O_3 bixbyite flower size of around 30 nm in diameter was rarely exceeded. Similar behavior has previously been observed in the formation of In_2O_3 nanoflowers, also in the bixbyite phase. In that case, the aggregation process was thought to result from insufficient ligand coverage, so that the progression of growth stopped once the ligands fully passivated the nanoflower surface.[76] Indeed, we found that the addition of excess oleic acid and oleylamine circumvented flower formation; however the resulting vanadium oxide nanoparticles were amorphous by XRD (Figure A.4).

2.3.3 Determination of Chemical Reaction Mechanism

The FTIR spectra of pure oleic acid and the nanocrystals isolated from the crude reaction mixture are shown in Figure 2.3a and b, respectively. The peaks at 1550 cm^{-1} and 1450 cm^{-1} in Figure 2.3b can be assigned to the COO- symmetric and asymmetric stretching bands, respectively, suggesting that oleate ligands are bound to the nanocrystal surface.[77] The stretching band separation of 100 cm^{-1} is indicative of a chelating bidentate coordination mode.[78] The C=O stretch peak at 1700 cm^{-1}, characteristic of protonated carboxylic acid, in Figure 2.3a is not present in the nanocrystal spectrum, indicating that no free oleic acid remains after purification. The peaks at 2850 cm^{-1} and 2800 cm^{-1} in Figure 2.3b therefore correspond to the methylene C-H symmetric and asymmetric stretch from the ligands rather than free oleic acid. The peaks at 1000 cm^{-1}, 850 cm^{-1}, and at the edge of the scanning

range (around 600 cm^{-1}) of Figure 2.3b can be assigned to the V=O stretch of the terminal bonds at the nanocrystal surface, V-O-V bridging stretch, and V-O stretch of the inorganic core, respectively.[79] In order to further analyze the reaction pathway, small aliquots were collected at various stages during the heating and analyzed using FTIR. As shown in Figure 2.3e, absorbing peaks at 1616 cm^{-1} and 1586 cm^{-1} form after degassing for an hour at 110°C. These peaks also appear when oleic acid is not present (Figure A.5) suggesting that a complex forms between the oleylamine and vanadyl acetylacetonate during the degassing step. This is also supported by a shift in the vanadyl acetylacetonate V=O stretch peak upon mixing with oleylamine (Figure A.6), indicating a change in coordination environment.[80] As the mixture of reactants is heated further, the peaks at 1616 cm^{-1} and 1586 cm^{-1} decrease in intensity and peaks located at 1644 cm^{-1} and 1557 cm^{-1} become apparent. These can respectively be assigned to the C=O stretch and N-H bend of an amide, the byproduct of an aminolysis reaction.[77] These peaks are also present in the FTIR spectrum taken of the supernatant after the first centrifugation in the cleaning process, shown in Figure 2.3d along with the spectra for pure squalane for reference in Figure 2.3c. The case for an aminolysis reaction is further supported by the fact that no product could be recovered when oleylamine was not present in the reaction. The oleylamine is likely responsible for the reduction in vanadium oxidation state from 4+ in the precursor salt to the final 3+ state in the sesquioxide. Supporting this hypothesis, reducing the amount of oleylamine from 4 mmol to 2 mmol resulted in mixed phase nanoflowers with both bixbyite V_2O_3 and VO_2(A) phases present (Figure A.7), indicating an incomplete reduction of vanadium. When the reaction was performed without oleic acid, the resulting nanocrystals, with an average diameter of 5 nm, exhibited broad diffraction peaks which could not be indexed to any known vanadium oxide phase (Figure A.8). Specific amounts of both oleic acid, which acts as the primary surface-capping agent, and oleylamine, the reducing and initiating agent, are therefore required in order to produce the bixbyite phase. The following structural studies were therefore performed on nanocrystals synthesized using 4 mmol oleic acid and 4 mmol oleylamine, a reaction temperature of 370°C, and a reaction time of 1 hour.

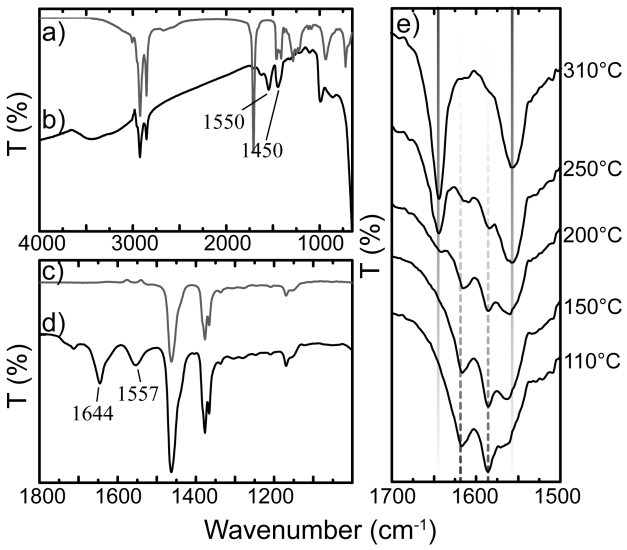

Figure 2.3: FTIR spectra of a) pure oleic acid, b) clean V_2O_3 nanocrystals, c) pure squalane, d) the supernatant collected during the first cleaning step, and e) the reaction mixture collected at various temperatures during heating, with oleylamine-precursor complex peaks marked with dotted line and amide byproduct peaks marked with solid line

2.3.4 Rietveld Refinement of Bixbyite Structure

The XRD patterns of the as-synthesized nanocrystals could all be assigned to the bixbyite phase of V_2O_3, regardless of reaction time and temperature. In addition to the new bixbyite phase, V_2O_3 is known to exist in two other phases: The corundum phase, which is metallic, paramagnetic, and stable under normal conditions, and an insulating, antiferromagnetic, monoclinic phase, which is stable below 170 K.[2,81,22,23] The bixbyite structure is closely related to the fluorite structure, consisting of 8 fluorite unit cells with a quarter of the oxygen anions removed in an ordered manner. The presence of structural oxygen vacancies result in a slight shift in cation and anion position compared to fluorite. Cations in the bixbyite structure occupy two different octahedral lattice sites, the 8d and 24d Wyckoff positions, which differ in terms of the position and symmetry of the surrounding structural vacancies.[82] The bixbyite and corundum structures of V_2O_3 are shown in Figure 2.4a and b. Weber *et al.* was this first to report the crystallization of bulk V_2O_3 in the bixbyite structure by reacting vanadium trifluoride with forming gas at elevated temperatures.[29] However, their bixbyite could not be isolated as a pure phase and reverted to VO_2 within 3 weeks of exposure to air. The synthesis of porous V_2O_3 urchin-like micronanostructures with a bixbyite crystal structure was also recently reported by Xu *et al.*[72] In both cases, the structures were found to rapidly transform to corundum phase upon heating in an inert atmosphere at around 550°C and 540°C, respectively. A Rietveld refinement was performed in order to confirm the bixbyite structure and compare the structural parameters with previous reports. The results of the refinement are shown in Figure 2.4c and Table A.1 in Appendix A. The bixbyite-type structure was found to exist as a pure phase, with space group Ia-3 and a lattice parameter of 9.363 Å. The quality of the refinement was evaluated by the weighted residual error (R_{wp}

= 2.31%) and goodness of fit indicator (χ^2 = 2.339). The calculated lattice parameter is smaller than the value of 9.395 Å previously reported by Weber *et al.* Lattice contraction in nanocrystal oxides is unusual, with most exhibiting an increase in lattice parameters ascribed to enhanced bond ionicity at the nanoscale.[83–85] This can be also understood in the context of the competing influences of Madelung energy, resulting in lattice expansion in finite sized ionic materials, and surface stress, causing lattice contraction in materials with covalent bonding. The degree of bond ionicity (or covalency) therefore governs the change that is observed in lattice parameter as size is reduced. Lattice contraction was previously observed in anatase TiO_2 nanocrystals, which the authors attributed to positive surface pressure due to surface hydration.[86] In the present case of bixbyite V_2O_3, it is difficult to provide a definitive explanation considering that the structural parameters of the bulk are still not well established.

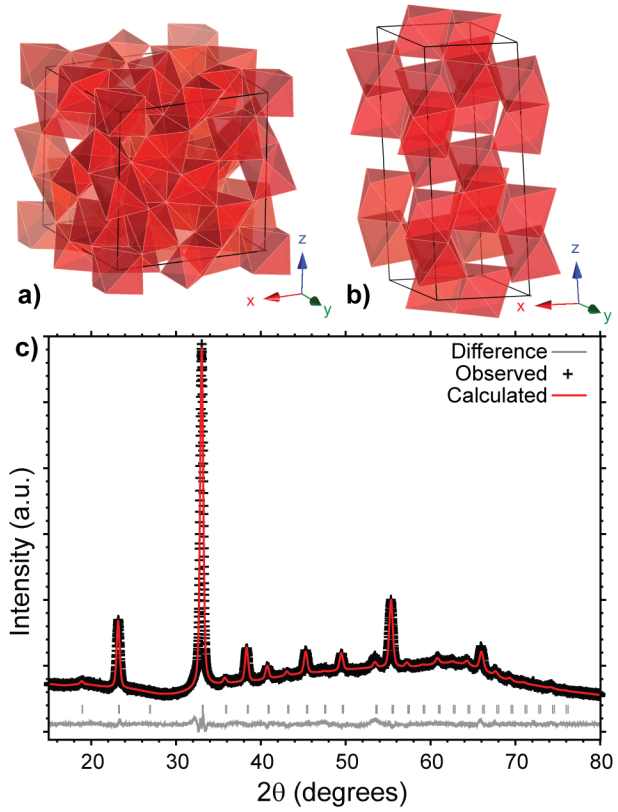

Figure 2.4: a) V_2O_3 bixbyite and b) corundum crystal structures. c) XRD pattern of V_2O_3 bixbyite nanocrystals with results of Rietveld refinement. Raw data is marked with black crosses, the fit after refinement is marked by the red line, and the gray line shows the difference between the two. Calculated peak locations are indicated by the gray marks.

2.3.5 Determination of Optical Band Gap

Very recently, a theoretical direct band gap of 0.75 eV for bixbyite V_2O_3 was reported.[87] We used UV-Vis spectroscopy to determine absorbance as a function of wavelength for particles suspended in tetrachloroethylene. Using this data, a Tauc plot was computed. Briefly, $(\alpha h\nu)^2$

was plotted as a function of energy and the linear region was extrapolated to the x-axis in order to determine the band gap of the bixbyite nanocrystals (Figure A.9). Based on this analysis, a direct band gap of 1.29 eV was derived. The large blue shift in band gap as compared to the theoretical value may be due to quantum confinement effects. The average petal diameter approaches the exciton Bohr radius of bixbyite In_2O_3, estimated to be between 2.6 and 5 nm.[88] Another factor that could contribute to the strongly blue shifted band gap would be a substitutional charge carrier concentration, which could arise, for example, from an abundance of oxygen vacancies. These preliminary observations suggest that the details of the V_2O_3 bixbyite nanocrystal electronic structure deserve more investigation.

2.3.6 Phase Stability in Air

Recalling that bulk V_2O_3 in the bixbyite phase readily oxidizes to VO_2 at room temperature, XRD patterns were taken at various times after synthesis and film deposition to assess the phase stability of our V_2O_3 nanocrystals in air.[29] The inset in Figure 2.5a shows the position of the (222) reflection of the bixbyite phase as a function of exposure time in air at room temperature. A slight shift in peak position to lower 2θ values is apparent over time, shifting by approximately 0.2° after 3 months of air exposure. Analysis of the full XRD scan, shown in Figure 2.5a, shows that this shift occurs for all peaks, indicating a uniform expansion in lattice. A decrease in intensity of many of the bixbyite peaks is also apparent after several months, while the peaks corresponding to the fluorite (111), (200), (220), and (311) planes are largely unchanged. This suggests that the lattice becomes less distorted with time, with the vanadium atoms shifting to lattice positions closer to that of the fluorite structure, as shown in Figure 2.5c. We believe this could be caused by the filling of structural oxygen vacancies in the bixbyite lattice, a behavior that has also been observed in isostructural indium and scandium orthovanadates under oxidizing conditions.[89,90] For example, *in situ* XRD observation of air oxidation in bixbyite $InVO_3$ displayed a peak shift to lower 2θ starting at 150°C, indicating the onset of oxygen uptake, and then a large shift at 225°C, indicating the formation of a new metastable defective fluorite phase with the formula $InVO_{3.5+x}$.[89] At 400°C the structure transformed to the $InVO_4$ zircon structure. Similar structural changes were observed during the oxidation of $ScVO_3$.[90] The oxidation of the bixbyite phase is also observed in the cerium oxide system with bixbyite Ce_2O_3 readily transforming to fluorite CeO_2 under oxidizing conditions, made possible by the facile conversion between cerium oxidation states.[91] It has been suggested that this oxidation, which occurs quickly in bulk material, may be slowed or completely prevented in Ce_2O_3 nanoparticles due to enhanced stability of the trivalent oxide at reduced sizes.[92] In contrast to the observed behavior of vanadium oxide, the cerium oxide lattice contracts upon oxidation, due to an increased ionic attraction between the 4+ cation and oxygen anion, as compared to the 3+ ion.[93,94] In the case of vanadium oxide, the bonding is approximately 34% ionic, as calculated from Pauling's empirical relationship relating electronegative values to degree of ionic character. The bond ionicity of vanadium oxide may therefore have less of an effect on the equilibrium lattice constant than in the case of ceria which was calculated to be 44% ionic. Any attractive force between ions in the lattice is likely overcome by the influence of lattice strain caused by the addition of oxygen, resulting in the expansion of the lattice and slight rearrangement of atoms in the unit cell.

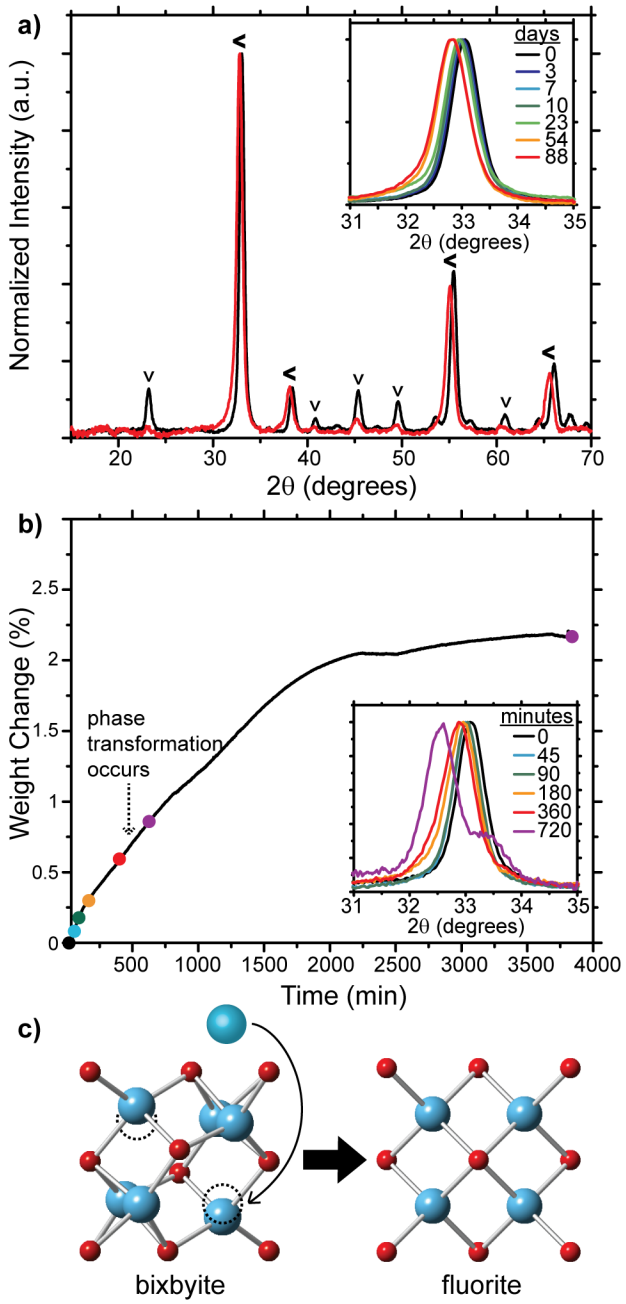

Figure 2.5: XRD pattern of as synthesized bixbyite nanocrystals (black) and nanocrystals stored in air for 88 days (red), inset: XRD pattern centered at bixbyite (222) peak as a function of storage time in air. b) TGA scan of bixbyite nanocrystals heated in air at 100°C for 64 hr, inset: XRD pattern centered at bixbyite (222) peak as a function of annealing time in air at 100°C. c) Bixbyite and fluorite crystal structures viewed from the [100] direction, demonstrating transformation from more to less distorted structure as oxygen vacancies (marked by dotted lines) become filled. Only one eighth of the bixbyite lattice is shown for clarity.

To further elucidate the behavior of our V_2O_3 bixbyite nanocrystals under oxidizing conditions, their mass was monitored while annealing at 100°C under air flow. Figure 2.5b shows an increase in weight of approximately 0.5% after 6 hours of heating, corresponding to the filling of about 1 of the 16 structural vacancies in each bixbyite unit cell. Upon further annealing at 100°C the weight continued to increase, eventually leveling off to a constant value after about 48 hours. The inset in Figure 2.5b shows the position of the (222) bixbyite peak as a function of annealing time in air at 100°C, exhibiting a similar shift in the first 6 hours of annealing as seen in the samples stored under ambient conditions for several months. However, XRD of the nanocrystals annealed for 12 or more hours indicates a transformation to an unidentified structure, exhibiting splitting of the former (222) bixbyite peak and the formation of several new peaks at higher 2θ. This transformation did not reverse upon annealing in forming gas at 100°C. Annealing in air at higher temperature resulted in additional oxidative transformation. At 250°C, the nanocrystal film oxidized to V_3O_7, and at 400°C, the material fully oxidized to V_2O_5. The resulting V_2O_5 materials did not retain the nanoflower morphology, and instead sintered into micron-sized particles. This phase and morphology change was followed by XRD and TEM as shown in Figure A.10. Overall, the V_2O_3 bixbyite phase of our nanocrystals was far more stable against oxidation than the previously reported bulk material, requiring significant heating in air to induce progressive oxidative phase transformations.

2.3.7 Phase Stability in an Inert Atmosphere

For oxide nanocrystals, there often exists a critical size below which the lower surface energy phase is stable and above which the lower bulk Gibbs free energy phase is stable.[31,36,33] When nanocrystals are heated, particle coarsening can occur, causing a decrease in surface area and triggering a transformation from the metastable phase found in nanocrystals to the bulk stable phase. To assess their phase stability and monitor the onset of any phase transformations, the bixbyite nanocrystals were heated in an inert atmosphere (to avoid oxidation) and characterized by *in situ* x-ray diffraction. Figure 2.6 shows peak intensity in a portion of the 2θ range, containing the (440) bixbyite peak and (116) corundum peak, as a function of time at 800°C (Figure 2.6a), 850°C (Figure 2.6b), and 900°C (Figure 2.6c), after heating from room temperature. While holding at these temperatures, the bixbyite nanocrystals begin to transform to corundum phase, with the onset of the transformation occurring after an incubation period of approximately 10 minutes, 3 minutes, and less than 1 minute of heating, respectively. The transformation is irreversible in that the structure does not revert back the bixbyite phase upon cooling. Rather, the corundum phase persists.

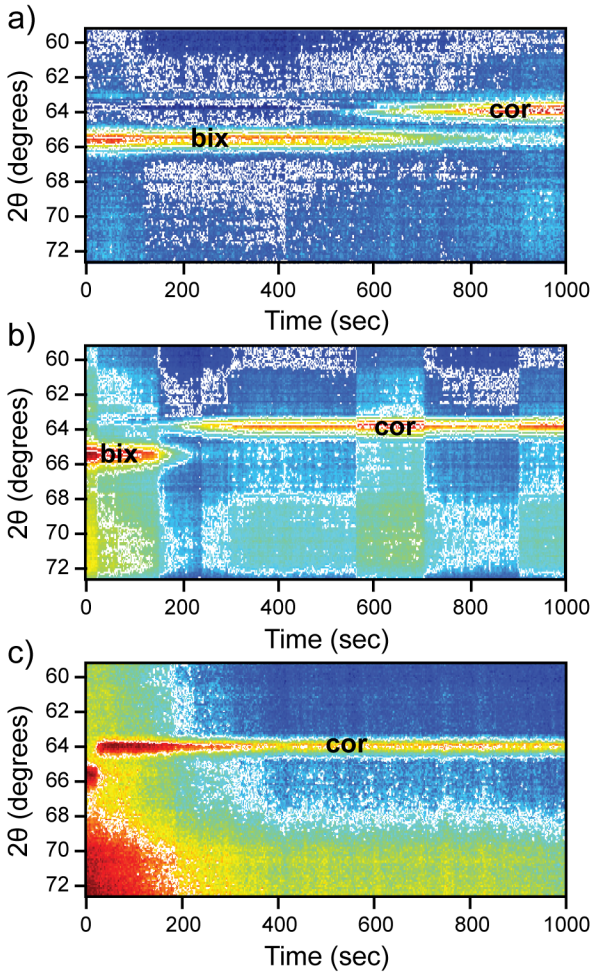

Figure 2.6: *In situ* XRD pattern of V_2O_3 bixbyite nanocrystal film heated to a) 800°C b) 850°C, and c) 900°C. The location of the bixbyite (440) peak is labeled "bix" and the location of the corundum (116) peak is labeled "cor."

The progression from bixbyite to corundum can be further understood by comparing the full θ-2θ scans over the course of the transformation (Figure 2.7). The peak widths of the as-deposited, partially transformed, and fully transformed samples were subjected to a Scherrer analysis to assess the critical size for phase transformation. Due to the similarity in peak positions of the two phases, only 2 regions were analyzed to determine the crystallite size before, during, and after transformation: the (211) bixbyite peak and (012) corundum peak at around 23° and 24°, respectively, and the (116) corundum peak and (440) bixbyite peak at around 53° and 55°, respectively. An average crystallite size of 14.5 nm was determined for the as-deposited bixbyite sample. This size is larger than the primary particles that aggregate and fuse together to make up the dense pseudospherical nanocrystals, but smaller than the nanocrystals themselves, indicating a partial degree of oriented attachment among the flower structures in the initial stages of formation, resulting in polycrystalline nanocrystals upon densification. This is consistent with observations by TEM (Figure 2.1). After heating the sample for 30 minutes at 700°C in argon, both bixbyite and corundum phases are present

in the sample. The bixbyite peak width corresponds to a crystallite size of 16 nm, which is very similar to the size before the onset of transformation. The corundum peak, however, corresponds to a crystallite size of 27 nm, which is within the measured size range of the nanocrystals. Therefore, it can be inferred that the first particles to transform are the larger, fully lattice-oriented nanocrystals. This is likely followed by the transformation of the crystals that have undergone atomic rearrangement along non-oriented grain boundaries to reach the critical size. After 1 hour at 700°C, the bixbyite peak has diminished such that it is still visible yet it is impossible to reliably determine the peak broadening. The corundum peak width for this sample corresponds to a crystallite size of 40 nm, nearly twice the average diameter of the as synthesized bixbyite nanocrystals, indicating that some degree of particle coarsening has occurred during the course of the transformation. After 2 hours at 700°C, the sample is fully transformed to corundum phase, with peak widths corresponding to an average crystallite size of 42.5 nm, signifying that very little additional coarsening occurs between 1 and 2 hours of annealing.

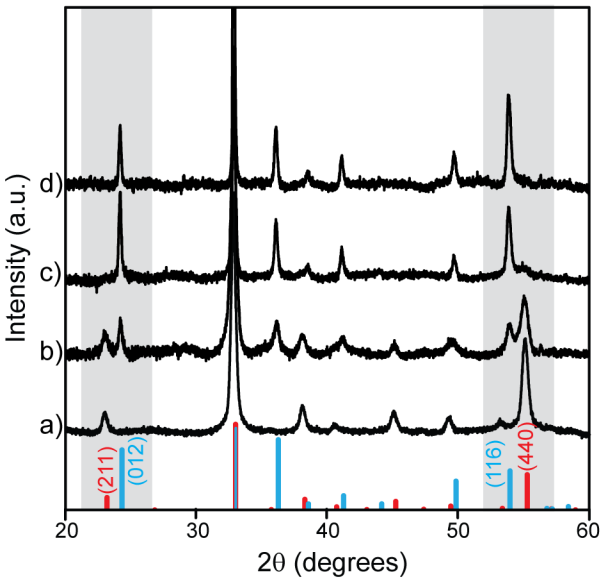

Figure 2.7: XRD pattern of the a) as-deposited bixbyite nanocrystal film, partially transformed samples containing both bixbyite and corundum phases after annealing in argon at 700°C for b) 30 minutes and c) 1 hour, and d) fully transformed corundum phase after 2 hours of annealing in argon at 700°C. The XRD patterns for the bulk bixbyite and corundum phases of V_2O_3 are shown at the bottom of the image in red and blue, respectively. The regions containing the bixbyite (211) and corundum (012) peak, and the region containing the bixbyite (440) and corundum (116) peak are highlighted in gray.

Based on this analysis, the critical size for transformation from bixbyite to corundum V_2O_3 is estimated to be between 27 and 42 nm. This is within the range of previously reported critical sizes for other metastable oxide nanocrystals; however these values are not always well established. For example, while thermodynamic analysis of the stability of TiO_2 predicts a critical size for the anatase to rutile conversion of 14 nm, experimental results

vary from agreement to as high as 45 nm.[36,95–97] Clearly, size is not the only critical factor in determining phase stability. Factors that differ based on preparation method, such as the ligand binding environment and particle morphology, which in turn affect surface stress, are also significant. Nevertheless, the high temperatures necessary to induce transformation as well as the slow kinetics of the transformation suggest that the bixbyite phase of our V_2O_3 nanocrystals has a significantly lower surface energy compared to the corundum phase.

We have synthesized pure phase V_2O_3 bixbyite nanocrystals, a metastable phase of vanadium oxide discovered in 2011. The nanoflower morphology of the particles was shown to be tunable with reaction temperature, densifying to spherical particles when synthesized at 370°C. The growth and reaction mechanisms of the colloidal synthesis were discussed and it was determined that an aminolysis reaction takes place. The phase stability in air at room temperature and elevated temperatures was explored. The particles stored under ambient conditions experienced an expansion in lattice constant, which we attributed to oxygen filling of structural vacancies within the bixbyite lattice. The onset of transformation to the bulk stable corundum phase was shown to occur over the coarse of about an hour at 700°C and over the coarse of about a minute at 900°C, indicating that the transformation kinetics are highly dependent of temperature. A Scherrer analysis of peak widths at different stages of the transformation led us to estimate a critical size for transformation between 27 and 42 nm. Our results motivate further investigation of the electronic properties of bixbyite V_2O_3 and of the interplay of size and structure in vanadium oxides more broadly.

2.4.1 Acknowledgments

The authors acknowledge F. Gandara for assistance with XRD measurements and A. Llordes for helpful discussions. Work at the Molecular Foundry was supported by the Office of Science, Office of Basic Energy Sciences, of the U.S. Department of Energy under Contract No. DE-AC02-05CH11231. Use of the National Synchrotron Light Source, Brookhaven National Laboratory, was supported by the U.S. Department of Energy, Office of Science, Office of Basic Energy Sciences, under Contract No. DE-AC02-98CH10886. Ms. Bergerud was supported by a UC Berkeley Chancellor's Fellowship for Graduate Study and a National Science Foundation Graduate Student Research Fellowship under Grant No. DGE 1106400.

2 3

The oxides of vanadium are known for both their structural complexity and fascinating properties, as manifested in the many stable and metastable phases and phase transitions that exist in these materials. Vanadium sesquioxide (V_2O_3) is one such oxide, transforming from the antiferromagnetic, insulating monoclinic phase to the paramagnetic, metallic corundum phase at 170 K.[2,22,23] This phase transformation is of great fundamental importance due to its model Mott-Hubbard transition behavior.[28] Recently, a metastable phase of V_2O_3 with a cubic, bixbyite structure was discovered.[29] This new polymorph has since been the subject of several studies, both fundamental and applied, including its proposed use as a p-type conductor and battery electrode.[99,72] Synthesizing V_2O_3 nanocrystals stabilizes the metastable phase and allowed us, in 2013, to prepare phase pure bixbyite.[48] Using our colloidal synthetic method, we now demonstrate low temperature, reversible oxidation and reduction of bixbyite V_2O_3 nanocrystals, a phenomenon which could be harnessed for oxygen storage.

The bixbyite structure has a body-centered cubic lattice with space group Ia-3. Often described as anion deficient fluorite, bixbyite is comparable to a 2 x 2 x 2 fluorite supercell with a quarter of the anions removed, as demonstrated in Figure 3.1. These vacated sites are the 16c Wyckoff positions in the Ia-3 space group, which are inherently unfilled in bixbyite.[82] Cations in the bixbyite structure populate two symmetry inequivalent positions- the 8b and 24d Wyckoff positions, otherwise known as b- and d-sites, while anions populate the 48e positions for a total of 80 atoms in the unit cell. Bixbyite is the stable polymorph of several M_2O_3 type oxides, including indium oxide, yttrium oxide, and manganese oxide. As a vanadium oxide, this phase was found to be metastable, transforming to the bulk stable corundum phase of V_2O_3 upon heating in an inert atmosphere. Since the initial discovery of bixbyite V_2O_3, several papers have been published on the subject, but only three synthetic

routes to the bixbyite polymorph have been reported as of yet. Weber *et al.* synthesized a mixture of corundum and bixbyite V_2O_3 from the reduction of vanadium trifluoride at 600°C in water saturated forming gas.[29] This mixture was observed to transform to pure corundum phase upon heating to 550°C in argon. Xu *et al.* formed bixbyite with an urchin-like morphology through the thermal decomposition of vanadyl ethylene glycolate.[72] Transformation to corundum occurred upon heating in argon at 540°C in this instance. Lastly, we previously reported a colloidal route to bixbyite nanocrystals (NCs) with enhanced stability relative to its bulk counterparts.[48] Transformation to corundum proceeded slowly over the course of about 1 hour when held at 700°C, and was accompanied by particle coarsening. This enhanced stability was reasoned to be due to the non-negligible effect of surface energy on Gibbs free energy at the nanoscale, a well-known phenomenon in nanocrystals.[31,36,32] The suspected lower surface energy of bixbyite is thought to alter the relative energetics of the two phases, potentially favoring bixbyite over corundum below some critical size.

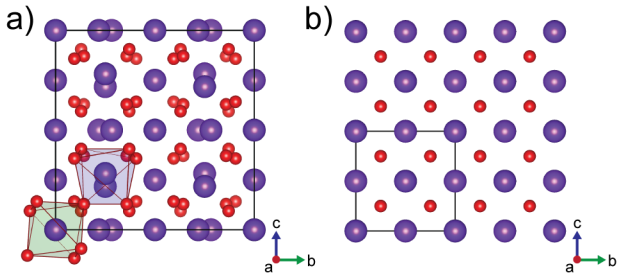

Figure 3.1: Bixbyite unit cell with b- and d- sites marked with green and blue polyhedra, respectively. b) The undistorted fluorite structure is shown for comparison. Cations are colored purple and anions are red, while black lines mark the border of the unit cell in each structure. All crystal structure figures were created using VESTA.[100]

In addition to experimental reports, several theoretical studies on bixbyite V_2O_3 have been published in recent years, including calculations of electronic and magnetic properties, intrinsic and extrinsic defects, and phase stabilities. Using GGA+U and hybrid density functional theory (DFT) calculations, Wessel *et al.* compared the energetics of the known polymorphs of V_2O_3 along with other defective fluorite-type structures, confirming the metastable nature of the bixbyite polymorph.[87] Antiferromagnetic ordering minimized the energy of the system and led to the formation of a band gap, properties which were confirmed by previous experimental work by the same group.[29] Sarmadian *et al.* recently published a detailed study on p-type dopants in bixbyite.[99] Using a hybrid HSE06 functional, magnesium was found to be a shallow acceptor and therefore Mg-doped bixbyite is theorized to be a p-type conductor. Vanadium vacancies were also found to be shallow acceptors and may also result in p-type conductivity. To understand the very low oxygen partial pressures required to stabilize the bixbyite phase in their group's previous work,[29] Reimann *et al.* also used DFT, with both GGA and hybrid functionals, to study intrinsic defects in bixbyite.[101] The formation of oxygen interstitials in the 16c Wyckoff position was found to be favorable under ambient conditions, and an oxygen partial pressure of 10^{-17} bar was estimated to be required to thermodynamically favor the formation of stoichiometric bixbyite under their

reaction conditions. In our previous publication, we noted a change in crystal structure of bixbyite V_2O_3 nanocrystals upon air exposure, thought to be due to oxidation.[48]

Here, we explore the oxidation of bixbyite nanocrystals in detail, using *in situ* x-ray diffraction (XRD) to observe structural changes in real time and complementing the experimental findings with DFT calculations. The oxidation process is found to be reversible upon heating in inert atmosphere at moderate temperatures (>325°C), thereby establishing the possibility for use in low-temperature oxygen storage applications, where oxygen is reversibly stored and released, *e.g.* for gas separation or to carry out catalytic processes.[102–104]

3.2.1 Synthetic Methods

In a typical synthesis using standard Schlenk line techniques, a 50 ml three-neck flask containing 0.265 g (1 mmol) vanadyl acetylacetonate (Strem Chemicals, 98%), 1.07 g (4 mmol) oleylamine (Sigma Aldrich, 70%), and 1.13 g (4 mmol) oleic acid (Sigma Aldrich, 98%) in 8 ml squalane (Sigma Aldrich, 99%) was degassed under vacuum at 110°C for 1 hour. The mixture was then heated, under nitrogen flow, to 370°C and held at this temperature for 1 hour. The nanocrystals were cleaned by repeated flocculation with isopropanol and redispersion in hexanes or toluene.

3.2.2 Transmission Electron Microscopy

Nanocrystals were drop cast onto silicon nitride grids from a dilute suspension in hexanes and allowed to dry. Grids were heated in air at 125°C for 2 hours to transform to the oxidized phase, then annealed in nitrogen at 325°C for 1 hour to reduce. Low resolution images were acquired using a JEOL-2010F microscope with a Schottky field emission gun operating at 200 kV and equipped with a CCD camera.

3.2.3 X-ray Diffraction

Nanocrystals in hexanes were drop cast onto silicon substrates to create films. These films were annealed in a Thermo Scientific Lindberg Blue M Mini-Mite tube furnace open to air at 125°C for 0, 10, 20, 30, 40, and 50 minutes, resulting in increasing levels of oxidation. XRD patterns of these films were collected at the Stanford Synchrotron Radiation Lightsource on beamline 2-1. The diffractometer, equipped with Huber 2-circle goniometer and a high-resolution crystal-analyzer detector, was operated at 12 keV ($\lambda = 1.033$ Å) in reflection mode with the sample under helium flow. Scans were obtained between $2\theta = 10^\circ$ to 44° with a step size of 0.01° and time per step of 1 second. Scans were repeated 3 times then averaged. Rietveld refinement was performed on the data using the TOPAS 4.2 program.

3.2.4 *In situ* X-ray Diffraction

In situ XRD was performed on beamline X20A at the National Synchrotron Light Source at Brookhaven National Laboratory. The diffractometer was operated in reflection mode, with

a molybdenum sample heater, at an energy of 8.0645 keV (λ = 1.537 Å). Real time scans were collected using a 640-pixel linear detector centered at Q = 2.25 $Å^{-1}$ and positioned such that a Q range of 1.4 $Å^{-1}$ was surveyed during oxidation, corresponding to a resolution of 0.0022 $Å^{-1}$/pixel. Oxidation was observed while the sample was open to air and heated to temperatures between 100 and 170°C. To observe the reduction of bixbyite, a beryllium dome was affixed to the stage and purged with helium. Samples were then heated to between 250 and 400°C. Integration time varied between 1 to 5 seconds, depending on the speed of transformation, and continued over the course of transformation.

3.2.5 Thermogravimetric Analysis

TGA was done using a Mettler Toledo TGA/DSC 1. To prepare the samples, several milligrams of clean nanocrystals in hexanes were drop cast into alumina crucibles and the solvent was allowed to evaporate. Experiments were run in nitrogen or air at a flow rate of 50 ml/min and temperature ramp rate of 20°C/min.

3.2.6 X-ray Photoelectron Spectroscopy

XPS measurements were done using a Kratos Axis Ultra DLD X-ray photoelectron spectrometer with an aluminum X-ray source. The spectrometer was equipped with a series of chambers and a capsule, known collectively as ROX interface, which allow for air-free transfer from a glove box. XPS spectra were calibrated to the O 1s peak at 530 eV following the method of Silversmit *et al.*[105] High resolution spectra of the V $2p_{3/2}$, V $2p_{1/2}$, and O 1s peaks were acquired for samples annealed in air at 125°C, then analyzed using the CasaXPS software package. The peak at ~527 eV corresponds to a vanadium satellite while the peak at ~532 eV can be assigned to the oxygen-containing oleate ligands bound to the surface of the nanocrystals.[105,106]

3.2.7 Density Functional Theory

DFT[107,108] calculations were performed using the Vienna Ab initio Simulation Package (VASP) with a plane-wave basis set expanded up to a cutoff energy of 550 eV.[109,110] The projector augmented wave (PAW) method was used, treating 13 valence electrons for vanadium ($3s^2 3p^6 4s^2 3d^3$) and 6 valence electrons for oxygen ($2s^2 2p^4$).[111,112] Exchange-correlation effects were treated within the GGA+U formalism, employing the PBEsol functional[113]. As in previous publications, the Liechtenstein correction scheme, with U=2.8 and J=0.93, was initially applied to vanadium 3d states during preliminary testing and static energy mapping. Later, for the nudged elastic band and defect formation energy calculations, a Dudarev scheme with a Hubbard U value of 2.2 eV was used as it was found to more accurately describe the relative energetics and band structure of the V_2O_3 phases, as shown in Figure B.8. For the 80-atom bixbyite unit cell, Brillouin zone integration was done on a Γ-centered 3x3x3 k-point mesh, while 4x6x6 and 6x6x2 k-meshes were used for the monoclinic and corundum phases, respectively. Spin-polarized calculations were done with antiferromagnetic ordering of vanadium 3d electrons for the monoclinic and bixbyite polymorphs. Atom positions were relaxed until residual forces became less than 0.01 eV/Å and the Birch Murnaghan equation

was used to obtain the equilibrium lattice parameter.[114] The transition path for oxygen interstitial diffusion was explored without spin polarization using the climbing-image nudged elastic band method.[115,116] Atom positions within each image were relaxed until the forces became less than 0.03 eV/Å. Further details on DFT calculations are included in Appendix B.

3.3.1 Structural Changes in Bixbyite V_2O_3 Upon Oxidation

Upon exposure to air, the crystal structure of the bixbyite nanocrystals changes gradually over the course of weeks at room temperature, as observed by XRD. The change is accelerated at higher temperatures, occurring over the course of approximately an hour at 125°C, eventually resulting in a phase transformation to an unknown phase of vanadium oxide with no obvious changes in particle shape and size (Figure 3.2a & b, Figure B.1). Before this transformation occurs, XRD peaks shift to lower Q values while some peaks decrease in intensity, suggesting lattice expansion and changes in atomic positions, respectively. This evolution is shown for samples heated in air at 125°C, by both *ex situ* and *in situ* XRD, in Figure 3.2c, d, & e. To support this interpretation, Rietveld refinement was performed on XRD scans of bixbyite NCs annealed in air at 125°C for 0, 10, 20, 30, and 40 minutes (Figure B.2). These results, shown in Figure 3.2f, confirm that the cubic lattice parameter increases while vanadium located in the 24d Wyckoff positions in bixbyite shift location within the unit cell with increasing annealing time. This shift in vanadium position can also be described as the structure becoming more "fluorite-like," an indication that the vacant 16c Wyckoff positions may be filled by oxygen interstitials during the process. Thermogravimetric analysis (TGA) also shows an increase in weight when bixbyite is heated in air yielding further confirmation of oxygen insertion into the bixbyite lattice.[48]

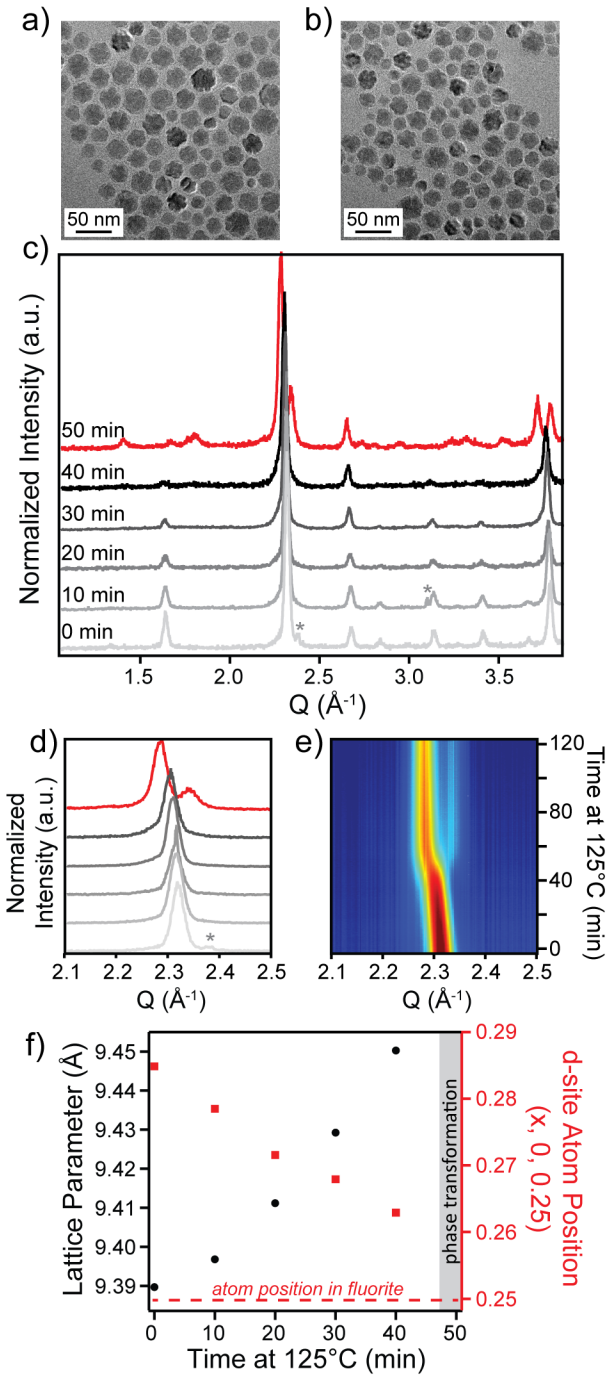

Figure 3.2: Transmission electron microscopy images of bixbyite NCs a) as synthesized and b) after annealing at 125°C in air for 2 hours. c) XRD scans of bixbyite annealed in air at 125°C for 0, 10, 20, 30, 40, and 50 minutes (with impurity peaks from the Si substrate marked with *) with d) a zoomed in image of the (222) peak, e) *in situ* XRD pattern centered at the (222) bixbyite peak held at 125°C in air, and f) results of Rietveld refinement for films annealed at 125°C for 0, 10, 20, 30, and 40 minutes showing lattice parameter (left/black) and position of the d-site vanadium (right/red) as a function of annealing time.

3.3.2 Static DFT Mapping of Oxygen Interstitial Sites

Static DFT calculations were used to map the energy landscape of the likely interstitial oxygen positions in the bixbyite unit cell. The total energy of the system upon moving one interstitial oxygen along channels parallel to the edge, face diagonal, and body diagonal of the bixbyite unit cell was calculated and the results are shown in Figure 3.3. Since test calculations revealed that the trends in interstitial oxygen position were insensitive to magnetic order and spin polarization (Figure B.9), these parameters were not included in the calculations to reduce computational cost.

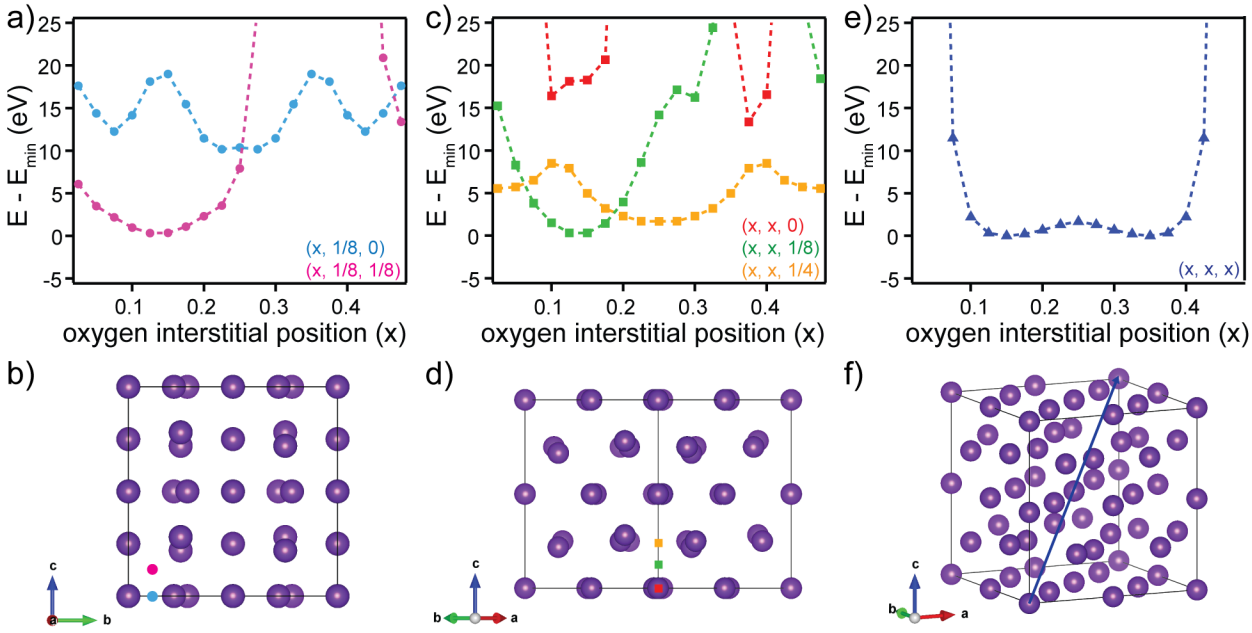

Figure 3.3: Energy of the bixbyite unit cell with an oxygen interstitial placed along channels parallel to the a) cube edge, c) face diagonal, and e) body diagonal, referenced to minimum energy value. Channels marked in structures below (b, d, f). Positions are indicated in terms of fractional coordinates in the cubic unit cell.

As expected, and previously assumed without energy mapping in other work, the most stable positions for oxygen interstitials are the inherently vacant 16c Wyckoff positions in the Ia-3 space group.[101] This is evident from the minima found at the fractional coordinates (0.15, 0.15, 0.15) and (0.35, 0.35, 0.35) in Figure 3.3e. A mirrored version of the trend was observed along the second half of the body diagonal (between the body center and opposite cube corner), with minima also existing at (0.65, 0.65, 0.65) and (0.85, 0.85, 0.85). These 16c sites can also be described as those in which oxygen is vacant relative to the fluorite structure, therefore these results support the experimental observation that the bixbyite crystal structure becomes more similar to fluorite upon oxygen incorporation.

3.3.3 Charge Compensation by Local Oxidation of Vanadium

To maintain charge neutrality upon oxidation, the incorporation of negatively charged oxygen interstitials must be followed by the creation of holes in the vanadium sublattice due to internal charge transfer from vanadium to oxygen. Holes in the vanadium sublattice can either be localized on a vanadium cation and give rise to p-type polaronic conduction, or delocalized in the valence band, yielding a strongly correlated p-type metal. Given the small energy differences between vanadium oxidation states, localized charge compensation at vanadium lattice sites is expected, in which two vanadium atoms oxidize for every oxygen interstitial present, as shown in Kröger-Vink notation below.

$$2V_{\mathsf{V}}^{\mathsf{X}} + \frac{1}{2}O_2(g) \rightarrow 2V_{\mathsf{V}}^{\cdot} + O_{\mathsf{i}}^{\prime\prime} \tag{3.1}$$

Indeed, X-ray photoelectron spectroscopy (XPS) confirms the presence of V^{4+} following air exposure. This is evident by a second peak contribution within the envelope of the V 2p doublet, which increases in intensity with annealing time at 125°C in air (Figure 3.4).

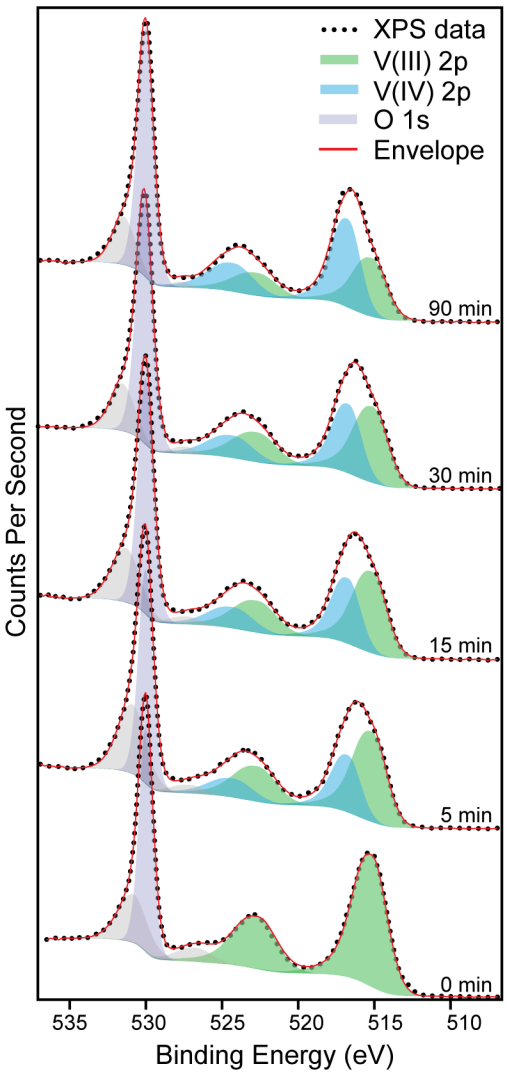

Figure 3.4: XPS scans of bixbyite films annealed in air at 125°C for 0, 5, 15, 30, and 90 minutes. The contribution of vanadium in the 3+ and 4+ oxidation states is indicated by the green and blue peaks, respectively.

3.3.4 Kinetics of Oxidation and Phase Transformation

The course of the bixbyite oxidation process that ultimately leads to phase transformation was followed in detail by carrying out *in situ* XRD experiments, like that shown in Figure 3.2e, at several temperatures. Figure 3.5a maps the position of the (222) diffraction peak from this data as a function of annealing time at 100°C, 125°C, and 150°C. The rate of peak shift, and therefore volume expansion, increases with temperature up to the point of transformation, where the single peak at Q ≈ 2.3 $Å^{-1}$ splits into a peak and shoulder. No further structural changes are observed after this transition. Figure 3.5b shows weight gain, monitored by TGA, in bixbyite nanocrystals as a function of time under the same annealing conditions as *in situ* XRD. As temperature is increased, weight gain occurs at a faster rate.

However the percentage of weight gain at transformation, determined from the maximum change in shoulder peak intensity (Figure B.3) and marked with green circles in Figure 3.5a & b, is independent of annealing temperature. This suggests that the transformation is triggered once a critical oxidation level is reached. Taking the lattice as cubic up to the point of transformation and ascribing all weight gain to oxygen interstitial incorporation, *in situ* XRD and TGA data can be combined to track unit cell volume as a function of oxygen interstitial concentration. A nonlinear trend is apparent with increasing expansion as oxidation proceeds (Figure 3.5c). The trend is consistent for annealing at 100°C and 125°C, while the data appear slightly shifted for 150°C annealing. We attribute this shift to partial oxidation during the ramp to 150°C, which would result in an underestimation of oxygen interstitial content. Based on the weight gain of about 1.8% at transformation, it can be reasoned that the bixbyite lattice can accommodate two oxygen interstitials per unit cell, after which the structure becomes unstable and transformation occurs. This result suggests that the oxidized phase has a stoichiometry between that of V_2O_3 and V_3O_5, the adjacent phase in the V-O phase diagram. However, efforts to identify its crystal structure were unsuccessful, as it indexes to no known vanadium oxide phase or fluorite derivative.

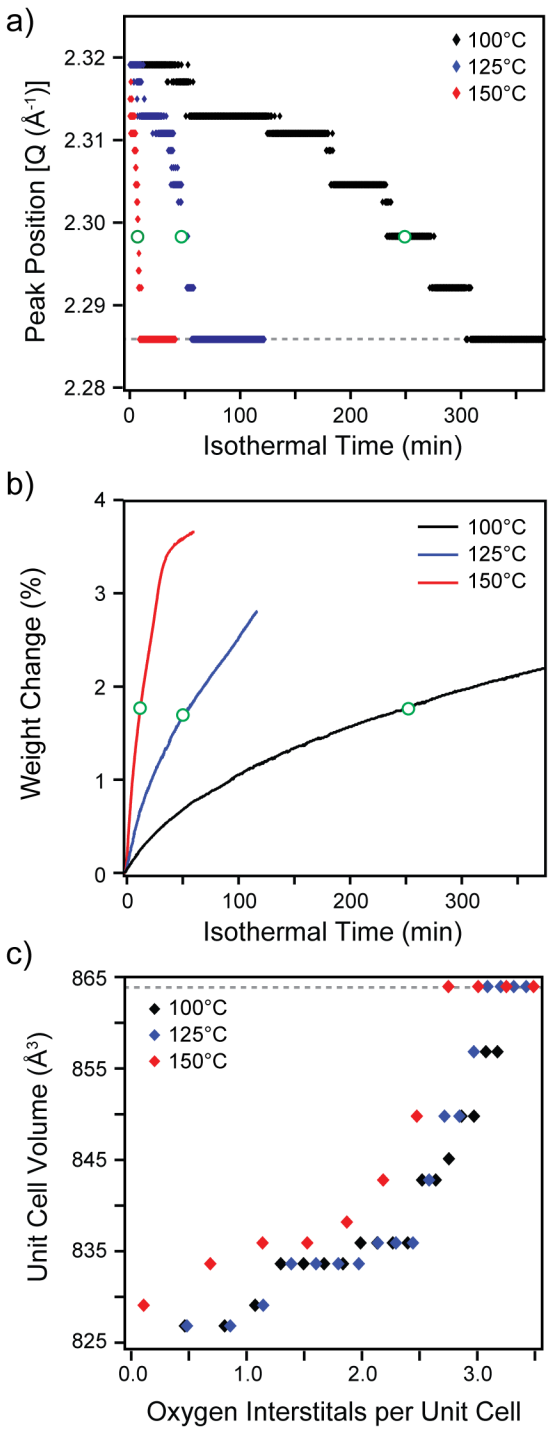

Figure 3.5: Kinetic progress of the oxidation of bixbyite V_2O_3 nanocrystals followed *in situ* during air annealing. a) (222) peak position from *in situ* XRD data and b) TGA scans for bixbyite nanocrystals annealed in air at 100°C (black), 125°C (blue), and 150°C (red). c) Volume expansion as a function of oxygen interstitial content calculated from data in a) and b). Green circles indicate time at which transformation to unknown phase occurs, as determined from maximum change in shoulder peak intensity.

3.3.5 Oxygen Diffusion as Rate Limiting Step in Oxidation Process

The *in situ* data were also used to plot time to transformation as a function of annealing temperature, as shown in Figure 3.6a. An Arrhenius-type relation is apparent, in which transformation rate is related to temperature following:

$$k = Ae^{E_a=RT} \tag{3.2}$$

Where k is the reaction rate, A is an attempt frequency factor, E_a is the activation energy, R is the universal gas constant, and T is temperature. An activation energy and frequency factor of 98 kJ/mol (1.02 eV), and 3.1 x 10^9 s^{-1}, respectively, were extracted from the data. Activation energy is determined by the rate limiting step of the oxidation process, which may include oxygen adsorption, dissociation, intercalation, diffusion, and finally, structural transformation. Many of these potentially rate limiting processes are expected to be accelerated in materials with high surface area (*i.e.*, adsorption, dissociation, intercalation) or presenting short path lengths (*i.e.*, diffusion), so that the progression of the structure along an equilibrium pathway of progressive oxidation is greatly facilitated by the nanostructuring of the material. Oxidation happens quickly at the surface of the nanocrystal, as seen by the large concentration of charge compensating V^{4+} after only 5 minutes of annealing in Figure 3.4. Thus, it is unlikely that the processes occurring at the surface of the nanocrystal are rate limiting. Furthermore, the extracted activation energy is comparable to theoretical and experimental activation energies of oxygen diffusion in perovskite, fluorite, and bixbyite oxides, thereby suggesting that oxygen diffusion is the rate limiting step in the bixbyite oxidation process.[117–119] To support this hypothesis, the activation energy of oxygen diffusion was modeled using the climbing-image nudged elastic band method for DFT.[115,116] Neighboring minima along the body diagonal in the bixbyite unit cell, as shown in Figure 3.3e, were chosen as initial and final positions of the minimum energy pathway for oxygen migration. The resulting activation energy along this path was found to be 1.09 eV (Figure 3.6b). This result is in very good agreement with the activation energy extracted from experimental kinetics, thereby supporting the role of oxygen diffusion as the rate limiting step in the transformation process.

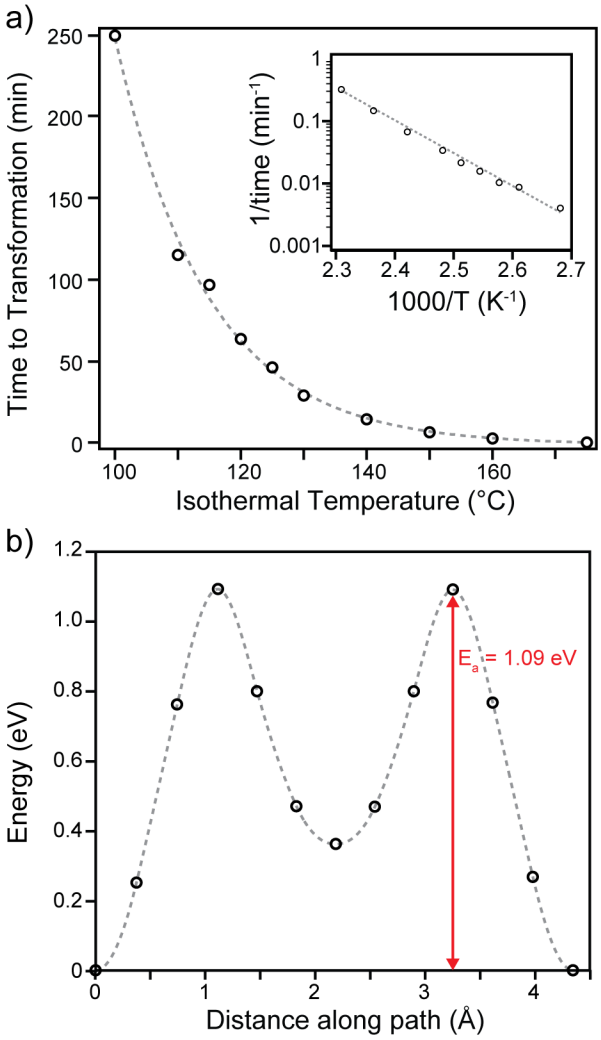

Figure 3.6: a) Time to transformation as a function of annealing temperature in air. Inset shows plot of 1000/T vs ln(1/t), yielding straight line which can be used to extract activation energy and frequency factor. b) Climbing-image nudged elastic band model of oxygen interstitial diffusion between neighboring 16c Wyckoff positions along the cell body diagonal.

3.3.6 Reversibility of Oxidation Process

Notably, the oxidation of bixbyite V_2O_3 can be reversed upon annealing in a mild reducing atmosphere, even if it has been allowed to progress past the phase transformation. Figure 3.7a shows *in situ* XRD scans from an already oxidized and transformed sample heated in helium to 325°C. The characteristic peak and shoulder of the unknown, oxidized phase merge into one peak, characteristic of the bixbyite phase, suggesting a phase transformation back to the stoichiometric phase. Indeed, the recovery of the bixbyite phase is confirmed by *ex situ* XRD while TEM images show minimal changes to particle size and shape (Figure B.1). Oxidized bixbyite was also heated under the same conditions as *in situ* XRD while weight loss was tracked by TGA. The starting weight of the sample corresponds to the weight after

oxidation at 125°C (a continuation of the data in Figure 3.5b). Upon heating in inert gas, a weight loss is indeed observed, with the maximum rate of change in weight occurring at the same time and temperature as the rapid change in peak position, approximately 13 minutes and 310°C, respectively (Figure B.6). However the final weight after reduction (≈95 wt%) is less than the initial sample weight before oxidation (100 wt%). This additional weight loss can be accounted for by the decomposition of the organic ligands bound to the surface of the nanocrystals, as evidenced by the 5 wt% loss in a pristine bixbyite sample heated under the same conditions (Figure 3.7b). The final weight of the oxidized sample is approximately equal to the final weight of the unoxidized sample, indicating that the weight gain due to oxygen insertion is completely reversed by annealing in nitrogen. Therefore, it is likely that the change in structure observed by *in situ* XRD is indeed due to reduction, wherein the phase transformation is reversed and oxygen interstitials are removed from the bixbyite lattice.

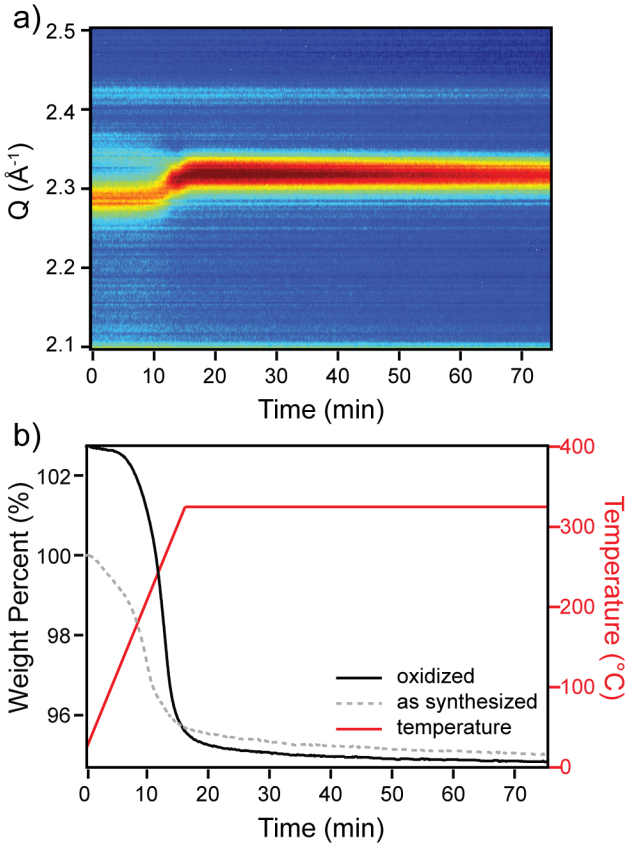

Figure 3.7: Reduction of oxidized bixbyite as observed by a) *in situ* XRD and b) TGA heated in inert gas following temperature profile in red. TGA data includes reduction of oxidized and as-synthesized bixbyite in order to account for ligand decomposition. The XRD peaks near Q = 2.1 and 2.42 $Å^{-1}$ arise from the beryllium dome required for *in situ* inert gas annealing.

Such reversibility in the oxidation process requires not only kinetic facilitation by the nanoscale nature of the material, but favorable thermodynamics that allow the system to

shift between thermodynamically favored states within the experimentally accessible range of environmental conditions. To probe the energetics of the defect formation process corresponding to oxygen insertion in bixbyite V_2O_3, DFT was used to evaluate the following equation for defect formation energy of a neutral cell[120]:

$$E_{\mathrm{defect}} = E_{\mathrm{defective\,cell}} - E_{\mathrm{perfect\,cell}} - \sum_i n_i \mu_i \tag{3.3}$$

Where μ_i is the chemical potential of species i added or removed and n_i is the number of species i added or removed (n_i <0 if removed, n_i >0 if added). For the case of an oxygen interstitial in the 80 atom unit cell of bixbyite, the equation becomes:

$$E_{O_i} = E_{V_{32}O_{49}} - E_{V_{32}O_{48}} - \mu_O \tag{3.4}$$

The total energy of a stoichiometric, relaxed bixbyite cell was subtracted from the total energy of a cell with one additional interstitial oxygen initially at a position of (0.15, 0.15, 0.15) and relaxed to (0.141, 0.142. 0.143), as calculated by DFT. The lattice parameters were fixed to simulate the dilute limit. We note that the defect-defect distance is 9.414 Å and that only subtle elastic interactions between defects in periodic images are expected. As the chemical potential of oxygen depends on pressure and temperature, it is reported as a range of achievable values. The lower bound, or reducing limit, represents the chemical potential at which the dissociation of V_2O_3 into vanadium metal and oxygen gas becomes thermodynamically favorable, whereas at the upper bound, or oxidizing limit, the maximum chemical potential of oxygen considered is the total energy of oxygen in an isolated oxygen molecule.[1] Figure 3.8 shows the defect formation energy of an oxygen interstitial at 0 K as a function of the chemical potential of oxygen.

[1]

[2]

[121]

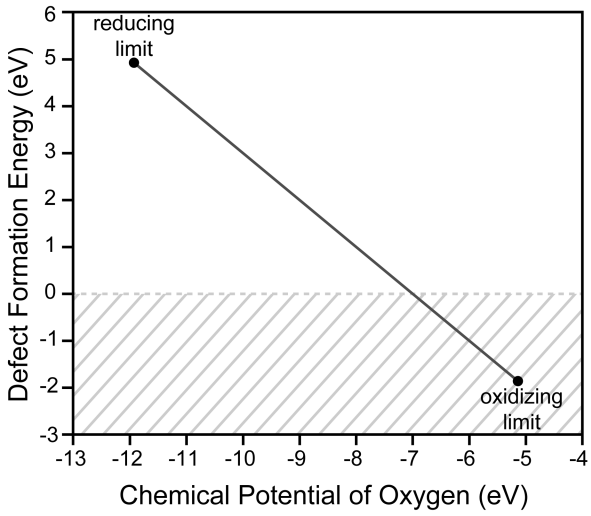

Figure 3.8: Defect formation energy of oxygen interstitial in bixbyite V_2O_3 calculated by DFT as a function of the chemical potential of oxygen for a range of experimentally accessible values. Dashed gray area indicates the region of negative defect formation energy.

The reversibility of the oxidation process observed experimentally can be understood from the calculated defect formation energy and its dependence on the chemical potential of oxygen. Under oxygen-rich conditions, oxygen has a higher chemical potential and the defect formation energy of an oxygen interstitial is negative. This result indicates that bixbyite is metastable with respect to a more oxidized phase under these conditions, which is consistent with our observation that bixbyite oxidizes spontaneously over time. Under oxygen-poor conditions (low chemical potential), the defect formation energy is positive, indicating that stoichiometric bixbyite is a stable host for oxygen interstitials. As the oxygen chemical potential decreases, either by reducing oxygen partial pressure or increasing temperature, the defect formation energy increases, ultimately leading to a decrease in the equilibrium concentration of oxygen interstitials in bixbyite. This is consistent with our observation that oxygen interstitials are removed from the lattice upon heating under inert gas flow (low pO_2), as shown by XRD and TGA in Figure 3.7. Furthermore, distinct levels of reduction can be achieved by simply varying temperature while keeping partial pressure low and fixed (Figure B.4 & B.5). In this way, oxygen content can be controlled by altering either oxygen partial pressure, temperature, or both.

3.4.1 Bixbyite V_2O_3 for Low Temperature Oxygen Storage Applications

The ability to reversibly store and release oxygen in bixbyite V_2O_3 makes it an appealing candidate for use in oxygen storage applications. Oxidation occurs both rapidly and with minimal change in crystal structure below a concentration of approximately two oxygen interstitials per unit cell. However, the most remarkable feature of bixbyite's reversible oxidation

process is the unusually low temperatures required for oxidation and reduction. For comparison, $HoMnO_3$, a hexagonal manganite material demonstrating oxidation at exceptionally low temperatures, requires an oxidation temperature of 190°C, while heating in pure O_2 gas, and a reduction temperature of 325°C.[122] Bixbyite V_2O_3 demonstrates nearly the same oxygen storage capacity at transformation (~1.8%) while operating at a lower temperature and pO_2. In addition to aiding in the stabilization of the phase, the high surface to volume ratio in bixbyite NCs is expected to result in faster diffusion, and therefore faster switching kinetics, than in the bulk.[123] Furthermore, while most oxygen storage materials under investigation today contain rare earth elements, vanadium oxide is made up of earth-abundant elements.

To pave the way toward practical applications, further work is needed to improve cyclability of the oxidation and reduction processes. Initial tests show diminishing oxygen storage capacity upon cycling, leading to an eventual loss of bixbyite stabilization (Figure B.7). This may be associated with the thermal decomposition of the binding organic ligands at the surface of the bixbyite nanocrystals which may alter surface energy and, therefore, stability of the phase. Repeated expansion and transformation induced by oxidation may also lead to degradation of the structure. Indeed, cyclability is improved when oxidation is not allowed to progress past the point of structural transformation. These problems may be mitigated by doping or alloying with elements that stabilize the metastable structure (as in yttrium-stabilized zirconia) or minimize defect-induced strain. The improved oxygen storage capacity and cyclability of zirconia-ceria solid solutions, compared to pure ceria, is an example of the latter. This improvement has been ascribed to the small size of the zirconium ion, which counteracts the strain associated with the formation of trivalent cerium during reduction.[124]

3.4.2 Defect Induced Lattice Expansion in Oxides

Lattice expansion in fluorite and defective fluorite-type oxides is not a new occurrence, but contrary to what is observed in V_2O_3, this tends to occur as a result of oxygen vacancy formation. Termed chemical expansion, this is a well-known phenomenon, due in part to the stresses this type of expansion can induce in energy conversion devices such as solid oxide fuel cells.[125] Charge compensating cation reduction, and the resulting increase in cationic radius, is the dominant mechanism leading to expansion in oxygen deficient fluorites and perovskites. Although relaxation near the vacancy causes some contraction, the effect is not as pronounced and therefore the net result is still expansion. Similarly, in bixbyite V_2O_3, two opposing influences on lattice parameter are expected. The presence of excess oxygen is expected to favor expansion to accommodate lattice strain while the oxidation of vanadium, required for charge compensation, favors contraction. This is clear from the ionic radius of vanadium, which is 0.64 Å in the 3+ oxidation state and 0.58 Å in the 4+ state.[126] If change in cation size dominates the change in lattice constant, as it does in the case of chemical expansion observed in other fluorite-type structures, one might expect the net effect of these competing influences to favor contraction, however this is not observed. Instead, low concentrations of oxygen interstitials have very little effect on the lattice, as shown in Figure 3.5c, while larger concentrations result in expansion. We propose that the two competing mechanisms favoring expansion and contraction, strain accommodation and cation oxidation, respectively, balance and compensate each other at low oxidation levels.

Upon further oxidation however, expansion due to accommodation of extra atoms in the lattice dominates. DFT calculations of unit cell volume as a function of oxygen interstitial content show a similar trend (Figure B.11).

3.4.3 Comparison to Other Bixbyite Oxides and Polymorphs of V_2O_3

The reversible oxidation observed in bixbyite is not expected to occur in the other polymorphs of V_2O_3. Although vanadium is known for its ability to switch oxidation states, and could thereby compensate for the extra charge introduced by oxygen interstitials in any crystal phase, the corundum and monoclinic phases likely have insufficient space in the lattice to accommodate oxygen interstitials at reasonable formation energy. Corundum, for example, has a hexagonal close-packed oxygen sublattice that leaves little room for excess oxygen, quite unlike the inherently vacant sites in the bixbyite unit cell.[127] The calculated density of the bixbyite phase is 4.81 g/cm^3, as compared to the much higher densities of the corundum and monoclinic phases, which are 5.02 g/cm^3 and 4.98 g/cm^3, respectively.[22,81] Alternatively, other oxides with the bixbyite structure, such as indium oxide (In_2O_3), may be unable to easily compensate for the high levels of charge introduced by oxygen interstitials. As indium in the 3+ oxidation state has a stable [Kr]4d^{10} electron configuration, compensation by cation oxidation is highly unlikely. Furthermore, delocalized compensation, resulting in hole formation and p-type conductivity, is possible in semiconductors like In_2O_3 but never observed. Rather the formation of oxygen vacancies is known to be favorable in In_2O_3, leading to intrinsic n-type conductivity.[128]

It is therefore a combination of bixbyite's open structure and vanadium's ability to change oxidation state that hold the key to bixbyite V_2O_3's ability to accommodate large oxygen excesses under mild oxidizing conditions. In this regard, its nanocrystalline morphology, which plays a role in stabilizing the less dense phase in addition to offering short diffusion paths, is clearly important. Lacking direct experimental data, however, it is unclear whether this reversible process could occur effectively in bulk bixbyite.

Here we report reversible oxygen incorporation in metastable, bixbyite In_2O_3 nanocrystals. Oxygen interstitials fill the inherently vacant 16c positions in bixbyite, as suggested by Rietveld refinement results and supported by DFT calculations, making the structure more like that of fluorite. Increasing oxidation in bixbyite results in lattice distortion and expansion, eventually inducing a phase transformation to an unidentified phase. Combined XRD and TGA data reveals a nonlinear chemical expansion, with minimal structural changes upon initial oxidation and rapid expansion up to a critical oxidation level of 1.8 weight %, corresponding to about 3 oxygen interstitials per unit cell, at which point transformation occurs. The rate of transformation follows an Arrhenius relationship, which was used to extract the activation energy of the process from *in situ* XRD data. This activation energy is in good agreement with the calculated activation energy of oxygen diffusion determined by DFT, and therefore the oxidation process is reasoned to be diffusion limited. Finally, oxidation

and transformation were shown to be reversible by annealing in inert gas at 325°C, with the structure reverting back to that of stoichiometric bixbyite and weight loss indicating the removal of interstitial oxygen from the lattice. The reversibility of the process can be understood by the dependence of defect formation energy on the chemical potential of oxygen, which can be controlled by varying oxygen partial pressure and temperature. This study motivates the continued effort in stabilizing a bulk form of bixbyite V_2O_3 in order to elucidate the influence of nanosize effects on reversible oxidation, as well as the further exploration of the strange and fascinating properties of this metastable oxide.

3.5.1 Acknowledgments

The authors acknowledge Jean L. Jordan-Sweet, Badri Shyam, and Hugo Celio for assistance with XRD and XPS measurements, and Penghao Xiao, Sandra H. Skjærvø, Gerhard Olsen, and Tor Grande for helpful discussions. Use of the National Synchrotron Light Source, Brookhaven National Laboratory, was supported by the U.S. Department of Energy, Office of Science, Office of Basic Energy Sciences, under Contract No. DE-AC02-98CH10886. Use of the Stanford Synchrotron Radiation Lightsource, SLAC National Accelerator Laboratory, is supported by the U.S. Department of Energy, Office of Science, Office of Basic Energy Sciences under Contract No. DE-AC02-76SF00515. Computational resources were provided by NOTUR (The Norwegian Metacenter for Computational Science) through grant no. NN9264K. Additional support to DJM from the Welch Foundation (F-1848) is acknowledged. This material is based upon work supported by the National Science Foundation Graduate Research Fellowship under Grant No. DGE 1106400. AB's extended research visit in Norway was supported by the NSF Graduate Research Opportunities Worldwide (GROW) Program in collaboration with the Research Council of Norway.

Reproduced in part with permission from Amy Bergerud, Gabriel LeBlanc, Clayton Dahlman, and Delia J. Milliron "Electrochemically-Induced Transformations in Vanadium Dioxide Nanocrystals" Submitted .

Bulk vanadium dioxide (VO_2) undergoes a reversible metal-to-insulator transition (MIT) at approximately 68°C, at which point the low-temperature monoclinic phase transforms to the high-temperature rutile phase.[2] This structural transformation is accompanied by dramatic changes in the oxide's electronic and near infrared (NIR) optical properties.[8,9] Due to the relatively low temperature of MIT, VO_2 has also been investigated for a variety of applications including solid-state memory devices,[3,4] sensors,[5] and smart-windows.[6,7] In addition to using direct thermal energy to trigger the transformation, this MIT phenomenon has also been observed in VO_2 using "all-optical"[129] and "all-electrical"[130–133] methods. In 2012, Nakano and co-workers observed a MIT in VO_2 via ionic liquid gating using an electric double layer transistor geometry consisting of a thin film of VO_2 as the channel and an ionic liquid as the gate.[134] Application of a gate voltage resulted in a lowering of the MIT temperature across the channel, with sufficiently high voltages leading to a stabilization of the metallic state across all temperatures. At the time, this change in conductivity was attributed to a transformation to rutile phase. The authors reasoned that electrostatic charging at the VO_2 surface triggered collective carrier delocalization and transformation in the bulk of the film. In a similar configuration in 2013, however, Jeong and co-workers found that ionic liquid gating does more than electronically charge the VO_2 film, reporting that metallization was accompanied by the generation of oxygen vacancies within the material.[135] Subsequent studies by the same group found that though VO_2 films underwent significant structural changes during gating,[136] the vacancy-rich phase was not rutile and therefore metallization under ionic liquid gating is distinct from the transformation to the metallic

rutile phase.[137] Additionally, metallization was only obtained when the epitaxial VO_2 film was oriented such that the rutile c-axis was partially or fully perpendicular to the surface, allowing oxygen atoms to diffuse in and out of the film along chains of edge-sharing VO_6 octahedra.[136]

Nanocrystals (NCs) are expected to facilitate oxygen diffusion due to their high surface-to-volume ratios, which present many pathways for diffusion in and out of the lattice, and their small sizes, which minimize diffusion distances. We therefore hypothesized that electrochemical control would be observed in films of VO_2 NCs more readily than in epitaxial thin films and without the need for orientation control. Despite the interest in VO_2 NCs for their desirable optical properties[138] and potential for size-dependent phase behavior,[139] their chemical synthesis remains challenging. The complicated phase diagram of the vanadium-oxygen system contains many stable and metastable compounds and phases, thus making stabilization of a particular phase difficult.[1] Nevertheless, several routes to nanostructured VO_2 with varying degrees of morphology control have been reported including hydrothermal synthesis[65,42] and polymer assisted deposition.[140] Optical quality films suitable for spectro-electrochemical investigation can be readily prepared from colloidal nanocrystals,[141,142] thus making this approach to VO_2 NCs most attractive. Unfortunately, a direct colloidal synthesis of VO_2 NCs has not yet been reported. In the closest example, Paik and co-workers reported the conversion of VO_x colloidal NCs with an unidentified crystal structure into VO_2 films using a rapid thermal annealing process; however nanocrystallinity was lost upon conversion, resulting in the formation of ordinary, densified thin films.[143]

Building on our recent report of the colloidal synthesis of metastable bixbyite V_2O_3 NCs,[48] here we report the development of a low-temperature, oxidative annealing process to convert films of V_2O_3 NCs to VO_2 while maintaining nanocrystallinity and high optical quality. Upon electrochemical reduction, these NC films transform from monoclinic phase to an IR blocking, oxygen deficient monoclinic state, consistent with the effects of ionic liquid gating on VO_2 thin films. However, upon further reduction or reduction from the IR blocking rutile phase, we observe a reversal in this IR darkening, leading to a new IR transparent state that, according to Raman and X-ray absorption spectroscopy (XAS), is oxygen deficient and no longer monoclinic or rutile phase. Hence, the enhanced gating effect in our VO_2 NC films can instigate a reversible electrochemically-driven phase transformation that has not been revealed by gating epitaxial thin films with ionic liquid electrolyte.

4.2.1 Synthetic Methods

Bixbyite V_2O_3 NCs were prepared following our previously described colloidal synthesis.[48] Briefly, vanadyl acetylacetonate (1 mmol) (Strem Chemicals, 98%), oleylamine (4 mmol) (Sigma Aldrich, 70%), oleic acid (4 mmol) (Sigma Aldrich, 90%), and squalane (8 mL) (Sigma Aldrich, $\geq$95%) were mixed and degassed at 110 °C. The suspension was then heated under nitrogen flow to 370 °C for 1 hour before repeated washing with isopropanol and hexanes. The cleaned NC ink (~50 mg/mL) was then deposited onto cleaned ITO coated glass substrates or doped silicon substrates via spin coating. Briefly, 20 µL of the NC ink was added to a

2x2 cm substrate, which was then spun at 1000 rpm for 90 s and dried at 4000 rpm for 30 s. Film thickness was determined to be 83 ± 3 nm using a Veeco Dektak 6M Stylus Profilometer. The as deposited bixbyite V_2O_3 NC film was then converted to monoclinic VO_2 by annealing in a slightly oxidative environment. In this study, the films were annealed at 375 °C in 167-250 ppm O_2 atmosphere for 30-60 minutes.

4.2.2 X-ray Diffraction

In situ XRD in air was performed on beamline X20A at the National Synchrotron Light Source at Brookhaven National Laboratory. The diffractometer was operated in reflection mode, with a molybdenum sample heater, at an energy of 8.0645 keV (λ = 1.537 Å). Scans were collected every second while a film of bixbyite NCs was heated in air to 600°C at a rate of 1°C/sec. *In situ* XRD in 250 ppm O_2 in N_2 was performed at the Norwegian University of Science and Technology on a Bruker D8 Advance diffractometer with Cu Kα radiation, Våntec-1 detector, high temperature stage and gas chamber. Scans were collected every 4-6 minutes with a step size between 0.1 and 0.25°, depending on the 2θ range. *Ex situ* XRD was performed using a Rigaku R-axis Spider diffractometer with an image plate detector and Cu Kα radiation. Films were prepared on silicon substrates and data was collected in reflection mode over 10 minutes of exposure.

4.2.3 Transmission Electron Microscopy

Transmission electron microscopy images were collected using a JEOL 2010F TEM with a Schottky field emission source operating at 200 kV. The sample was prepared by drop casting a dilute suspension on V_2O_3 nanocrystals in hexanes on a silicon nitride TEM grid. TEM grids were annealed under the same conditions as films (375°C, 1 hr, 250 ppm O_2) to convert to VO_2 NCs.

4.2.4 Variable Temperature Spectroelectrochemistry (VT-SEC)

Electrochemical analysis of the VO_2 films was performed using a Bio Logic VMP3 Potentiostat. The VO_2 film was set as the working electrode, platinum foil as the counter electrode, and Ag/Ag^+ as the reference electrode. Note, the Ag/Ag^+ electrode was calibrated against a Li/Li^+ electrode and was found to be -3.00 V vs Li/Li^+. Voltages in this paper are reported relative to a NHE electrode. The three electrodes were housed in a custom built cell that enabled a minimal pathlength through the electrochemical mediator consisting of 0.1 M tetrabutylammonium bis-trifluoromethanesulfonimidate (TBA-TFSI) (Sigma Aldrich, ≥99.0%) in propylene carbonate (Sigma Aldrich, 99.7%). Spectroscopy (400 – 2200 nm) was performed with an ASD Inc. PANalytical spectrometer operating in transmission mode, which was directed through the film using fiber optic cables. Finally, the temperature was controlled using a TC-720 temperature controller with a Peltier thermoelectric element with a center hole (TE Technologies) to enable light through the system. The temperature was monitored with an epoxy bead thermistor (TE Technologies). For the experiments described in the main text, the entire VT-SEC set-up was housed in an argon glovebox (Figure C.1).

Experiments were also performed in air by using a similar set-up outside the glovebox and bubbling the electrolyte with compressed air for 2 hours.

Respresentative darkening, bleaching, and bleached samples were prepared on silicon substrates for *ex situ* analysis. A sample in the process of darkening in the IR was prepared by applying a small bias for a long time (-0.5V for 7.5 hrs), thus preventing overshoot into the bleached state. A film in the process of bleaching, after first darkening, was prepared by applying a large bias for a short time (-2V for 30 min), and finally, the fully bleached state was accessed by applying a bias from the rutile phase until saturation (-1.5V for 10 min at 100°C).

4.2.5 Raman Spectroscopy

Raman spectroscopy was performed on a Horiba Jobin Yvon LabRAM ARAMIS spectrometer using a 532 nm laser. Electrochemistry of the VO_2 films on doped silicon substrates was performed in a glovebox before transfer to the Raman instrument using a Linkam LTS420 cell. The Linkam cell not only prevented rapid oxygen contamination, but also enabled analysis at temperatures above and below the MIT temperature. Measurements were taken under a 50x long working distance microscope objective lens.

4.2.6 X-ray Absorption Spectroscopy

XAS spectra were collected at beamline 10.3.2 of the Advanced Light Source. Vanadium K-edge spectra were collected in fluorescence mode using an Amptek silicon drift fluorescence detector 1-element (XR-100SDD) collected at ambient temperature (25°C) for all spectra except the rutile sample, which was heated to 100°C in air using a Peltier heating element affixed to the back of the sample substrate during measurements. The darkening, bleaching, and bleached films were electrochemically reduced then sealed with a mylar film in an argon glovebox before XAS measurement to prevent air exposure. A Si (111) monochromator was used with a resolving power ($\Delta E/E$) of 7000 at 10 keV. More details about the beamline can be found in reference by Marcus *et al.*[144] V K-edge EXAFS were collected in the energy range of 5360 to 5980 eV. Each XAS spectrum was averaged from two consecutive scans, each about 45 minutes long. The experimental data was energy calibrated to a vanadium foil measured in transmission mode. Preliminary analysis to scan average and background the pre- and post-edge features was performed using software developed at ALS beamline 10.3.2, and normalization and post-processing of $\mu(E)$ data was performed using Athena and Artemis from the Demeter package (version 0.9.24). A Hanning window in the k-space range of 2.6-10.6 $Å^{-1}$ was applied to the Fourier transform into real space. Full XAS and k-space EXAFS is presented in Figure C.10.

4.3.1 *In Situ* Observation of V_2O_3 Oxidation

As discussed in our previous publications, bixbyite V_2O_3 NCs oxidize when heated in air. At low temperatures, oxygen fills interstitial sites in the bixbyite lattice, eventually resulting

in a transformation to a new phase of vanadium oxide. At these low levels of oxidation, NC morphology remains largely unchanged and oxidation is reversible upon annealing in inert atmosphere at slightly elevated temperatures. At higher temperatures in air, bixbyite transforms irreversibly to V_3O_7 or V_2O_5, accompanied by a complete loss in nanocrystallinity (Figure A.10).

In order to understand the progression of bixbyite oxidation, *in situ* XRD was performed on NC films heated in air (Figure 4.1a) at 1°C/sec. As expected, initial heating at low temperatures results in a subtle phase transformation from bixbyite to an unknown oxidized phase, indicated by a shift in the peaks located at 33° and 38° to lower 2θ and a disappearance of the peaks located at 23° and 40°. At approximately 350°C, the peaks disappear, likely caused by amorphization of the material, followed by the crystallization of a mixture of VO_2 and V_3O_7. The peaks indicative of VO_2 eventually disappear as temperature continues to increase, leaving only V_3O_7, then a mixture of V_3O_7 and V_2O_5, and finally pure V_2O_5. As this progression occurs, the peak widths also appear to decrease, indicating the expected increase in crystallite size. Surprisingly however, the peak widths corresponding to VO_2 are much broader than those of V_3O_7 and V_2O_5. This suggests that nanocrystallinity in retained in vanadium dioxide in this instance.

Our *in situ* results in air show that VO_2 can be obtained by annealing V_2O_3 nanocrystals in air, however the phase only exists over a short temperature span and it is not phase pure. Therefore, in an attempt to obtain phase pure VO_2, bixbyite V_2O_3 was annealed at a lower partial pressure of oxygen. This has the effect of altering the oxygen chemical potential of the system, and thus, the thermodynamics. Films of bixbyite NCs were heated in 250 ppm O_2 in N_2 at a rate of 0.1°C/sec, nearly three orders of magnitude less oxygen than in air, and the resulting transformations were tracked *in situ* (Figure 4.1b). As expected, oxidization proceeds differently at this lower partial pressure of oxygen. After the initial formation of the unknown oxidized phase at approximately 280°C, VO_2 is observed as a pure phase, initially forming at ≈360°C and persisting for approximately 50°C before the another unknown phase begins to crystallize. VO_2 peaks are initially broad then narrow as temperature increases, indicating a coarsening of the VO_2 crystallites.

4.3.2 Synthesis of Nanocrystalline VO_2 via Controlled Oxidation of V_2O_3 NCs

Following our previously published method, V_2O_3 colloidal NCs with a metastable bixbyite crystal structure were first synthesized via aminolysis reaction using standard Schlenk line techniques.[48] Films of V_2O_3 NCs were prepared via spin or drop casting from solvent then converted to VO_2 via a mild annealing treatment at low oxygen partial pressure (375°C, 250 ppm O_2 in N_2). Transmission electron microscopy (TEM) was used to observe the morphology of the NCs before and after conversion (Figure 4.2a & b). The as prepared V_2O_3 NCs are well-separated with an average diameter of approximately 25 nm. During the oxidative transformation, diffusion leads to necking between the NCs, resulting in a porous NC network. The crystal structure before and after conversion was determined via X-ray diffraction (XRD), and indexed to the bixbyite V_2O_3 and monoclinic VO_2 structures, respectively (Figure 4.2c). A decrease in XRD peak widths between bixbyite and monoclinic suggests

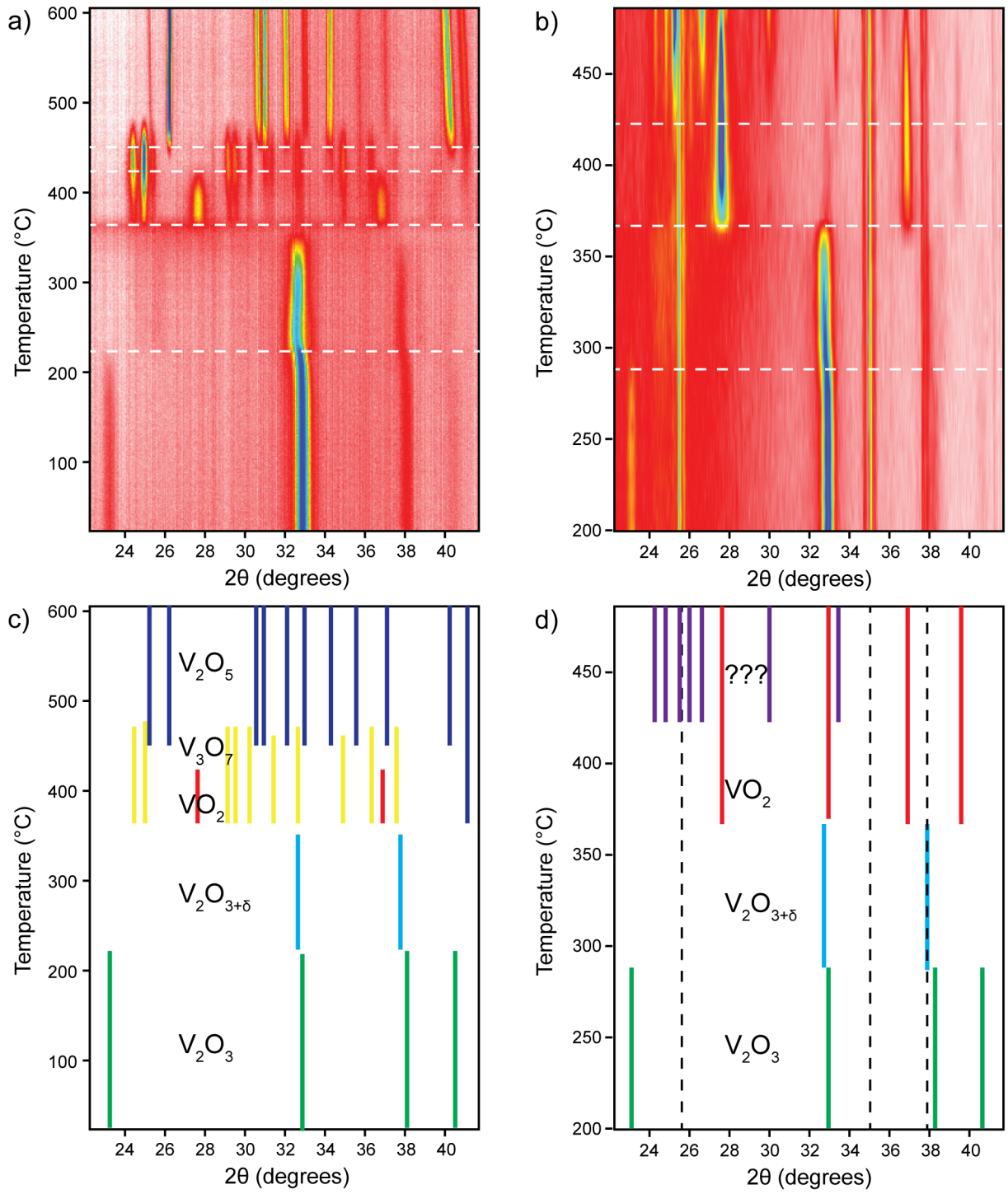

Figure 4.1: *In situ* XRD of bixbyite NCs heated in a) air and b) 250 ppm O_2 in N_2. Peak locations and phase identification from a) and b) are marked in c) and d), respectively, indicating location of XRD peaks indexed to bixbyite V_2O_3 (green), the unknown oxidized phase discussed in chapter x (blue), rutile VO_2 (red), V_3O_7 (yellow) and V_2O_5 (dark blue). An additional unknown phase, or mixture of unknown phases, is marked in purple. Black dotted lines mark peaks from *in situ* gas chamber.

that a small degree of coarsening occurs upon conversion. The resulting VO_2 NCs are thermochromic, exhibiting diminished IR transmittance at elevated temperature (Figure 4.2d), indicative of the phase transformation from monoclinic to rutile phase and the associated MIT. This IR blocking behavior in bulk rutile VO_2 is ascribed to the presence of conduction electrons and in nanostructures, the IR optical signature has been described as a damped localized surface plasmon resonance of those electrons.[64]

4.3.3 Electrochemically-Induced Optical Changes in VO_2

To investigate the response of our VO_2 NCs to electrochemical gating *in situ*, variable temperature spectroelectrochemistry was performed. In an inert atmosphere glove box maintained at < 1 ppm O_2, VO_2 films on ITO-coated glass were submerged in an electrolyte consisting of 0.1 M bis-trifluoromethanesulfonimidate (TFSI) salt in propylene carbonate. In our home-built apparatus, VO_2 acted as the working electrode while platinum and Ag/Ag^+ were used as counter and reference electrodes, respectively. Temperature was controlled using a Peltier thermoelectric element with a center hole to allow a continuous optical path through the VO_2 film, enabling collection of Vis-NIR transmission spectra *in situ* using a fiber-coupled spectrometer (Figure C.1). Irreversible optical changes were observed when lithium containing electrolyte was used, likely due to the intercalation of Li^+ ions in the VO_2 lattice resulting in an irreversible phase transformation (Figure C.2), consistent with the results of Kahn *et al.* on thin films.[145] When lithium was replaced with a bulky counter-ion, specifically tetrabutylammonium (TBA), intercalation was inhibited and reversible optical modulation was observed.

Upon application of a reducing bias (-1.5 V vs NHE) at room temperature, a strong decrease in NIR transmittance was observed, indicative of induced metallic character (Figure 4.3a). This spectroscopic observation is in agreement with the previous report of metallization induced IR darkening in ionic liquid gated epitaxial VO_2 films.[146] Our results demonstrate that optoelectronic modulation is possible in NCs even without ionic liquids, which are known to deliver the highest local fields. Continued application of this same bias, however, eventually leads to a reversal of the IR darkening (Figure 4.3b). This unexpected result suggests that the NC film is transitioning from a metallic state back to an insulating state. Voltage-induced IR bleaching was also observed upon reduction of the rutile phase at 100°C, but at a much faster rate (Figure C.3). This difference in rate may be due to faster kinetics of oxygen diffusion at high temperature or, as recently proposed in a study by Singh *et al.*, increased electrochemical reactivity in the rutile phase as compared to the monoclinic phase.[147]

Darkening and bleaching were found to be reversible upon the application of an oxidizing potential (Figure C.4 and C.5). Interestingly, we found that electrochemical modulation of IR transmittance was possible even in an oxygen-rich environment, albeit with lower coloration efficiency than in an inert environment (Figure C.6). In earlier reports, the conductivity of thin VO_2 films could not be modulated by ionic liquid gating in the presence of oxygen,[135] demonstrating once again the enhancement in the efficacy of electrochemical modulation using NC morphology. After removing electrochemical bias, darkened films exposed to air were observed to slowly return to an optical state characteristic of the original monoclinic structure while films in argon remained unchanged. In fact, as long as the film was not ex-

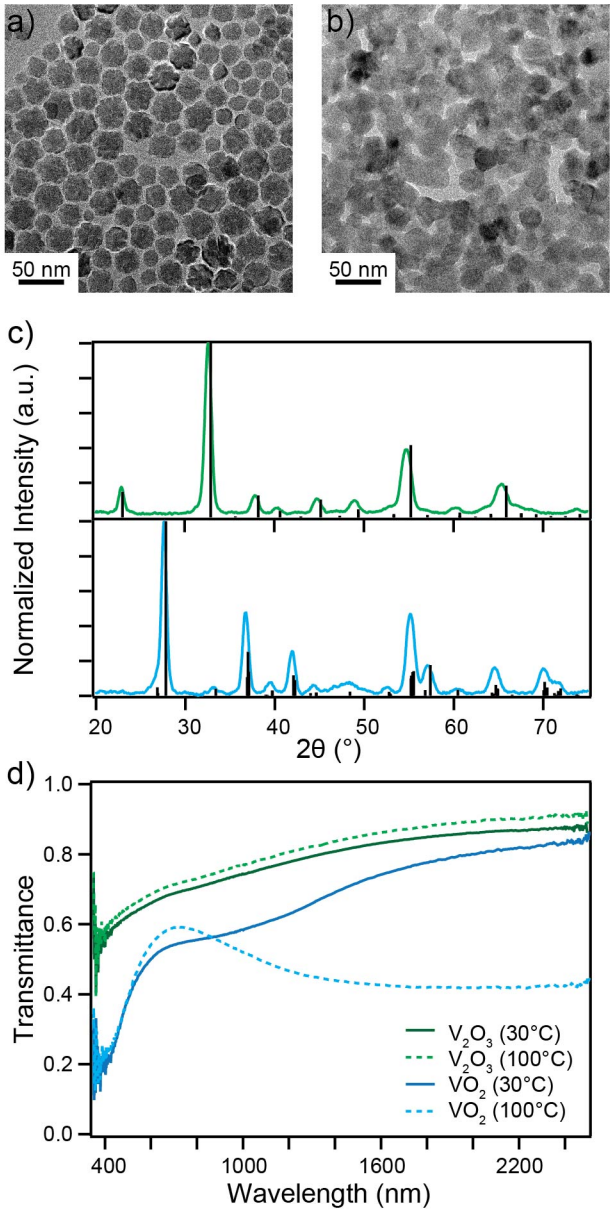

Figure 4.2: Characterization of V_2O_3 NCs and converted VO_2 NCs. TEM images of a) colloidal V_2O_3 NCs and b) VO_2 NCs generated via thermal annealing. c) XRD pattern of bixbyite V_2O_3 NCs (green/top) and monoclinic VO_2 NCs (bottom/blue). Reference XRD patterns [ICSD collection code 260212 and 15889] are shown in each plot. d) Transmittance spectra of NC thin films demonstrating minimal change for V_2O_3 and dramatic NIR modulation for VO_2 as a function of temperature.

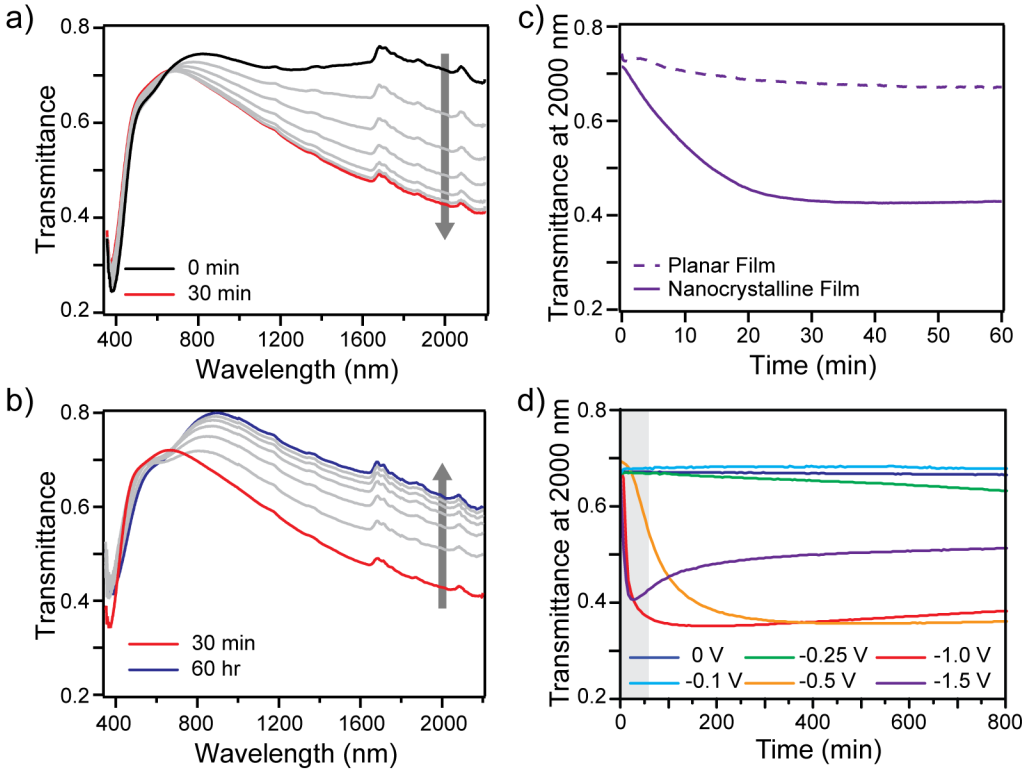

Figure 4.3: Spectroelectrochemistry of VO_2 NC films on ITO-coated glass in 0.1 M TBA-TFSI electrolyte. a) Darkening of NIR transmittance generated by applying -1.5V vs NHE with scans taken every 5 minutes for 30 minutes. b) Bleaching of NIR transmittance after applying -1.5V vs NHE starting at 30 minutes, with scans taken every 10 hours for 60 hours. c) Comparison of the NIR modulation kinetics at -1.5V vs NHE between a non-porous planar film of VO_2 (dashed) and a highly porous film of VO_2 NCs (solid line). d) The effect of applied potential on the transmittance of 2000 nm light as a function of time.

posed to oxygen, we could remove and rinse the electrode with no effect to the optical state, supporting the notion that the material is transformed under applied potential, not merely gated electrostatically. Planar VO_2 films, which we produced via the thermal condensation of vanadium oxalate clusters (Figure C.7),[148] showed very little change in IR transmittance upon the application of a reducing bias (Figure 4.3c and C.8), thereby highlighting the importance of nanostructuring, or exposure of certain crystal facets to the electrolyte interface, to enable this type of electrochemical control.

4.3.4 Spectroscopic Characterization of VO_2 in Different Optical States

Although the initial NIR darkening of our VO_2 NC films upon reduction was anticipated based on the thin film literature, the subsequent bleaching was not. To understand the structural changes occurring with progressive reduction, we performed Raman and X-ray absorption spectroscopy on NC films in various optical states, including the initial monoclinic, thermally darkened (rutile), electrochemically darkening, and partly or fully electrochemically bleached states. Films were prepared on doped silicon for use across a range of analytical techniques. As the kinetics of darkening and subsequent bleaching in the IR are sensitive to applied bias, as shown in Figure 4.3d, these states were accessed using different time-potential-temperature trajectories to avoid ambiguity and ensure that a complete set of samples in different optical states was obtained for analysis (details of their preparation are in Appendix C).

As the VO_2 NC films are thin and sensitive to air once electrochemically reduced, we utilized characterization techniques that required only a small amount of material and could be performed without exposure to air. Raman spectroscopy is one such technique and is commonly used for characterizing the structure of VO_2. At low temperature, peaks indicative of the monoclinic (M1) phase are apparent as shown in Figure 4.4a. As the film is heated, the VO_2 transforms to the more symmetric rutile phase and these peaks decrease in intensity and eventually disappear, consistent with previous Raman studies on VO_2 nanostructures.[149–151] To characterize the electrochemically darkening and further electrochemically reduced bleached states, films were first reduced then transferred air-free to the Raman spectrometer. The darkening state contains peaks that index to the monoclinic phase. This is in agreement with Jeong and co-workers finding that V-V dimerization, an identifying feature of the monoclinic phase, is maintained upon electrochemical metallization and is also consistent with recent Raman studies on ionic liquid gated VO_2 thin films.[136,147,152] On the other hand, the bleached state has no obvious Raman peaks, besides those which index to the underlying silicon substrate. This absence of peaks, however, is not sufficient evidence to assign the state to rutile phase. Instead, it merely suggests that the symmetry of the structure is increased and it is distinct from the monoclinic state.

X-ray absorption spectroscopy at the vanadium K-edge was used to further characterize the nature of the states accessed by electrochemical reduction. A progressive shift in absorption edge, indicative of a reduction in vanadium oxidation state, was observed in the near-edge region of the spectra (Figure 4.4b), implying that oxygen vacancy formation accompanies optical modulation throughout both the darkening and bleaching processes. The

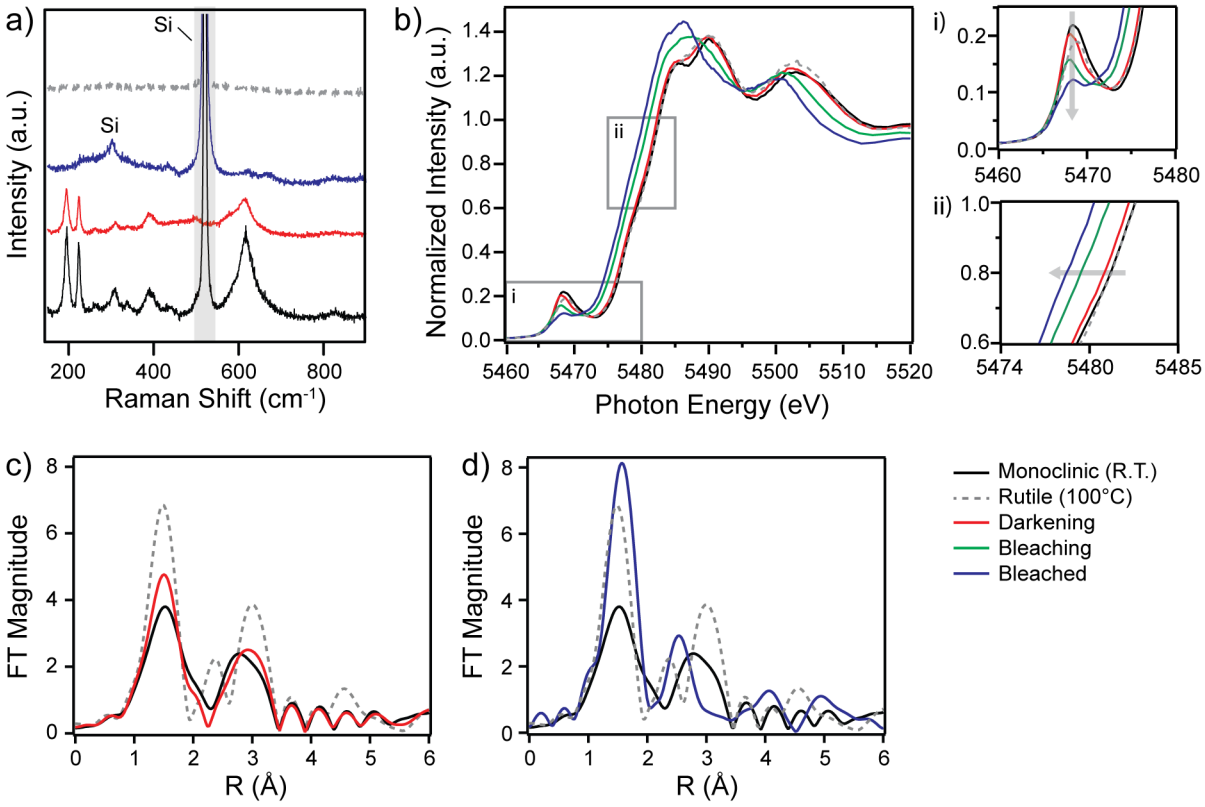

Figure 4.4: Characterization of monoclinic, rutile, darkening, bleaching, and bleached states by a) Raman spectroscopy and b) X-ray absorption near edge spectroscopy of the V K-edge, with zoomed in views of the i) pre-edge feature and ii) absorption edge. Fourier transformation of the k^3 weighted EXAFS of the c) darkening state and d) bleached state with monoclinic and rutile shown in each for comparison.

pre-edge feature at approximately 5470 eV was also observed to decrease in intensity with increasing reduction. This suppression of the V1s to V3d transition suggests an increase in octahedral symmetry, state mixing, and state filling occur during the reduction process.[153,154]

Although the Raman spectroscopy results identify the darkening state as monoclinic phase, the absence of Raman peaks in the bleached state requires that another technique be used to shed light on its structure. Therefore, extended X-ray absorption fine structure (EXAFS) was utilized to determine the local structure surrounding vanadium in the reduced NC films. As expected, the darkening and monoclinic patterns are nearly identical, confirming that the darkening state is indeed monoclinic phase even as it becomes metallic through electrochemical reduction (Figure 4.4c). However, the EXAFS pattern of the fully bleached state is very different from both the monoclinic and rutile phases, leading to the conclusion that further electrochemical reduction past the metallized monoclinic phase induces a phase transformation, as shown in Figure 4.4d.

Through a combination of temperature control and electrochemical bias, we were able to control the optical properties of a VO_2 NC film reversibly through four distinct transformations, as shown schematically in Figure 4.5. As previously hypothesized by Jeong *et al.*, darkening in the IR, indicative of metallization, is likely caused by the formation of oxygen vacancies. However, as reduction proceeds, bleaching in the IR is apparent. We propose that this optical change is due to a transformation to a different phase of vanadium oxide, triggered by instabilities in the monoclinic structure as oxygen vacancy concentration increases. This oxygen deficient phase, with an average oxidation state of approximately +3.4 as determined by absorption edge position,[154] was shown by Raman to have enhanced symmetry relative to the monoclinic phase. Furthermore, its high transmittance in the IR suggests that the material is an insulator. After analyzing many vanadium oxide structures, V_3O_5 was identified as a likely candidate for this oxygen deficient phase as it produced a good match to the fully bleached EXAFS data (Figure C.9) and is known to be insulating below ~150°C.[155]

In summary, we have demonstrated the ability to electrochemically modulate the IR transmittance of VO_2 NC films, prepared by controlled oxidation of V_2O_3 colloidal NCs, in a TBA-TFSI electrolyte. Initial application of a reducing bias leads to oxygen vacancy formation and diminished IR transmittance, as anticipated based on previous ionic liquid gating experiments performed on epitaxial VO_2 films. However, further reduction of our NC films was found to result in bleaching in the IR, leading to a never before seen transition to an oxygen deficient state. This progressive optical switching is likely facilitated by the nanocrystalline nature of the films, which may alter thermodynamics so that higher oxygen vacancy concentrations are accessible or enhance diffusion kinetics so that this behavior is apparent on experimentally realizable timescales. Strain due to gating induced volume expansion may

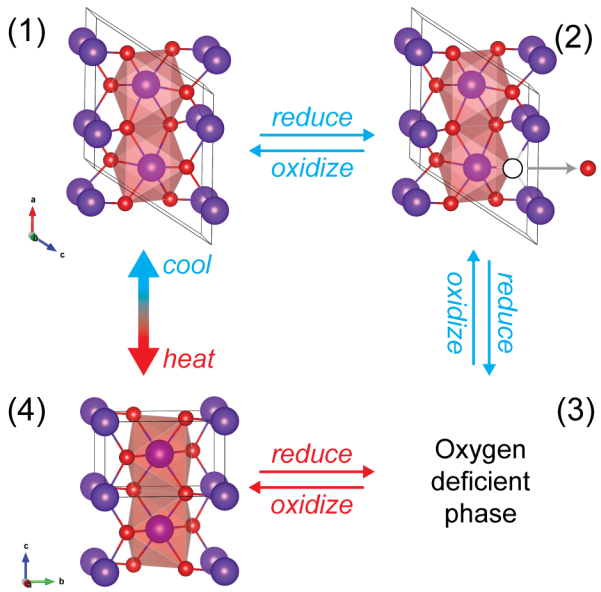

Figure 4.5: Schematic illustrating the pathways to 4 distinct states of VO_2 NC films: (1) The low-temperature, IR-transmitting monoclinic state, (2) an oxygen deficient, IR-blocking monoclinic state, (3) an IR-transmitting, oxygen deficient phase distinct from the monoclinic and rutile phases, and (4) the high-temperature, IR-blocking rutile state. These states can be accessed via heating/cooling and electrochemical reduction/oxidation, denoted by arrows in the diagram.

also be better accommodated by the NC morphology as compared to epitaxial thin films. The discovery of this new electrochemically-induced phase transition is promising for smart window applications if the kinetics can be further enhanced. This is especially true given the higher visible transmittance of the electrochemically bleached state as compared to the thermally accessible monoclinic phase, the low transmittance of which has been a major roadblock in the commercialization of VO_2-based thermochromic window coatings.[156]

4.5.1 Acknowledgments

The authors would like to acknowledge Jinghua Guo for helpful discussions. This work was supported by a U.S. Department of Energy (DOE) ARPA-E grant (A.B., C.J.D.), a DOE Early Career grant to D.J.M. (G.L.), and by the Welch Foundation (grant no. F-1848), X-ray absorption spectroscopy was performed at beamline 10.3.2 of the Advanced Light Source, which is supported by the Director, Office of Science, Office of Basic Energy Sciences, of the U.S. Department of Energy under Contract No. DE-AC02-05CH11231. A.B. and C.J.D were partially supported by National Science Foundation Graduate Research Fellowships under Grant No. DGE 1106400.

In this dissertation, the interesting phase behavior of vanadium oxide nanocrystals was presented and discussed. Influenced by both thermodynamic and kinetic factors, these nanocrystals demonstrate enhanced stability relative to bulk materials as well as faster kinetics of oxygen interstitial and vacancy diffusion owing to high surface area and small particle size. In Chapter 2, the colloidal synthesis of the newly-discovered, bixbyite polymorph of V_2O_3 was presented, including discussion of synthetic parameters, reaction mechanism, and formation mechanism. The stability of bixbyite nanocrystals was evaluated in both air and inert atmospheres, with phase transformations observed in each. The latter irreversible transformation to corundum phase in inert gas at temperatures above 700°C confirms the metastable nature of the polymorph, while concurrent particle coarsening suggests that bixbyite may be stabilized in nanocrystal form due to surface energy effects. In Chapter 3, the stability of bixbyite nanocrystals in air was explored, with structural changes occurring upon heating. Rietveld refinement of XRD data and supporting DFT calculations suggest that this is due to oxygen interstitial formation in the 16c Wyckoff positions of the bixbyite cell. The kinetics of oxidation were explored with *in situ* XRD at different temperatures and an Arrhenius relationship was observed. The rate limited step of the process was reasoned to be oxygen diffusion which was also supported by DFT. The reversibility of the oxidation process and resulting phase transformation were discussed and explained by the dependence of oxygen interstitial formation energy on temperature and oxygen partial pressure. Further oxidation at low oxygen partial pressure led to the stabilization of the monoclinic VO_2 phase, which is studied for its well-known MIT. In Chapter 4, optical changes upon electrochemical reduction of nanocrystalline VO_2 were observed *in situ* via variable-temperature spectroelectrochemistry. A decrease, then increase, of IR transmittance was observed with progressive reduction and the electrochemically darkened and bleached states were further characterized with Raman and X-ray absorption spectroscopies. The darkened state was found to be a oxygen-deficient, metallic form of monoclinic phase, while the bleached state could not be assigned to monoclinic or rutile phase.

Although this dissertation serves as a important starting point in the study of the bixbyite phase of V_2O_3 and electrochemically-induced transformations in nanocrystalline VO_2, there

is still work to be done to understand these unique materials and transformations. Therefore, avenues of future work will be discussed in the following sections. As only a few instances of its formation have been reported, there is still much to be learned about bixbyite V_2O_3, including its electronic and magnetic properties as discussed in Section 5.2. Determination of its thermodynamic properties will aid in the understanding of phase stability of the polymorph and thus is proposed in Section 5.3. Also suggested is doping as a means of enhancing the stability of the phase, which will contribute to both fundamental knowledge of phase stability in bixbyite and make high temperature application possible. Future work related to nanocrystalline VO_2 and its use in thermochromic window applications is also discussed in Section 5.4, while characterization techniques which may aid in the identification of the unknown phases encountered in this work are discussed in Section 5.5.

5.2.1 Electronic Properties

Although much progress has been made in understanding the new bixbyite phase of V_2O_3 in the last few years, there is still work to be done in determining the basic properties of the material. For example, multiple sources agree that the material is a semiconductor, however the exact band gap is still unknown. With DFT, Wessel *et al.* used a GGA functional to compute a direct band gap of 0.8 eV while Sarmadian *et al.*, using the more accurate HSE06 hybrid functional, computed an indirect band gap of 1.61 eV and an optical band gap of 1.98 eV.[87,99] Our DFT model, used in Chapter 3 to investigate oxygen interstitial defects in bixbyite, yielded a band gap of $\approx$0.5 eV. These values vary widely, an expected consequence of differing exchange correlation functionals and calculation parameters, and therefore experimental results are required to determine the true band gap of the material. In Chapter 2, we reported an experimental optical band gap of 1.29 eV, although this analysis was complicated by the gradual onset of absorption in the optical spectrum and corresponding Tauc plot (Figure A.9). Unfortunately, this is the only experimental value reported as of now, and thus it is impossible to know if this is representative of bulk bixbyite or if it is influenced in some way by size or nonstoichiometry. The closest bulk material for comparison is a vanadium oxide nitride with a bixbyite crystal structure, which was shown to have a band gap of 0.83 eV through an Arrhenius fit to temperature dependent conductivity data.[87] Unfortunately, extracting band gap from temperature dependent conductivity measurements of NC films is highly nontrivial. This is due to the fact that conduction in NC films occurs through a hopping mechanism, which also has an Arrhenius dependence. Because both carrier concentration, due to the band gap, and mobility, due to hopping, increase exponentially with temperature, the resulting conductivity data is influenced by both and it is very difficult to deconvolute the two.

Although band gap can not be determined easily, there are still opportunities to further the understanding of the electronic structure of bixbyite V_2O_3 with our NCs. It has been proposed and shown computationally that bixbyite V_2O_3 may support p-type doping. This is typically difficult in oxides due to the oxygen 2p character of the valence band maximum,

which tends to lie deep below the vacuum level resulting in large ionization potentials.[157] High-throughput DFT calculations of bixbyite oxides indicate that V_2O_3 may possess p-type dopability due to the proximity of its branch point energy to the valence band.[158] Additional computational work found magnesium to be a shallow acceptor in bixbyite V_2O_3 with low formation energy, and thus a promising candidate for p-type doping.[99] Preliminary work on doping bixbyite NCs with magnesium is ongoing. Once this is achieved, Hall measurements can be performed to determine the carrier type, confirming whether this type of dopant imparts p-type conductivity in bixbyite V_2O_3.

5.2.2 Magnetic Properties

In addition to electronic properties, little is known about the magnetic properties of bixbyite. In 2011, Weber *et al.* reported strong field dependence of the magnetic ordering transition at 50 K, which supports the existence of canted antiferromagnetic ordering or spin-glass like behavior.[29] Theoretical calculations, by ourselves and others, also show a slight preference for antiferromagnetic ordering over ferromagnetic ordering at 0 K.[87] Considering the magnetic properties associated with the other polymorphs of V_2O_3 and the already published report of spin-glass-like behavior at low temperature in the bixbyite phase, we anticipate that magnetic characterization of bixbyite NCs will yield interesting results. Furthermore, varying oxygen stoichiometry may also influence magnetic transitions the material, as observed previously in corundum and monoclinic V_2O_{3+x}.[25]

5.3.1 Thermodynamic Analysis of Nanocrystalline V_2O_3

In chapter 2, we hypothesized that bixbyite is an example of a size stabilized polymorph, where surface energy affects Gibbs free energy to the extent that the normally unstable bixbyite phase is thermodynamically favored over the stable corundum phase. However, there is more work to be done in order to prove that this truly is a thermodynamic, rather than kinetic, effect. The following equation describing the energetics of the bixbyite to corundum transformation as a function of nanocrystal size is adapted from the analysis of anatase titania by Zhang and Banfield:

$$\triangle G = \triangle_f G(T, corundum) - \triangle_f G(T, bixbyite) + (2t+3)\frac{M}{r}\left(\frac{\gamma_C}{\rho_C} - \frac{\gamma_B}{\rho_B}\right) \tag{5.1}$$

If bixbyite is truly a size stabilized polymorph in that it is thermodynamically favored below some critical size, ΔG must be positive for values of r less than the critical size. At the very least, since $\triangle_f G(T, corundum) - \triangle_f G(T, bixbyite)$ is negative, $\frac{C}{C} - \frac{B}{B}$ must be positive, or $\frac{C}{C} > \frac{B}{B}$. This analysis requires a knowledge of the Gibbs free energies and surface energies of bixbyite and corundum phase V_2O_3. While the latter has been reported previously,[159] the former has not, thus in order to proceed the Gibbs free energy and surface energy of bixbyite must be determined.

Thermodynamic properties like enthalpy, entropy, and surface energy can be measured using calorimetric methods which measure heat change during a reaction or transformation.[160] A technique known as solution drop calorimetry is typically used for the experimental determination of enthalpy and surface energy, in which a small pellet of solid material is dropped into molten oxide solvent.[161] The resulting heat released from the dissolution process is then measured, from which the enthalpy of formation can be extracted. Repeating this for several nanoparticle sizes, the enthalpy of formation can be plotted as a function of surface area. If surface energy is constant, the resulting slope is then equal to surface energy, as shown previously in Figure 1.4. In reality, surface energy may not scale linearly with surface area and will also be influenced by surface hydration, ligand binding, particle aggregation, and the presence of defects. Therefore, the use of solution drop calorimetry to determine surface energy in bixbyite V_2O_3 is a possible avenue of future work, but will likely be challenging owing to the difficulty of controlling particle size and the presence of ligands and oxygen defects.

Surface energy can also be determined computationally by DFT. Using a slab model, in which the crystal is periodic in two dimensions but not a third, the following equation can be used to estimate surface energy:

$$\gamma = \frac{1}{A}\left[E_{\mathsf{slab}} - nE_{\mathsf{bulk}}\right] \tag{5.2}$$

Where E_{slab} is the total energy of the slab terminated at the surface of interest, E_{bulk} is the total bulk energy per formula unit, n is the number of formula units in the slab, and A is the surface area of the top and bottom slab surfaces.[162] Because the pseudospherical bixbyite nanocrystals have many surface terminations, this will need to be repeated for several crystal facets then averaged to estimate a single surface energy, similar to what was done with known values of surface energy for different facets in rutile and anatase phase in Zhang and Banfield's analysis.[36] In reality, however, surface energy is also influenced by the ligands bound to the surface of the nanocrystals, which is dependent on binding geometry and surface coverage, and thus is far beyond the scope of this work and our group's DFT expertise. Nevertheless, the initial estimation of surface energy without the influence of ligands is an important first step in determining whether surface energy of bixbyite is true smaller than the surface energy of corundum phase- a result that is expected due to surface density, but as of yet, not confirmed.

5.3.2 Doping to Improve Phase Stability of Bixbyite V_2O_3

Although bixbyite V_2O_3 has already been shown to possess enhanced stability in nanocrystal form, it does eventually transform to corundum phase when heated above at least 700°C. Therefore, another avenue of future work involves enhancing the stability of the bixbyite phase, thus allowing for the utilization of bixbyite at high temperature without fear of transformation. In addition to nanoscaling, doping is another common method of stabilizing metastable phases.[163] The incorporation of dopants can introduce strain in the lattice, caused by differences in cation size or the formation of charge compensating defects, which may result in a different atomic configuration becoming energetically favorable. This lattice strain can be thought of as an additional contribution to the enthalpy of mixing term in the calculation

of Gibbs free energy. The most famous example of dopant stabilization is yttria-stabilized zirconia.[164] The addition of yttrium, a trivalent cation, in zirconia is compensated by the formation of oxygen vacancies. These vacancies stabilize the tetragonal phase, desired for its low thermal conductivity, over the bulk stable monoclinic phase.

In the case of bixbyite, initial doping experiments with aluminum, indium, chromium, and cerium all enhance the stability of the bixbyite phase over corundum, requiring higher temperatures or longer annealing times in order for transformation to proceed. Figure 5.1 shows *in situ* XRD of undoped and 2% Ce-doped sample heated to 900°C, showing quick transformation in the former case and no transformation in the latter. This demonstrates the validity of this approach to enhancing stability, although the underlying mechanism is not yet understood as the oxidation state and location of the Ce dopant is so far uncharacterized in this sample. Future work in this regard must focus on understanding how dopant species, dopant location within the lattice, and dopant location within the nanocrystal (i.e. surface or uniformly doped) collaborate to enhance stability of the bixbyite polymorph. Again, these experiments can be supported by DFT to gain an understanding of how the introduction of dopants influences energetic differences, and thus identify promising dopant candidates.

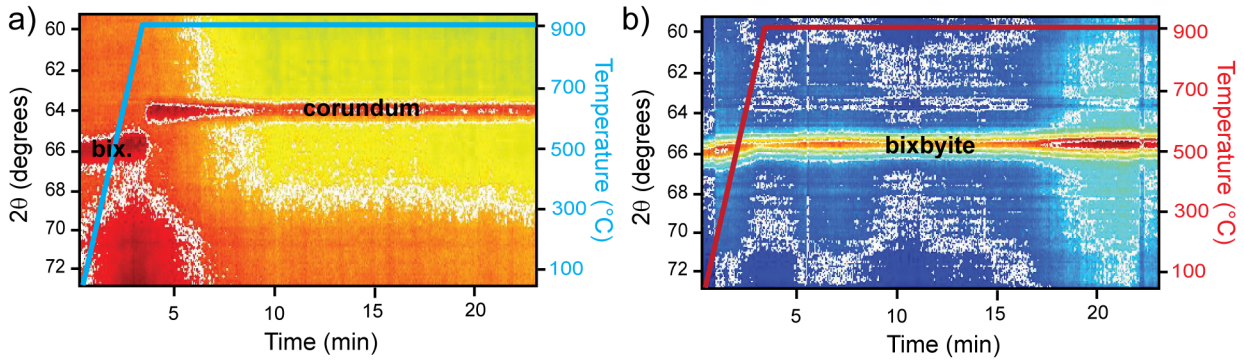

Figure 5.1: *In situ* XRD scans of a) undoped bixbyite and b) bixbyite doped with 2% Ce heated to 900°C. A transformation to corundum phase is apparent in the undoped sample while the bixbyite phase persists in the doped sample.

5.4.1 Nanocomposite Formation

In order to utilize VO_2 for thermochromic window applications, two major concerns must first be addressed.[156] First, the phase transformation temperature must be lowered. Strategies to lower this MIT transition are well established, and include the introduction of dopants (*e.g.*, W or Mg) and the application of strain.[13–15] The second concern is the low transmittance of visible light, yielding windows that appear yellow or brown in color. Visible transmittance can be improved by decreasing film thickness, but this has the effect of decreasing the modulation of IR light between low and high temperature states. Indeed, simultaneously maximization of visible transmittance and IR modulation has proven challenging, and is the subject of much research in the field of VO_2 thermochromism.[15,138,165]

One proposed solution to this problem involves the formation of VO_2 nanocomposites, consisting of VO_2 embedded in a high dielectric matrix.[138] Nanocomposites can be prepared from colloidal nanocrystals, as demonstrated previously by the Milliron group for the formation of dual-band electrochromic composites via the infilling of porous assemblies of nanocrystals or the formation of metal oxide cluster coatings on nanocrystals in solution before film deposition.[166,142] Unfortunately, VO_2 cannot yet be prepared colloidally. Rather, films of bixbyite V_2O_3 NCs must be annealed under low oxygen partial pressures to transform to nanocrystalline VO_2 as described in Chapter 4 and thus, the route to nanocomposites must allow for this oxidation process to occur.

One strategy to form VO_2 nanocomposites from V_2O_3 NCs involves infilling the pores of an already converted VO_2 NC film with a metal oxide precursor solution, followed by annealing to form metal oxide. Initial attempts utilized sol gel as an infilling solution, however the resulting sols were found to be too large to penetrate the NC film pores. Instead a metal precursor solution which crystallizes by means of combustion chemistry was used as an infilling solution.[167] Optimization of solution concentration and spin conditions yielded infilled nanocomposites which, unfortunately, did not possess improved optical properties when compared to pristine NC films. As pore sizes in the densely packed NC film are small, the problem may be that the volume fraction of VO_2 is too large. Therefore, future work will involve templating the VO_2 NCs in order to introduce larger pores for infilling, thus increasing the volume fraction of matrix material in the composite.

5.4.2 Size Control and Effect on MIT

In order to determine the parameters under which V_2O_3 is converted to VO_2, oxygen partial pressure, annealing time, and temperature were varied and the resulting NCs were characterized to determine particle morphology and phase. In the course of this investigation, annealing temperature was found to affect the resulting VO_2 crystallite size, with higher temperatures yielding larger particles. This is demonstrated by the scanning electron microscope images of films annealed at different temperatures in 250 ppm O_2 in N_2 in Figure 5.2. *In situ* XRD performed in a 2θ range containing the most intense peaks of V_2O_3 (at 33°) and VO_2 (at 27.5°) also supports this observation. Narrower VO_2 peak widths, corresponding to larger crystallite sizes, are observed with increasing annealing temperature. Another apparent trend is that as temperature increases, the time required for VO_2 to form decreases, likely due to enhanced kinetics of oxygen diffusion. Furthermore, VO_2 peak width does not appear to decrease any further with increasing time, suggesting that particle size is fairly constant after conversion. In order to quantify the effect of temperature and time on crystallite size, however, a full Scherrer analysis of peak width must be performed.

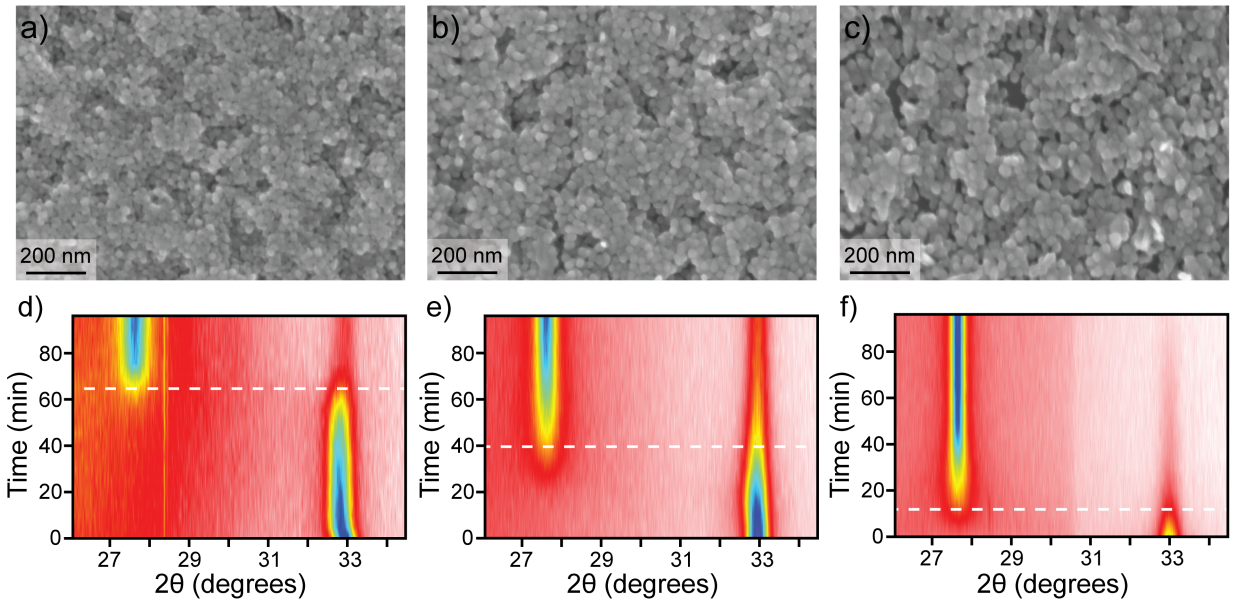

Figure 5.2: SEM images of VO_2 nanocrystalline films prepared from bixbyite NCs annealed at a) 350 °C, b) 375°C, and c) 387°C for 1 hour in an atmosphere of 250 ppm O_2 in N_2. *In situ* XRD of the bixbyite V_2O_3 to monoclinic VO_2 transition for films held at a) 350 °C, b) 375°C, and c) 387°C in same atmosphere. White dotted lines mark transformation time.

Initial characterization of MIT temperature was performed via *in situ* Vis-NIR spectroscopy. Transmittance scans were taken every 5-10°C while heating and cooling the films, as shown for a sample annealed at 362°C in Figure 5.3a. A plot of transmittance at 2000 nm as a function of temperature for the same sample is shown in Figure 5.3b, which could then be fit to a modified Fermi function to determine transition temperature. This was repeated for samples annealed at temperatures between 356°C and 400°C and transition temperature was plotted as a function of annealing temperature (Figure 5.3c). A slight depression in transformation temperature at lower annealing temperatures is apparent, while hysteresis width remains fairly constant. It is unclear whether this depression is a result of smaller crystallite sizes at low annealing temperature or if varying concentrations of oxygen defects also play a role. Therefore, future work in this area will require characterization of oxidation state within the nanocrystal, which can be garnered from V K-edge position, as in Figure 4.4b.

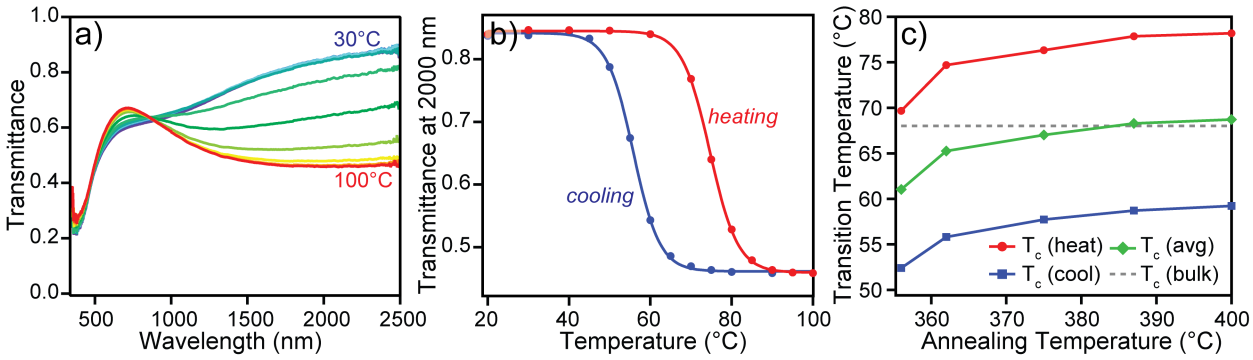

Figure 5.3: Optical changes through thermochromic transition in VO_2. a) Transmittance curves at different temperatures for NC film annealed at 362°C in 250 ppm O_2 in N_2. b) Plot of transmittance value at 2000 nm as a function of temperature during heating and cooling of NC films annealed at 362°C in 250 ppm O_2 in N_2, with fit to modified Fermi function. c) Transition temperature during heating and cooling (along with average of the two) for NC films annealed at different temperatures in 250 ppm O_2 in N_2. Dashed gray line denotes transition temperature in bulk VO_2.

Throughout this investigation of vanadium oxide nanocrystals, several unidentified phases have been observed. In chapter 2, unknown or amorphous phases were obtained by varying the ratio of oleic acid and oleylamine in the reaction. In chapter 3, the incorporation of oxygen interstitials eventually resulted in a transformation to an unknown, oxidized phase of vanadium oxide. Finally, in Chapter 4, a transformation to an unknown phase upon the electrochemical reduction of VO_2 was reported, likely due to instabilities in the lattice caused by oxygen vacancy formation. In the latter case, EXAFS analysis yields a decent fit to V_3O_5, although additional characterization of the phase is ongoing. This abundance of unknown phases is unsurprising given the structural complexity of vanadium oxides and the fact that the material is nanosized, which may alter thermodynamics to the extent that unstable or never before seen phases are stabilized. Indeed, although very few instances of colloidal vanadium oxide nanocrystals exist, those that do possess unknown or unexpected phases.[143]

All unknown phases encountered in this work have been compared to known compounds and phases of vanadium oxide, particularly the compounds with stoichiometry between that of V_2O_3 and VO_2, namely the Magnéli phases V_3O_5, V_4O_7, V_5O_9, V_6O_{11}, V_7O_{13}, V_8O_{15}, and the different polymorphs therein, as well as the other known polymorphs of V_2O_3 (monoclinic, corundum) and VO_2 (M1, M2, A, B, R, T). Given bixbyite's similarity to the fluorite structure, we have also investigated fluorite and derivative pyrochlore and weberite structures. Unfortunately, none of these have yielded fits to the unknown phases. It may be possible to utilize unit cell finding programs to narrow down a crystal lattice, but this is complicated by the fact that the materials are nanosized, resulting in broadened X-ray diffraction peaks and a higher degree of structural disorder compared to the bulk. Moving

forward, the identification of these phases will require the use of specialized techniques, such as convergent beam electron diffraction to identify symmetry operations within the crystal structure, neutron diffraction for corroborating oxygen ion position, and additional V K-edge EXAFS to determine local order surrounding each vanadium atom.

[1] H. A. Wriedt, "The O-V (Oxygen-Vanadium) system," *Bull. Alloy Phase Diagr.*, vol. 10, pp. 271–277, June 1989.

[2] F. J. Morin, "Oxides Which Show a Metal-to-Insulator Transition at the Neel Temperature," *Phys. Rev. Lett.*, vol. 3, pp. 34–36, July 1959.

[3] T. Driscoll, H.-T. Kim, B.-G. Chae, M. D. Ventra, and D. N. Basov, "Phase-transition driven memristive system," *Appl. Phys. Lett.*, vol. 95, p. 043503, July 2009.

[4] R. Xie, C. T. Bui, B. Varghese, Q. Zhang, C. H. Sow, B. Li, and J. T. L. Thong, "An Electrically Tuned Solid-State Thermal Memory Based on Metal–Insulator Transition of Single-Crystalline VO_2 Nanobeams," *Adv. Funct. Mater.*, vol. 21, pp. 1602–1607, May 2011.

[5] E. Strelcov, Y. Lilach, and A. Kolmakov, "Gas Sensor Based on Metal-Insulator Transition in VO_2 Nanowire Thermistor," *Nano Lett.*, vol. 9, pp. 2322–2326, June 2009.

[6] Y. Gao, H. Luo, Z. Zhang, L. Kang, Z. Chen, J. Du, M. Kanehira, and C. Cao, "Nanoceramic VO_2 thermochromic smart glass: A review on progress in solution processing," *Nano Energy*, vol. 1, pp. 221–246, Mar. 2012.

[7] M. E. A. Warwick and R. Binions, "Advances in thermochromic vanadium dioxide films," *J. Mater. Chem. A*, vol. 2, pp. 3275–3292, Feb. 2014.

[8] C. N. Berglund and H. J. Guggenheim, "Electronic Properties of VO_2 near the Semiconductor-Metal Transition," *Phys. Rev.*, vol. 185, pp. 1022–1033, Sept. 1969.

[9] J. B. Goodenough, "The two components of the crystallographic transition in VO_2," *J. Solid State Chem.*, vol. 3, pp. 490–500, Nov. 1971.

[10] R. M. Wentzcovitch, W. W. Schulz, and P. B. Allen, "VO_2: Peierls or Mott-Hubbard? A view from band theory," *Phys. Rev. Lett.*, vol. 72, pp. 3389–3392, May 1994.

[11] T. M. Rice, H. Launois, and J. P. Pouget, "Comment on "VO_2: Peierls or Mott-Hubbard? A View from Band Theory"," *Phys. Rev. Lett.*, vol. 73, pp. 3042–3042, Nov. 1994.

[12] Z. Tao, T.-R. T. Han, S. D. Mahanti, P. M. Duxbury, F. Yuan, C.-Y. Ruan, K. Wang, and J. Wu, "Decoupling of Structural and Electronic Phase Transitions in VO_2," *Phys. Rev. Lett.*, vol. 109, p. 166406, Oct. 2012.

[13] J. Cao, Y. Gu, W. Fan, L. Q. Chen, D. F. Ogletree, K. Chen, N. Tamura, M. Kunz, C. Barrett, J. Seidel, and J. Wu, "Extended Mapping and Exploration of the Vanadium Dioxide Stress-Temperature Phase Diagram," *Nano Lett.*, vol. 10, pp. 2667–2673, July 2010.

[14] C. B. Greenberg, "Undoped and doped VO_2 films grown from $VO(OC_3H_7)_3$," *Thin Solid Films*, vol. 110, pp. 73–82, Dec. 1983.

[15] N. Mlyuka, G. Niklasson, and C. G. Granqvist, "Mg doping of thermochromic VO_2 films enhances the optical transmittance and decreases the metal-insulator transition temperature," *Appl. Phys. Lett.*, vol. 95, pp. 171909–171909–3, Oct. 2009.

[16] J. P. Pouget and H. Launois, "Metal-Insulator Phase Transition in VO_2," *J. Phys. Colleques*, vol. 37, pp. 49–57, Oct. 1976.

[17] S. Zhang, J. Y. Chou, and L. J. Lauhon, "Direct Correlation of Structural Domain Formation with the Metal Insulator Transition in a VO_2 Nanobeam," *Nano Lett.*, vol. 9, pp. 4527–4532, Dec. 2009.

[18] J. H. Park, J. M. Coy, T. S. Kasirga, C. Huang, Z. Fei, S. Hunter, and D. H. Cobden, "Measurement of a solid-state triple point at the metal-insulator transition in VO_2," *Nature*, vol. 500, pp. 431–434, Aug. 2013.

[19] F. Théobald, "Étude hydrothermale du système VO_2-$VO_{2,5}$-H_2O," *J. Less Common Met.*, vol. 53, pp. 55–71, May 1977.

[20] M. Zhang and J. R. Dahn, "Electrochemical Lithium Intercalation in VO_2(B) in Aqueous Electrolytes," *J. Electrochem. Soc.*, vol. 143, pp. 2730–2735, Sept. 1996.

[21] J. M. Atkin, S. Berweger, E. K. Chavez, M. B. Raschke, J. Cao, W. Fan, and J. Wu, "Strain and temperature dependence of the insulating phases of VO_2 near the metal-insulator transition," *Phys. Rev. B*, vol. 85, p. 020101, Jan. 2012.

[22] P. D. Dernier and M. Marezio, "Crystal Structure of the Low-Temperature Antiferromagnetic Phase of V_2O_3," *Phys. Rev. B*, vol. 2, pp. 3771–3776, Nov. 1970.

[23] R. M. Moon, "Antiferromagnetism in V_2O_3," *Phys. Rev. Lett.*, vol. 25, pp. 527–529, Aug. 1970.

[24] D. B. McWhan, A. Menth, J. P. Remeika, W. F. Brinkman, and T. M. Rice, "Metal-Insulator Transitions in Pure and Doped V_2O_3," *Phys. Rev. B*, vol. 7, pp. 1920–1931, Mar. 1973.

[25] Y. Ueda, K. Kosuge, and S. Kachi, "Phase diagram and some physical properties of V_2O_{3+x} ($0 < x < 0.080$)," *J. Solid State Chem.*, vol. 31, pp. 171–188, Feb. 1980.

[26] S. A. Shivashankar and J. M. Honig, "Metal-antiferromagnetic-insulator transition in V_2O_3 alloys," *Phys. Rev. B*, vol. 28, pp. 5695–5701, Nov. 1983.

[27] D. B. McWhan and J. P. Remeika, "Metal-Insulator Transition in $(V_{1-x}Cr_x)_2O_3$," *Phys. Rev. B*, vol. 2, pp. 3734–3750, Nov. 1970.

[28] N. F. Mott and Z. Zinamon, "The metal-nonmetal transition," *Rep. Prog. Phys.*, vol. 33, p. 881, Sept. 1970.

[29] D. Weber, A. Stork, S. Nakhal, C. Wessel, C. Reimann, W. Hermes, A. Müller, T. Ressler, R. Pöttgen, T. Bredow, R. Dronskowski, and M. Lerch, "Bixbyite-Type V_2O_3 —A Metastable Polymorph of Vanadium Sesquioxide," *Inorg. Chem.*, vol. 50, pp. 6762–6766, July 2011.

[30] P. Ehrenfest, "Phase changes in the ordinary and extended sense classified according to the corresponding singularities of the thermodynamic potential," *Proc. Acad. Sci. Amsterdam*, vol. 36, pp. 153–157, 1993.

[31] J. M. McHale, A. Auroux, A. J. Perrotta, and A. Navrotsky, "Surface Energies and Thermodynamic Phase Stability in Nanocrystalline Aluminas," *Science*, vol. 277, pp. 788–791, Aug. 1997.

[32] D. P. Dinega and M. G. Bawendi, "A Solution-Phase Chemical Approach to a New Crystal Structure of Cobalt," *Angew. Chem. Int. Ed.*, vol. 38, pp. 1788–1791, June 1999.

[33] S. S. Farvid, N. Dave, and P. V. Radovanovic, "Phase-Controlled Synthesis of Colloidal In_2O_3 Nanocrystals via Size-Structure Correlation," *Chem. Mater.*, vol. 22, pp. 9–11, Jan. 2010.

[34] R. B. Soriano, I. U. Arachchige, C. D. Malliakas, J. Wu, and M. G. Kanatzidis, "Nanoscale Stabilization of New Phases in the PbTe–Sb_2Te_3 System: $Pb_mSb_{2n}Te_{m+3n}$ Nanocrystals," *J. Am. Chem. Soc.*, vol. 135, pp. 768–774, Jan. 2013.

[35] M. R. Ranade, A. Navrotsky, H. Z. Zhang, J. F. Banfield, S. H. Elder, A. Zaban, P. H. Borse, S. K. Kulkarni, G. S. Doran, and H. J. Whitfield, "Energetics of nanocrystalline TiO_2," *Proc. Natl. Acad. Sci. U.S.A.*, vol. 99, pp. 6476–6481, Apr. 2002.

[36] H. Zhang and J. F. Banfield, "Thermodynamic Analysis of Phase Stability of Nanocrystalline Titania," *J. Mater. Chem.*, vol. 8, pp. 2073–2076, Jan. 1998.

[37] A. A. Gribb and J. F. Banfield, "Particle size effects on transformation kinetics and phase stability in nanocrystalline TiO_2," *Am. Mineral.*, vol. 82, pp. 717–728, Aug. 1997.

[38] O. Warschkow, M. Asta, N. Erdman, K. R. Poeppelmeier, D. E. Ellis, and L. D. Marks, "TiO_2-rich reconstructions of $SrTiO_3$(0 0 1): a theoretical study of structural patterns," *Surf. Sci.*, vol. 573, pp. 446–456, Dec. 2004.

[39] J. Y. Suh, R. Lopez, L. C. Feldman, and R. F. Haglund, "Semiconductor to metal phase transition in the nucleation and growth of VO_2 nanoparticles and thin films," *J. Appl. Phys.*, vol. 96, pp. 1209–1213, July 2004.

[40] R. Lopez, L. C. Feldman, and R. F. Haglund, "Size-Dependent Optical Properties of VO_2 Nanoparticle Arrays," *Phys. Rev. Lett.*, vol. 93, p. 177403, Oct. 2004.

[41] R. Lopez, L. A. Boatner, T. E. Haynes, L. C. Feldman, and R. F. H. Jr, "Synthesis and Characterization of Size-Controlled Vanadium Dioxide Nanocrystals in a Fused Silica Matrix," *J. Appl. Phys.*, vol. 92, pp. 4031–4036, Oct. 2002.

[42] J.-H. Son, J. Wei, D. Cobden, G. Cao, and Y. Xia, "Hydrothermal Synthesis of Monoclinic VO_2 Micro- and Nanocrystals in One Step and Their Use in Fabricating Inverse Opals," *Chem. Mater.*, vol. 22, pp. 3043–3050, May 2010.

[43] T.-D. Nguyen and T.-O. Do, "Solvo-Hydrothermal Approach for the Shape-Selective Synthesis of Vanadium Oxide Nanocrystals and Their Characterization," *Langmuir*, vol. 25, pp. 5322–5332, May 2009.

[44] Y. Yin and A. P. Alivisatos, "Colloidal nanocrystal synthesis and the organic–inorganic interface," *Nature*, vol. 437, pp. 664–670, Sept. 2005.

[45] V. K. LaMer and R. H. Dinegar, "Theory, Production and Mechanism of Formation of Monodispersed Hydrosols," *J. Am. Chem. Soc.*, vol. 72, pp. 4847–4854, Nov. 1950.

[46] D. A. Porter and K. E. Easterling, *Phase Transformations in Metals and Alloys*. Chapman & Hall, 2 ed., July 1992.

[47] I. Yamaguchi, T. Manabe, T. Tsuchiya, T. Nakajima, M. Sohma, and T. Kumagai, "Preparation and Characterization of Epitaxial VO_2 Films on Sapphire Using Postepitaxial Topotaxy Route via Epitaxial V_2O_3 Films," *Jpn. J. Appl. Phys.*, vol. 47, pp. 1022–1027, Feb. 2008.

[48] A. Bergerud, R. Buonsanti, J. L. Jordan-Sweet, and D. J. Milliron, "Synthesis and Phase Stability of Metastable Bixbyite V_2O_3 Colloidal Nanocrystals," *Chem. Mater.*, vol. 25, pp. 3172–3179, Aug. 2013.

[49] S. S. Farvid, N. Dave, T. Wang, and P. V. Radovanovic, "Dopant-Induced Manipulation of the Growth and Structural Metastability of Colloidal Indium Oxide Nanocrystals," *J. Phys. Chem. C*, vol. 113, pp. 15928–15933, Sept. 2009.

[50] I. T. Sines, R. Misra, P. Schiffer, and R. E. Schaak, "Colloidal Synthesis of Non-Equilibrium Wurtzite-Type MnSe," *Angew. Chem. Int. Ed.*, vol. 49, pp. 4638–4640, June 2010.

[51] C.-C. Chen, A. B. Herhold, C. S. Johnson, and A. P. Alivisatos, "Size Dependence of Structural Metastability in Semiconductor Nanocrystals," *Science*, vol. 276, pp. 398–401, Apr. 1997.

[52] T. Blasco and J. M. L. Nieto, "Oxidative Dyhydrogenation of Short Chain Alkanes on Supported Vanadium Oxide Catalysts," *Appl. Catal. A: Gen.*, vol. 157, pp. 117–142, Sept. 1997.

[53] I. E. Wachs and B. M. Weckhuysen, "Structure and Reactivity of Surface Vanadium Oxide Species on Oxide Supports," *Appl. Catal. A: Gen.*, vol. 157, pp. 67–90, Sept. 1997.

[54] A. Talledo and C. G. Granqvist, "Electrochromic Vanadium–Pentoxide–Based Films: Structural, Electrochemical, and Optical Properties," *J. Appl. Phys.*, vol. 77, pp. 4655–4666, May 1995.

[55] N. F. Mott, *Metal-insulator transitions*. London; New York: Taylor & Francis, 1990.

[56] Y. Wang and G. Cao, "Synthesis and Enhanced Intercalation Properties of Nanostructured Vanadium Oxides," *Chem. Mater.*, vol. 18, pp. 2787–2804, June 2006.

[57] M. R. J. Scherer, L. Li, P. M. S. Cunha, O. A. Scherman, and U. Steiner, "Enhanced Electrochromism in Gyroid-Structured Vanadium Pentoxide," *Adv. Mater.*, vol. 24, pp. 1217–1221, Mar. 2012.

[58] C. Hess, "Nanostructured Vanadium Oxide Model Catalysts for Selective Oxidation Reactions," *ChemPhysChem*, vol. 10, pp. 319–326, Feb. 2009.

[59] X.-F. Zhang, K.-X. Wang, X. Wei, and J.-S. Chen, "Carbon-Coated V_2O_5 Nanocrystals as High Performance Cathode Material for Lithium Ion Batteries," *Chem. Mater.*, vol. 23, pp. 5290–5292, Dec. 2011.

[60] J. M. Velazquez and S. Banerjee, "Catalytic Growth of Single-Crystalline V_2O_5 Nanowire Arrays," *Small*, vol. 5, pp. 1025–1029, May 2009.

[61] S. A. Corr, M. Grossman, Y. Shi, K. R. Heier, G. D. Stucky, and R. Seshadri, "VO_2(B) Nanorods: Solvothermal Preparation, Electrical Properties, and Conversion to Rutile VO_2 and V_2O_3," *J. Mater. Chem.*, vol. 19, pp. 4362–4367, June 2009.

[62] S. Zhang, B. Shang, J. Yang, W. Yan, S. Wei, and Y. Xie, "From VO_2 (B) to VO_2 (A) Nanobelts: First Hydrothermal Transformation, Spectroscopic Study and First Principles Calculation," *Phys. Chem. Chem. Phys.*, vol. 13, no. 35, p. 15873, 2011.

[63] J. M. Booth and P. S. Casey, "Production of VO_2 M1 and M2 Nanoparticles and Composites and the Influence of the Substrate on the Structural Phase Transition," *ACS Appl. Mater. Interfaces*, vol. 1, pp. 1899–1905, Sept. 2009.

[64] K. Appavoo, D. Y. Lei, Y. Sonnefraud, B. Wang, S. T. Pantelides, S. A. Maier, and R. F. Haglund, "Role of Defects in the Phase Transition of VO_2 Nanoparticles Probed by Plasmon Resonance Spectroscopy," *Nano Lett.*, vol. 12, pp. 780–786, Feb. 2012.

[65] L. Whittaker, C. Jaye, Z. Fu, D. A. Fischer, and S. Banerjee, "Depressed Phase Transition in Solution-Grown VO_2 Nanostructures," *J. Am. Chem. Soc.*, vol. 131, pp. 8884–8894, July 2009.

[66] S. Zhang, I. S. Kim, and L. J. Lauhon, "Stoichiometry Engineering of Monoclinic to Rutile Phase Transition in Suspended Single Crystalline Vanadium Dioxide Nanobeams," *Nano Lett.*, vol. 11, pp. 1443–1447, Apr. 2011.

[67] V. A. Blagojevic, J. P. Carlo, L. E. Brus, M. L. Steigerwald, Y. J. Uemura, S. J. L. Billinge, W. Zhou, P. W. Stephens, A. A. Aczel, and G. M. Luke, "Magnetic Phase Transition in V_2O_3 Nanocrystals," *Phys. Rev. B*, vol. 82, p. 094453, Sept. 2010.

[68] N. Pinna, M. Antonietti, and M. Niederberger, "A Novel Nonaqueous Route to V_2O_3 and Nb_2O_5 Nanocrystals," *Colloids Surf., A*, vol. 250, pp. 211–213, Dec. 2004.

[69] R. Buonsanti, V. Grillo, E. Carlino, C. Giannini, T. Kipp, R. Cingolani, and P. D. Cozzoli, "Nonhydrolytic Synthesis of High-Quality Anisotropically Shaped Brookite TiO_2 Nanocrystals," *J. Am. Chem. Soc.*, vol. 130, pp. 11223–11233, Aug. 2008.

[70] J. Zhang, Eerdemutu, C. Yang, J. Feng, X. Di, Z. Liu, and G. Xu, "Size- and Shape-Controlled Synthesis of Monodisperse Vanadium Dioxide Nanocrystals," *J. Nanosci. Nanotechnol.*, vol. 10, pp. 2092–2098, Mar. 2010.

[71] Y. Ishiwata, S. Suehiro, T. Kida, H. Ishii, Y. Tezuka, H. Oosato, E. Watanabe, D. Tsuya, Y. Inagaki, T. Kawae, M. Nantoh, and K. Ishibashi, "Spontaneous Uniaxial Strain and Disappearance of the Metal-Insulator Transition in Monodisperse V_2O_3 Nanocrystals," *Phys. Rev. B*, vol. 86, p. 035449, July 2012.

[72] Y. Xu, L. Zheng, C. Wu, F. Qi, and Y. Xie, "New-Phased Metastable V_2O_3 Porous Urchinlike Micronanostructures: Facile Synthesis and Application in Aqueous Lithium Ion Batteries," *Chem. Eur. J.*, vol. 17, pp. 384–391, Jan. 2011.

[73] A. Larson and R. Von Dreele, "General Structure Analysis System (GSAS)," 2000.

[74] B. H. Toby, "EXPGUI, a graphical user interface for GSAS," *J. Appl. Crystallogr.*, vol. 34, pp. 210–213, Apr. 2001.

[75] J. Xu, A. R. Wilson, A. R. Rathmell, J. Howe, M. Chi, and B. J. Wiley, "Synthesis and Catalytic Properties of Au–Pd Nanoflowers," *ACS Nano*, vol. 5, pp. 6119–6127, Aug. 2011.

[76] A. Narayanaswamy, H. Xu, N. Pradhan, and X. Peng, "Crystalline Nanoflowers with Different Chemical Compositions and Physical Properties Grown by Limited Ligand Protection," *Angew. Chem. Int. Ed.*, vol. 118, pp. 5487–5490, Aug. 2006.

[77] L. J. Bellamy, *The Infrared Spectra of Complex Molecules.* Bungay, Suffolk: Richard Clay and Company Ltd., 2nd ed., 1959.

[78] K. Nakamoto, *Infrared and Raman Spectra of Inorganic and Coordination Compounds, Applications in Coordination, Organometallic, and Bioinorganic Chemistry.* Hoboken, N.J: Wiley-Interscience, b ed., Jan. 2009.

[79] J. Selbin, "The Chemistry of Oxovanadium(IV)," *Chem. Rev.*, vol. 65, pp. 153–175, Apr. 1965.

[80] R. G. Garvey and R. O. Ragsdale, "Trans-axial ligation in coordination complexes of oxovanadium(IV)," *Inorg. Chim. Acta*, vol. 2, pp. 191–194, Mar. 1968.

[81] P. D. Dernier, "The crystal structure of V_2O_3 and $(V_{0.962}Cr_{0.0382})_2O_3$ near the metal-insulator transition," *J. Phys. Chem. Solids*, vol. 31, pp. 2569–2575, Nov. 1970.

[82] R. W. G. Wyckoff, *Crystal Structures: Inorganic Compounds RXn, RnMX2, RnMX3*, vol. 2. Interscience Publishers, 1964.

[83] S. Tsunekawa, K. Ishikawa, Z.-Q. Li, Y. Kawazoe, and A. Kasuya, "Origin of Anomalous Lattice Expansion in Oxide Nanoparticles," *Phys. Rev. Lett.*, vol. 85, pp. 3440–3443, Oct. 2000.

[84] G. Li, J. Boerio-Goates, B. F. Woodfield, and L. Li, "Evidence of linear lattice expansion and covalency enhancement in rutile TiO_2 nanocrystals," *Appl. Phys. Lett.*, vol. 85, pp. 2059–2061, Sept. 2004.

[85] H. R. Moon, J. J. Urban, and D. J. Milliron, "Size-Controlled Synthesis and Optical Properties of Monodisperse Colloidal Magnesium Oxide Nanocrystals," *Angew. Chem. Int. Ed.*, vol. 48, pp. 6278–6281, Aug. 2009.

[86] G. Li, L. Li, J. Boerio-Goates, and B. F. Woodfield, "High Purity Anatase TiO_2 Nanocrystals: Near Room-Temperature Synthesis, Grain Growth Kinetics, and Surface Hydration Chemistry," *J. Am. Chem. Soc.*, vol. 127, pp. 8659–8666, June 2005.

[87] C. Wessel, C. Reimann, A. Müller, D. Weber, M. Lerch, T. Ressler, T. Bredow, and R. Dronskowski, "Electronic structure and thermodynamics of V_2O_3 polymorphs," *J. Comput. Chem.*, vol. 33, pp. 2102–2107, Oct. 2012.

[88] A. Murali, A. Barve, V. J. Leppert, S. H. Risbud, I. M. Kennedy, and H. W. H. Lee, "Synthesis and Characterization of Indium Oxide Nanoparticles," *Nano Lett.*, vol. 1, pp. 287–289, June 2001.

[89] S. P. Shafi, R. J. Lundgren, L. M. D. Cranswick, and M. Bieringer, "Formation, structure and magnetism of the metastable defect fluorite phases $AVO_{3.5+x}$(A=In, Sc)," *J. Solid State Chem.*, vol. 180, pp. 3333–3340, Dec. 2007.

[90] J. A. Alonso, M. T. Casais, and M. J. Martinez-Lope, "Preparation and topotactical oxidation of $ScVO_3$ with bixbyte structure: a low-temperature route to stabilize the new defect fluorite $ScVO_{3.5}$ metastable phase," *Dalton Trans.*, pp. 1294–1297, Apr. 2004.

[91] N. V. Skorodumova, S. I. Simak, B. I. Lundqvist, I. A. Abrikosov, and B. Johansson, "Quantum Origin of the Oxygen Storage Capability of Ceria," *Phys. Rev. Lett.*, vol. 89, p. 166601, Sept. 2002.

[92] T. Ghoshal, P. G. Fleming, J. D. Holmes, and M. A. Morris, "The stability of "Ce_2O_3" nanodots in ambient conditions: a study using block copolymer templated structures," *J. Mater. Chem.*, vol. 22, pp. 22949–22957, Oct. 2012.

[93] J. A. Rodriguez, J. C. Hanson, J.-Y. Kim, G. Liu, A. Iglesias-Juez, and M. Fernández-García, "Properties of CeO_2 and $Ce_{1-x}Zr_xO_2$ Nanoparticles: X-ray Absorption Near-Edge Spectroscopy, Density Functional, and Time-Resolved X-ray Diffraction Studies," *J. Phys. Chem. B*, vol. 107, pp. 3535–3543, Apr. 2003.

[94] S. Deshpande, S. Patil, S. V. Kuchibhatla, and S. Seal, "Size dependency variation in lattice parameter and valency states in nanocrystalline cerium oxide," *Appl. Phys. Lett.*, vol. 87, p. 133113, Sept. 2005.

[95] D. J. Reidy, J. D. Holmes, and M. A. Morris, "The critical size mechanism for the anatase to rutile transformation in TiO_2 and doped-TiO_2," *J. Eur. Ceram. Soc.*, vol. 26, no. 9, pp. 1527–1534, 2006.

[96] Y. Hu, H. L. Tsai, and C. L. Huang, "Phase transformation of precipitated TiO_2 nanoparticles," *Mater. Sci. Eng. A.*, vol. 344, pp. 209–214, Mar. 2003.

[97] R. Buonsanti, E. Carlino, C. Giannini, D. Altamura, L. De Marco, R. Giannuzzi, M. Manca, G. Gigli, and P. D. Cozzoli, "Hyperbranched Anatase TiO_2 Nanocrystals: Nonaqueous Synthesis, Growth Mechanism, and Exploitation in Dye-Sensitized Solar Cells," *J. Am. Chem. Soc.*, vol. 133, pp. 19216–19239, Nov. 2011.

[98] A. Bergerud, S. M. Selbach, and D. J. Milliron, "Oxygen Incorporation and Release in Metastable Bixbyite V_2O_3 Nanocrystals," *ACS Nano*, vol. 10, pp. 6147–6155, May 2016.

[99] N. Sarmadian, R. Saniz, B. Partoens, and D. Lamoen, "*Ab initio* study of shallow acceptors in bixbyite V_2O_3," *J. Appl. Phys.*, vol. 117, p. 015703, Jan. 2015.

[100] K. Momma and F. Izumi, "*VESTA 3* for three-dimensional visualization of crystal, volumetric and morphology data," *J. Appl. Crystallogr.*, vol. 44, pp. 1272–1276, Dec. 2011.

[101] C. Reimann, D. Weber, M. Lerch, and T. Bredow, "Nonstoichiometry in Bixbyite-Type Vanadium Sesquioxide," *J. Phys. Chem. C*, vol. 117, pp. 20164–20170, Oct. 2013.

[102] H. Jeen, W. S. Choi, M. D. Biegalski, C. M. Folkman, I.-C. Tung, D. D. Fong, J. W. Freeland, D. Shin, H. Ohta, M. F. Chisholm, and H. N. Lee, "Reversible redox reactions in an epitaxially stabilized $SrCoO_x$ oxygen sponge," *Nat. Mater.*, vol. 12, pp. 1057–1063, Nov. 2013.

[103] M. Hervieu, A. Guesdon, J. Bourgeois, E. Elkaïm, M. Poienar, F. Damay, J. Rouquette, A. Maignan, and C. Martin, "Oxygen storage capacity and structural flexibility of $LuFe_2O_{4+x}$($0<=x<=0.5$)," *Nat. Mater.*, vol. 13, pp. 74–80, Jan. 2014.

[104] M. Sugiura, "Oxygen Storage Materials for Automotive Catalysts: Ceria-Zirconia Solid Solutions," *Catal. Surv. Asia*, vol. 7, pp. 77–87, Apr. 2003.

[105] G. Silversmit, D. Depla, H. Poelman, G. B. Marin, and R. De Gryse, "Determination of the V2p XPS binding energies for different vanadium oxidation states (V5+ to V0+)," *J. Electron Spectrosc.*, vol. 135, pp. 167–175, Apr. 2004.

[106] D. Wilson and M. A. Langell, "XPS analysis of oleylamine/oleic acid capped Fe_3O_4 nanoparticles as a function of temperature," *Appl. Surf. Sci.*, vol. 303, pp. 6–13, June 2014.

[107] P. Hohenberg and W. Kohn, "Inhomogeneous Electron Gas," *Phys. Rev.*, vol. 136, pp. B864–B871, Nov. 1964.

[108] W. Kohn and L. J. Sham, "Self-Consistent Equations Including Exchange and Correlation Effects," *Phys. Rev.*, vol. 140, pp. A1133–A1138, Nov. 1965.

[109] G. Kresse and J. Furthmüller, "Efficiency of *ab initio* total energy calculations for metals and semiconductors using a plane-wave basis set," *Comp. Mater. Sci.*, vol. 6, pp. 15–50, July 1996.

[110] G. Kresse and J. Hafner, "*Ab initio* molecular dynamics for liquid metals," *Phys. Rev. B*, vol. 47, pp. 558–561, Jan. 1993.

[111] G. Kresse and D. Joubert, "From ultrasoft pseudopotentials to the projector augmented-wave method," *Phys. Rev. B*, vol. 59, pp. 1758–1775, Jan. 1999.

[112] P. E. Blöchl, "Projector augmented-wave method," *Phys. Rev. B*, vol. 50, pp. 17953–17979, Dec. 1994.

[113] J. P. Perdew, A. Ruzsinszky, G. I. Csonka, O. A. Vydrov, G. E. Scuseria, L. A. Constantin, X. Zhou, and K. Burke, "Restoring the density-gradient expansion for exchange in solids and surfaces," *Phys. Rev. Lett.*, vol. 100, Apr. 2008. arXiv: 0711.0156.

[114] F. Birch, "Finite Elastic Strain of Cubic Crystals," *Phys. Rev.*, vol. 71, pp. 809–824, June 1947.

[115] G. Henkelman, B. P. Uberuaga, and H. Jónsson, "A climbing image nudged elastic band method for finding saddle points and minimum energy paths," *J. Chem. Phys.*, vol. 113, pp. 9901–9904, Dec. 2000.

[116] G. Henkelman and H. Jónsson, "Improved tangent estimate in the nudged elastic band method for finding minimum energy paths and saddle points," *J. Chem. Phys.*, vol. 113, pp. 9978–9985, Dec. 2000.

[117] P. S. Manning, J. D. Sirman, and J. A. Kilner, "Oxygen self-diffusion and surface exchange studies of oxide electrolytes having the fluorite structure," *Solid State Ionics*, vol. 93, pp. 125–132, Dec. 1996.

[118] P. Ágoston and K. Albe, "*Ab initio* modeling of diffusion in indium oxide," *Phys. Rev. B*, vol. 81, p. 195205, May 2010.

[119] A. Chroneos, R. V. Vovk, I. L. Goulatis, and L. I. Goulatis, "Oxygen transport in perovskite and related oxides: A brief review," *J. Alloy. Compd.*, vol. 494, pp. 190–195, Apr. 2010.

[120] C. Freysoldt, B. Grabowski, T. Hickel, J. Neugebauer, G. Kresse, A. Janotti, and C. G. Van de Walle, "First-principles calculations for point defects in solids," *Rev. Mod. Phys.*, vol. 86, pp. 253–305, Mar. 2014.

[121] L. Wang, T. Maxisch, and G. Ceder, "Oxidation energies of transition metal oxides within the GGA + U framework," *Phys. Rev. B*, vol. 73, p. 195107, May 2006.

[122] C. Abughayada, B. Dabrowski, S. Kolesnik, D. E. Brown, and O. Chmaissem, "Characterization of Oxygen Storage and Structural Properties of Oxygen-Loaded Hexagonal $RMnO_{3+}$ (R = Ho, Er, and Y)," *Chem. Mater.*, vol. 27, pp. 6259–6267, Sept. 2015.

[123] T. Grande, J. R. Tolchard, and S. M. Selbach, "Anisotropic Thermal and Chemical Expansion in Sr-Substituted $LaMnO_{3+}$: Implications for Chemical Strain Relaxation," *Chem. Mater.*, vol. 24, pp. 338–345, Jan. 2012.

[124] E. Mamontov, T. Egami, R. Brezny, M. Koranne, and S. Tyagi, "Lattice Defects and Oxygen Storage Capacity of Nanocrystalline Ceria and Ceria-Zirconia," *J. Phys. Chem. B*, vol. 104, pp. 11110–11116, Nov. 2000.

[125] S. Bishop, D. Marrocchelli, C. Chatzichristodoulou, N. Perry, M. Mogensen, H. Tuller, and E. Wachsman, "Chemical Expansion: Implications for Electrochemical Energy Storage and Conversion Devices," *Annu. Rev. Mater. Res.*, vol. 44, no. 1, pp. 205–239, 2014.

[126] R. D. Shannon, "Revised effective ionic radii and systematic studies of interatomic distances in halides and chalcogenides," *Acta Crystallogr. A*, vol. 32, pp. 751–767, Sept. 1976.

[127] A. A. Sokol, A. Walsh, and C. R. A. Catlow, "Oxygen interstitial structures in close-packed metal oxides," *Chem. Phys. Lett.*, vol. 492, pp. 44–48, May 2010.

[128] S. Lany and A. Zunger, "Dopability, Intrinsic Conductivity, and Nonstoichiometry of Transparent Conducting Oxides," *Phys. Rev. Lett.*, vol. 98, p. 045501, Jan. 2007.

[129] K. Appavoo, B. Wang, N. F. Brady, M. Seo, J. Nag, R. P. Prasankumar, D. J. Hilton, S. T. Pantelides, and R. F. Haglund, "Ultrafast Phase Transition via Catastrophic Phonon Collapse Driven by Plasmonic Hot-Electron Injection," *Nano Lett.*, vol. 14, pp. 1127–1133, Mar. 2014.

[130] G. Stefanovich, A. Pergament, and D. Stefanovich, "Electrical switching and Mott transition in VO_2," *J. Phys.: Condens. Matter*, vol. 12, no. 41, p. 8837, 2000.

[131] P. P. Boriskov, A. A. Velichko, A. L. Pergament, G. B. Stefanovich, and D. G. Stefanovich, "The effect of electric field on metal-insulator phase transition in vanadium dioxide," *Tech. Phys. Lett.*, vol. 28, pp. 406–408, May 2002.

[132] H.-T. Kim, B.-G. Chae, D.-H. Youn, S.-L. Maeng, G. Kim, K.-Y. Kang, and Y.-S. Lim, "Mechanism and observation of Mott transition in VO_2-based two- and three-terminal devices," *New J. Phys.*, vol. 6, no. 1, p. 52, 2004.

[133] G. Gopalakrishnan, D. Ruzmetov, and S. Ramanathan, "On the triggering mechanism for the metal–insulator transition in thin film VO_2 devices: electric field versus thermal effects," *J. Mater. Sci.*, vol. 44, pp. 5345–5353, Apr. 2009.

[134] M. Nakano, K. Shibuya, D. Okuyama, T. Hatano, S. Ono, M. Kawasaki, Y. Iwasa, and Y. Tokura, "Collective bulk carrier delocalization driven by electrostatic surface charge accumulation," *Nature*, vol. 487, pp. 459–462, July 2012.

[135] J. Jeong, N. Aetukuri, T. Graf, T. D. Schladt, M. G. Samant, and S. S. P. Parkin, "Suppression of Metal-Insulator Transition in VO_2 by Electric Field–Induced Oxygen Vacancy Formation," *Science*, vol. 339, pp. 1402–1405, Mar. 2013.

[136] J. Jeong, N. B. Aetukuri, D. Passarello, S. D. Conradson, M. G. Samant, and S. S. P. Parkin, "Giant reversible, facet-dependent, structural changes in a correlated-electron insulator induced by ionic liquid gating," *Proc. Natl. Acad. Sci. U.S.A.*, vol. 112, pp. 1013–1018, Jan. 2015.

[137] J. Karel, C. E. ViolBarbosa, J. Kiss, J. Jeong, N. Aetukuri, M. G. Samant, X. Kozina, E. Ikenaga, G. H. Fecher, C. Felser, and S. S. P. Parkin, "Distinct Electronic Structure of the Electrolyte Gate-Induced Conducting Phase in Vanadium Dioxide Revealed by High-Energy Photoelectron Spectroscopy," *ACS Nano*, vol. 8, pp. 5784–5789, June 2014.

[138] S.-Y. Li, G. A. Niklasson, and C. G. Granqvist, "Nanothermochromics: Calculations for VO_2 nanoparticles in dielectric hosts show much improved luminous transmittance and solar energy transmittance modulation," *J. Appl. Phys.*, vol. 108, p. 063525, Sept. 2010.

[139] R. Lopez, T. E. Haynes, L. A. Boatner, L. C. Feldman, and R. F. Haglund, "Size effects in the structural phase transition of VO_2 nanoparticles," *Phys. Rev. B*, vol. 65, p. 224113, June 2002.

[140] L. Kang, Y. Gao, H. Luo, Z. Chen, J. Du, and Z. Zhang, "Nanoporous Thermochromic VO_2 Films with Low Optical Constants, Enhanced Luminous Transmittance and Thermochromic Properties," *ACS Appl. Mater. Interfaces*, vol. 3, pp. 135–138, Feb. 2011.

[141] G. Garcia, R. Buonsanti, E. L. Runnerstrom, R. J. Mendelsberg, A. Llordes, A. Anders, T. J. Richardson, and D. J. Milliron, "Dynamically Modulating the Surface Plasmon Resonance of Doped Semiconductor Nanocrystals," *Nano Lett.*, vol. 11, pp. 4415–4420, Oct. 2011.

[142] A. Llordés, G. Garcia, J. Gazquez, and D. J. Milliron, "Tunable near-infrared and visible-light transmittance in nanocrystal-in-glass composites," *Nature*, vol. 500, pp. 323–326, Aug. 2013.

[143] T. Paik, S.-H. Hong, E. A. Gaulding, H. Caglayan, T. R. Gordon, N. Engheta, C. R. Kagan, and C. B. Murray, "Solution-Processed Phase-Change VO_2 Metamaterials from Colloidal Vanadium Oxide (VO_x) Nanocrystals," *ACS Nano*, vol. 8, pp. 797–806, Jan. 2014.

[144] M. A. Marcus, A. A. MacDowell, R. Celestre, A. Manceau, T. Miller, H. A. Padmore, and R. E. Sublett, "Beamline 10.3.2 at ALS: a hard X-ray microprobe for environmental and materials sciences," *J. Synchrotron Rad.*, vol. 11, pp. 239–247, May 2004.

[145] M. S. R. Khan, K. A. Khan, W. Estrada, and C. G. Granqvist, "Electrochromism and thermochromism of Li_xVO_2 thin films," *J. Appl. Phys.*, vol. 69, pp. 3231–3234, Mar. 1991.

[146] M. Nakano, K. Shibuya, N. Ogawa, T. Hatano, M. Kawasaki, Y. Iwasa, and Y. Tokura, "Infrared-sensitive electrochromic device based on VO_2," *Appl. Phys. Lett.*, vol. 103, p. 153503, Oct. 2013.

[147] S. Singh, T. A. Abtew, G. Horrocks, C. Kilcoyne, P. M. Marley, A. A. Stabile, S. Banerjee, P. Zhang, and G. Sambandamurthy, "Selective electrochemical reactivity of rutile VO_2 towards the suppression of metal-insulator transition," *Phys. Rev. B*, vol. 93, p. 125132, Mar. 2016.

[148] A. Llordes, A. T. Hammack, R. Buonsanti, R. Tangirala, S. Aloni, B. A. Helms, and D. J. Milliron, "Polyoxometalates and colloidal nanocrystals as building blocks for metal oxide nanocomposite films," *J. Mater. Chem.*, vol. 21, pp. 11631–11638, July 2011.

[149] A. C. Jones, S. Berweger, J. Wei, D. Cobden, and M. B. Raschke, "Nano-optical Investigations of the Metal-Insulator Phase Behavior of Individual VO_2 Microcrystals," *Nano Lett.*, vol. 10, pp. 1574–1581, May 2010.

[150] L. Whittaker, T.-L. Wu, A. Stabile, G. Sambandamurthy, and S. Banerjee, "Single-Nanowire Raman Microprobe Studies of Doping-, Temperature-, and Voltage-Induced Metal–Insulator Transitions of $W_xV_{1-x}O_2$ Nanowires," *ACS Nano*, vol. 5, pp. 8861–8867, Nov. 2011.

[151] H. Zhang, Q. Li, P. Shen, Q. Dong, B. Liu, R. Liu, T. Cui, and B. Liu, "The structural phase transition process of free-standing monoclinic vanadium dioxide micron-sized rods: temperature-dependent Raman study," *RSC Adv.*, vol. 5, pp. 83139–83143, Sept. 2015.

[152] S. Chen, X. j. Wang, L. Fan, G. Liao, Y. Chen, W. Chu, L. Song, J. Jiang, and C. Zou, "The Dynamic Phase Transition Modulation of Ion-Liquid Gating VO_2 Thin Film: Formation, Diffusion, and Recovery of Oxygen Vacancies," *Adv. Funct. Mater.*, pp. n/a–n/a, Mar. 2016.

[153] J.-L. Chen, C.-C. Chang, Y.-K. Ho, C. L. Chen, C.-C. Hsu, W.-L. Jang, D.-H. Wei, C.-L. Dong, C.-W. Pao, J.-F. Lee, J.-M. Chen, J. Guo, and M.-K. Wu, "Behind the color

switching in gasochromic VO_2," *Phys. Chem. Chem. Phys.*, vol. 17, pp. 3482–3489, Jan. 2015.

[154] J. Wong, F. W. Lytle, R. P. Messmer, and D. H. Maylotte, "K-edge absorption spectra of selected vanadium compounds," *Phys. Rev. B*, vol. 30, pp. 5596–5610, Nov. 1984.

[155] E. I. Terukov, F. A. Chudnovskii, W. Reichelt, H. Oppermann, W. Brückner, H.-P. Brückner, and W. Moldenhauer, "Investigation of the physical properties of V_3O_5 at phase transition with consideration of its range of homogeneity," *Phys. Stat. Sol. (A)*, vol. 37, pp. 541–546, Oct. 1976.

[156] S.-Y. Li, G. A. Niklasson, and C. G. Granqvist, "Thermochromic fenestration with VO_2-based materials: Three challenges and how they can be met," *Thin Solid Films*, vol. 520, pp. 3823–3828, Mar. 2012.

[157] N. Sarmadian, R. Saniz, B. Partoens, and D. Lamoen, "Easily doped p-type, low hole effective mass, transparent oxides," *Sci. Rep.*, vol. 6, p. 20446, Feb. 2016.

[158] N. Sarmadian, R. Saniz, B. Partoens, D. Lamoen, K. Volety, G. Huyberechts, and J. Paul, "High throughput first-principles calculations of bixbyite oxides for TCO applications," *Phys. Chem. Chem. Phys.*, vol. 16, no. 33, pp. 17724–17733, 2014.

[159] W. Haynes, "Standard Thermodynamic Properties of Chemical Substances," in *CRC Handbook of Chemistry and Physics*, pp. 4–42, CRC Press- Taylor & Francis, 96 ed., 2015.

[160] S. Stølen and T. Grande, "Experimental Thermodynamics," in *Chemical Thermodynamics of Materials*, pp. 303–335, John Wiley & Sons, Ltd, 2003.

[161] A. Navrotsky, "Nanoscale Effects on Thermodynamics and Phase Equilibria in Oxide Systems," *ChemPhysChem*, vol. 12, pp. 2207–2215, Aug. 2011.

[162] D. S. Sholl and J. A. Steckel, "DFT Calculations for Surfaces of Solids," in *Density Functional Theory: A Practical Introduction*, pp. 83–112, John Wiley & Sons, Inc., 2009.

[163] D. A. H. Hanaor and C. C. Sorrell, "Review of the anatase to rutile phase transformation," *J Mater Sci*, vol. 46, pp. 855–874, Dec. 2010.

[164] S. Shukla and S. Seal, "Mechanisms of room temperature metastable tetragonal phase stabilisation in zirconia," *Int. Mater. Rev.*, vol. 50, pp. 45–64, Feb. 2005.

[165] L. Zhao, L. Miao, C. Liu, C. Li, T. Asaka, Y. Kang, Y. Iwamoto, S. Tanemura, H. Gu, and H. Su, "Solution-Processed VO_2-SiO_2 Composite Films with Simultaneously Enhanced Luminous Transmittance, Solar Modulation Ability and Anti-Oxidation property," *Sci. Rep.*, vol. 4, Nov. 2014.

[166] J. Kim, G. K. Ong, Y. Wang, G. LeBlanc, T. E. Williams, T. M. Mattox, B. A. Helms, and D. J. Milliron, "Nanocomposite Architecture for Rapid, Spectrally-Selective Electrochromic Modulation of Solar Transmittance," *Nano Lett.*, vol. 15, pp. 5574–5579, Aug. 2015.

[167] M.-G. Kim, M. G. Kanatzidis, A. Facchetti, and T. J. Marks, "Low-temperature fabrication of high-performance metal oxide thin-film electronics via combustion processing," *Nat. Mater.*, vol. 10, pp. 382–388, May 2011.

[168] S. Y. Ezhov, V. I. Anisimov, D. I. Khomskii, and G. A. Sawatzky, "Orbital Occupation, Local Spin, and Exchange Interactions in V_2O_3," *Phys. Rev. Lett.*, vol. 83, pp. 4136–4139, Nov. 1999.

[169] I. Solovyev, N. Hamada, and K. Terakura, "t_{2g} versus all 3d localization in $LaMO_3$ perovskites (M=Ti-Cu): First-principles study," *Phys. Rev. B*, vol. 53, pp. 7158–7170, Mar. 1996.

[170] S. Åsbrink, "The crystal structure of and valency distribution in the low-temperature modification of V_3O_5. The decisive importance of a few very weak reflexions in a crystal-structure determination," *Acta. Cryst.*, vol. 36, pp. 1332–1339, June 1980.

[171] S. H. Hong and S. Åsbrink, "The structure of the high-temperature modification of V_3O_5 at 458 K," *Acta. Cryst.*, vol. 38, pp. 713–719, Mar. 1982.

[172] U. Schwingenschlögl and V. Eyert, "The vanadium Magnéli phases V_nO_{2n-1}," *Ann. Phys.*, vol. 13, pp. 475–510, Sept. 2004.

[173] M. Newville, "*IFEFFIT* : interactive XAFS analysis and *FEFF* fitting," *J. Synchrotron Rad.*, vol. 8, pp. 322–324, Mar. 2001.

[174] B. Ravel and M. Newville, "*ATHENA* , *ARTEMIS* , *HEPHAESTUS* : data analysis for X-ray absorption spectroscopy using *IFEFFIT*," *J. Synchrotron Rad.*, vol. 12, pp. 537–541, July 2005.

This appendix includes additional TEM images and size histograms of the bixbyite NCs, FTIR spectra used in the analysis of reaction mechanism, TEM images and XRD scans of NCs made under different reaction conditions, details on Rietveld Refinement, and UV-vis-NIR spectra used for the determination of band gap.

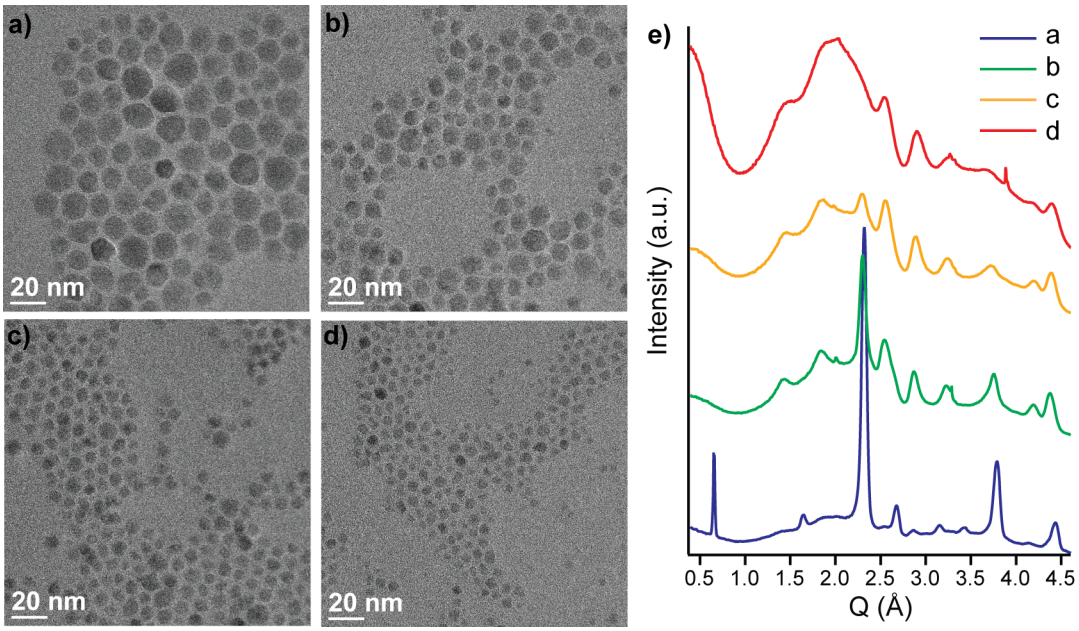

Figure A.1: Small nanocrystals separated from nanoflowers by size selective precipitation with average diameter a) 12.0 ± 3 nm, b) 8.0 ± 2 nm, c) 6.1 ± 1.2 nm, and d) 4.5 ± 1.0 nm. e) Corresponding XRD patterns of samples a-d show that smallest nanocrystals no longer possess bixbyite crystal structure.

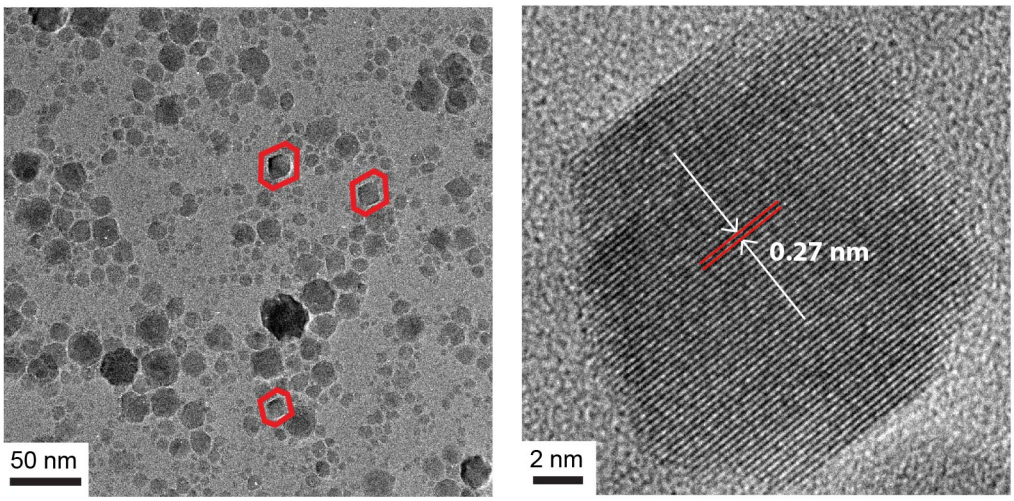

Figure A.2: Faceted nanocrystals form at elevated temperatures (370°C and above). Lattice spacing of 0.27 nm matches spacing between (222) planes in the bixbyite structure. XRD scan can be indexed to pure bixbyite phase.

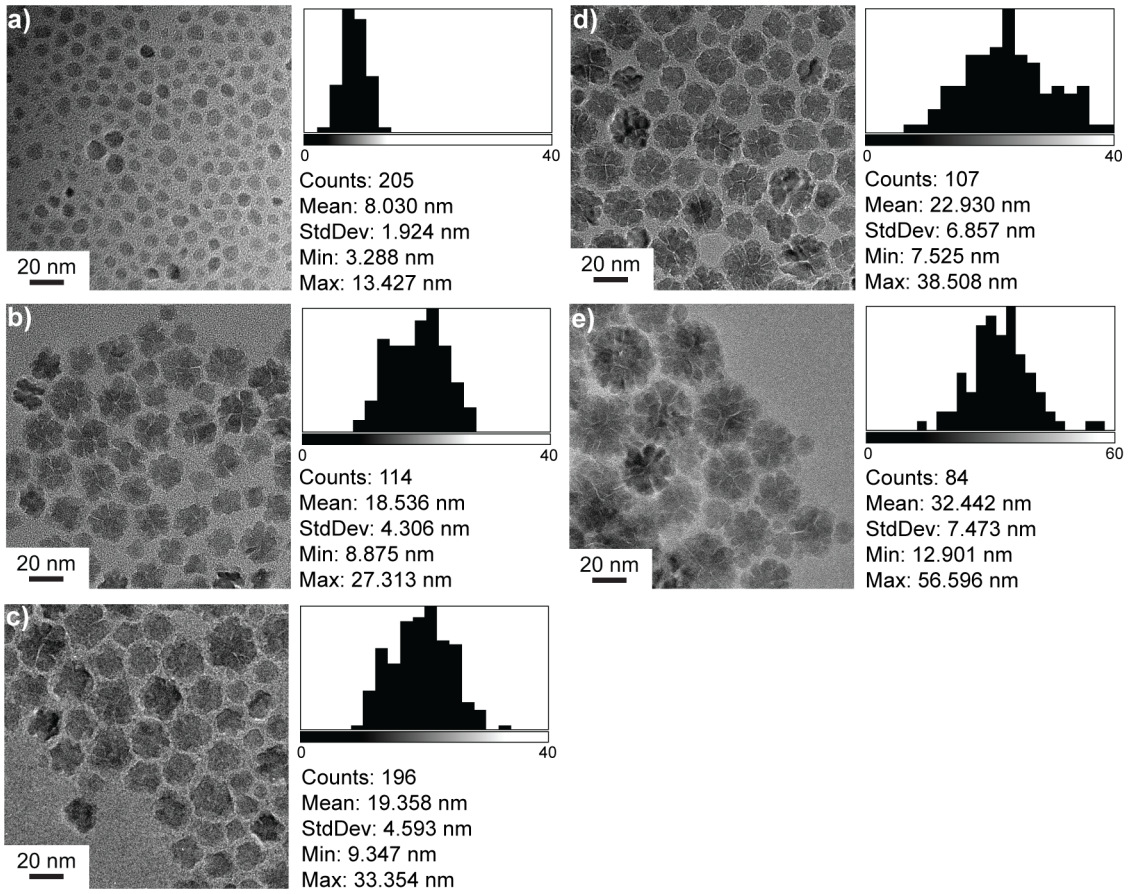

Figure A.3: Representative TEM images and histograms showing size distribution of nanocrystals synthesized at 340°C for a) 0 minutes with fast quench, b) 0 minutes with slow cooling, c) 1 hour, d) 4 hours, and e) 24 hours.

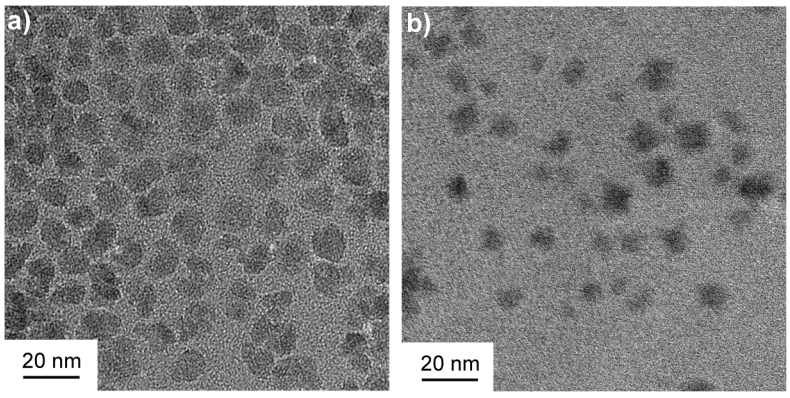

Figure A.4: TEM images of nanocrystal made with a) excess oleylamine (6 mmol oleylamine with 4 mmol oleic acid) and b) excess oleic acid (6 mmol oleic acid with 4 mmol oleylamine).

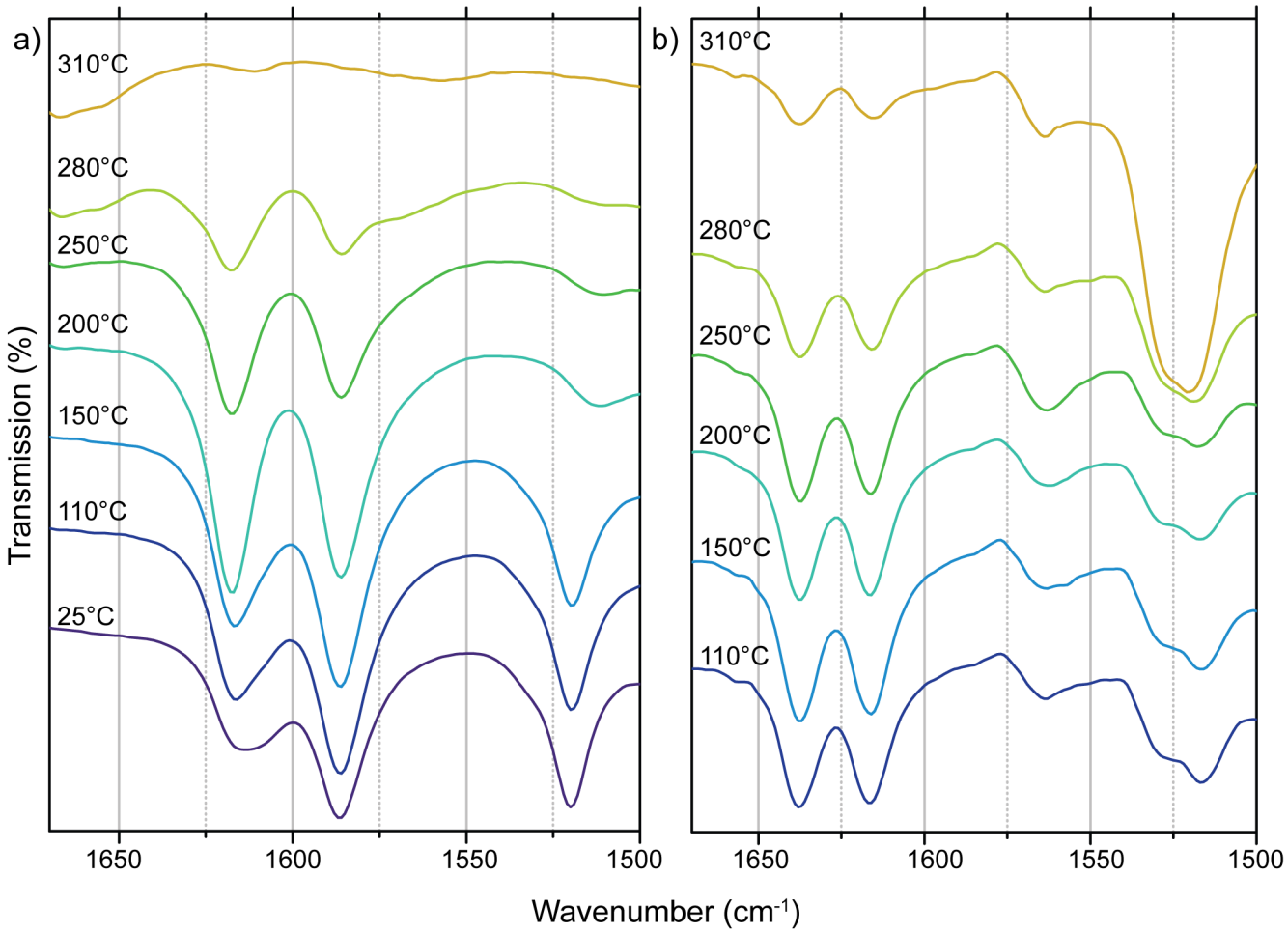

Figure A.5: FTIR spectra of reaction mixture collected at various temperatures during the heating of the reactants without the addition of a) oleic acid and b) oleylamine.

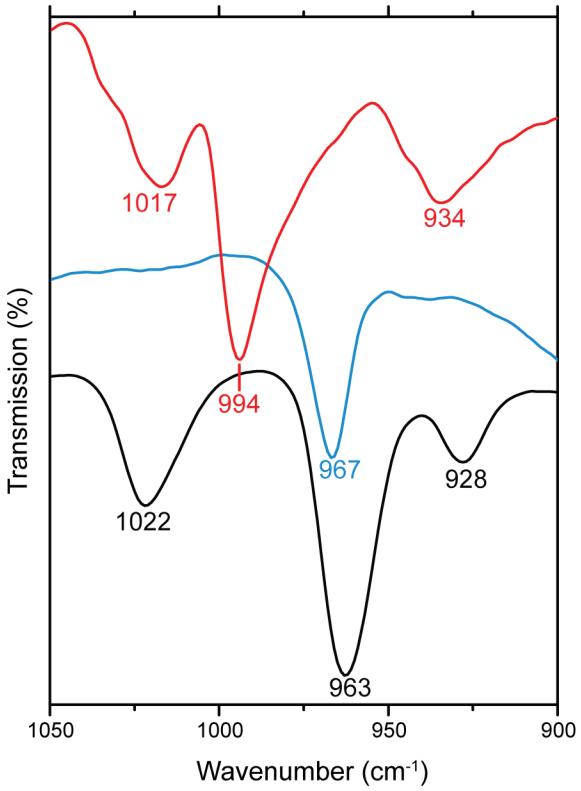

Figure A.6: FT-IR spectra of vanadyl acetylacetonate (red), oleylamine (blue), and a mixture of 1 mmol vanadyl acetylacetonate and 4 mmol oleylamine stirred at room temperature until completely dissolved (black). The V=O stretch peak, originally located at 994 cm^{-1} in vanadyl acetylacetonate, shifts to either lower or higher wavenumber in the oleylamine mixture (963 cm^{-1} or 1022 cm^{-1}). This is evidence of a change in ligand binding environment surrounding the vanadyl ion, therefore supporting the hypothesis that oleylamine and vanadyl acetylacetonate form a complex in solution. The peak at 1017 cm^{-1} in the vanadyl acetylacetonate can be indexed to the CH_3 rocking absorption, the peak at 967 cm^{-1} in the oleylamine is the C-H out of plane bend in C=C-H, and the peaks at 934 and 928 cm^{-1} is the C-CH_3 stretch.

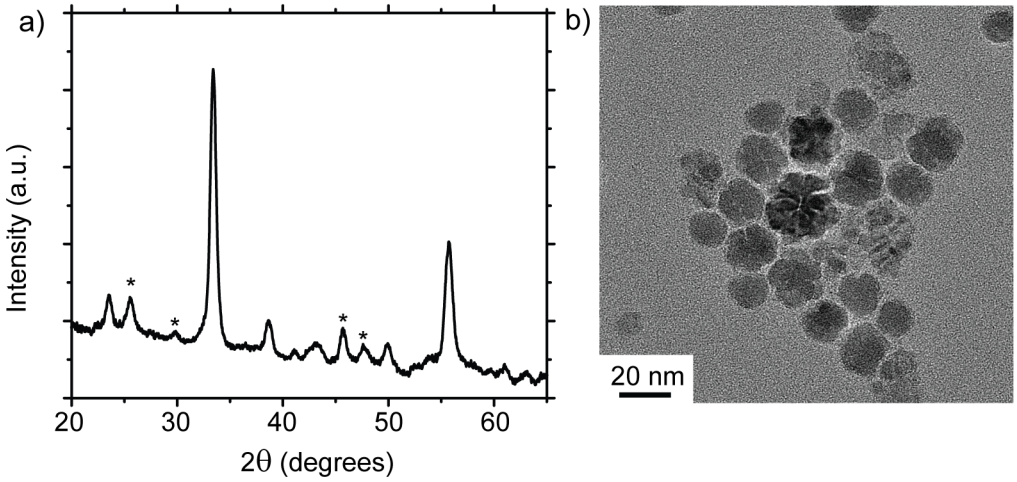

Figure A.7: a) XRD pattern and b) TEM image of nanocrystals synthesized with 2 mmol oleic acid and 2 mmol oleylamine. The nanocrystal morphology and size do not appear to be different than those made using 4 mmol oleic acid and 4 mmol oleylamine. An impurity phase (*) evident in the XRD scan can be indexed to the metastable VO_2-A phase. The data was modeled using the program Crystal Diffract and was found to contain approximately 75% bixbyite phase and 25% VO_2-A phase.

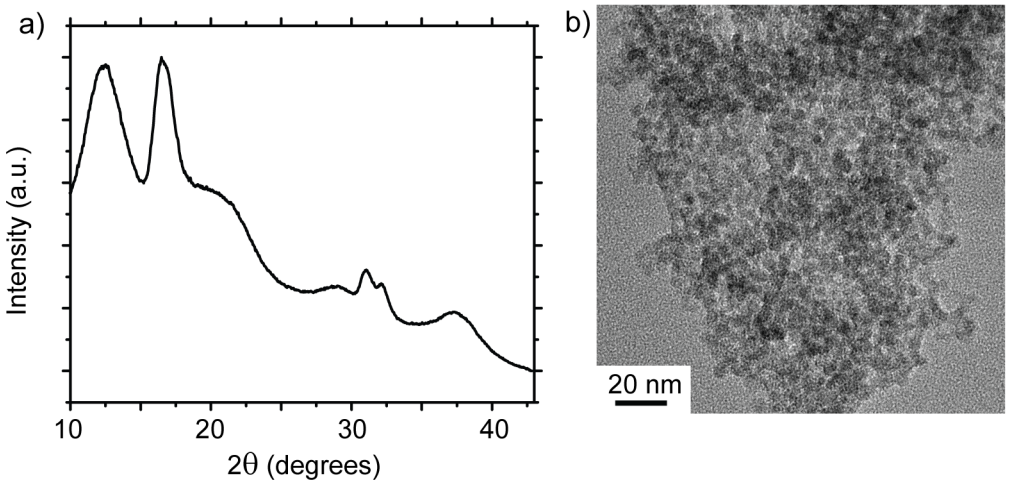

Figure A.8: a) XRD scan and b) TEM image of nanocrystals synthesized using 4 mmol oleylamine and no oleic acid. The XRD scan cannot be indexed to any known phase. The TEM shows a network of small (~5 nm) nanocrystals.

Table A.1: Rietveld Refinement Parameters and Results

Crystal Dimensions	5-30 nm
Crystal System	Cubic
Space Group	Ia-3
Unit Cell Dimensions	a=9.36337(8) Å
Unit Cell Volume	830.911(22) $Å^3$
Calculated Density	4.852 g/cm3
2θ Range	15-80°
Radiation	Cu Kα 1+2
Wavelength	1.541 Å
Temperature of Measurement	25°C
Absorption Corrections Performed?	yes
Method of Refinement and Program	GSAS + EXPGUI
Number of Refined Parameters	14
R_p	1.75%
R_{wp}	2.31%
χ^2	2.339

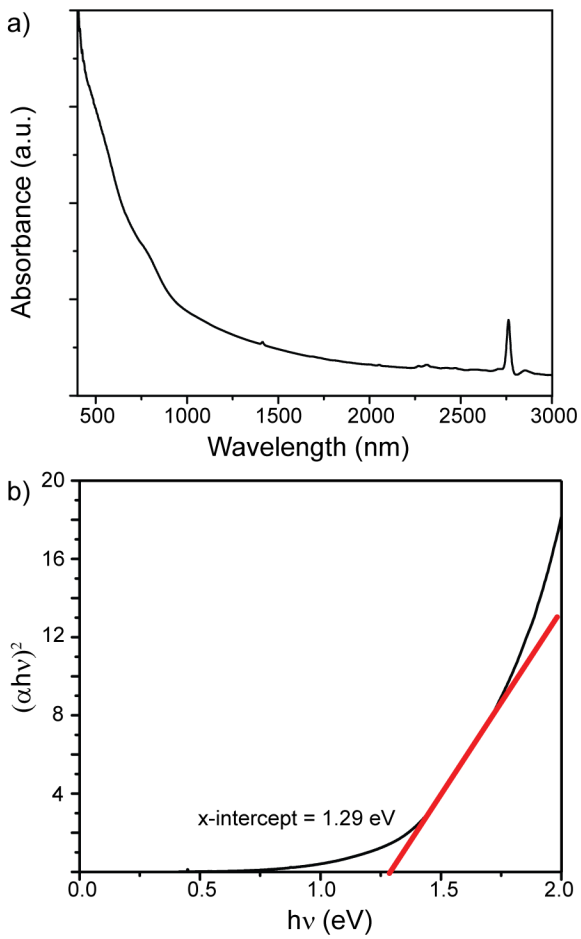

Figure A.9: a) UV-Vis spectra of bixbyite nanocrystals suspended in tetrachloroethylene. b) $(\alpha h\nu)^2$ plotted versus energy in order to determine the direct band gap, which was found to be 1.29 eV.

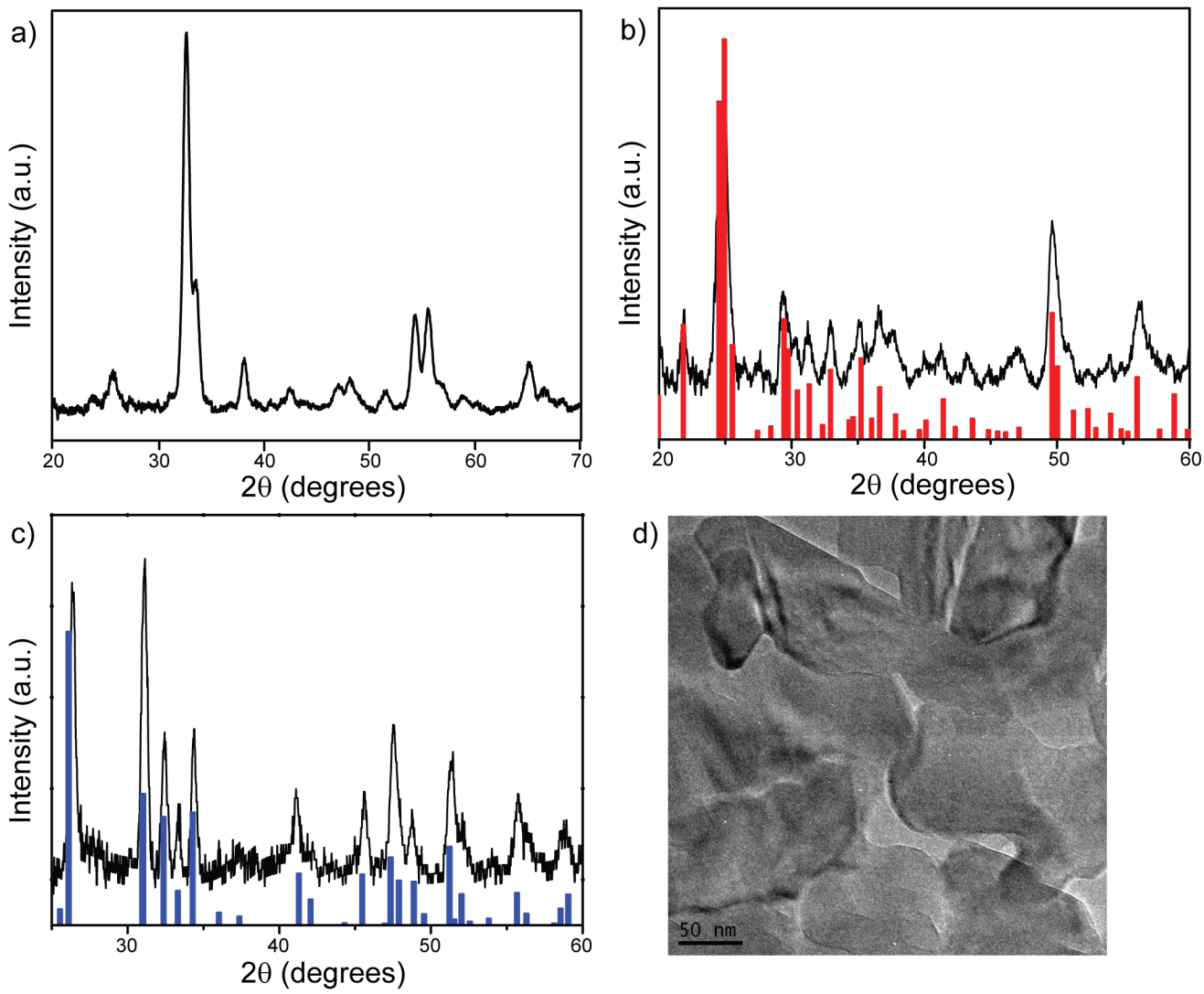

Figure A.10: XRD patterns of bixbyite nanocrystals after annealing in air for a) 12 hours 100°C and for 30 minutes at b) 300°C, and c) 400°C. The red and blue lines indicate the position of the XRD peaks for V_3O_7 and V_2O_5, respectively. No further oxidation occurs above 400°C. d) TEM image of bixbyite nanocrystals on SiN grid after annealing at 400°C for 30 minutes (see Figure 2c for TEM of as-deposited nanocrystals).

This appendix includes TEM, XRD, and size histograms of nanocrystals in differing states of oxidation, Rietveld refinement, a description of how transformation time is determined, and additional *in situ* XRD and TGA of the reduction process. The theoretical section includes information on how density functional theory was performed, initial parameter testing of exchange correlation functional, Hubbard U value, and magnetic ordering, as well as a description of the use of the Birch Murnaghan equation to determine equilibrium energy and volume.

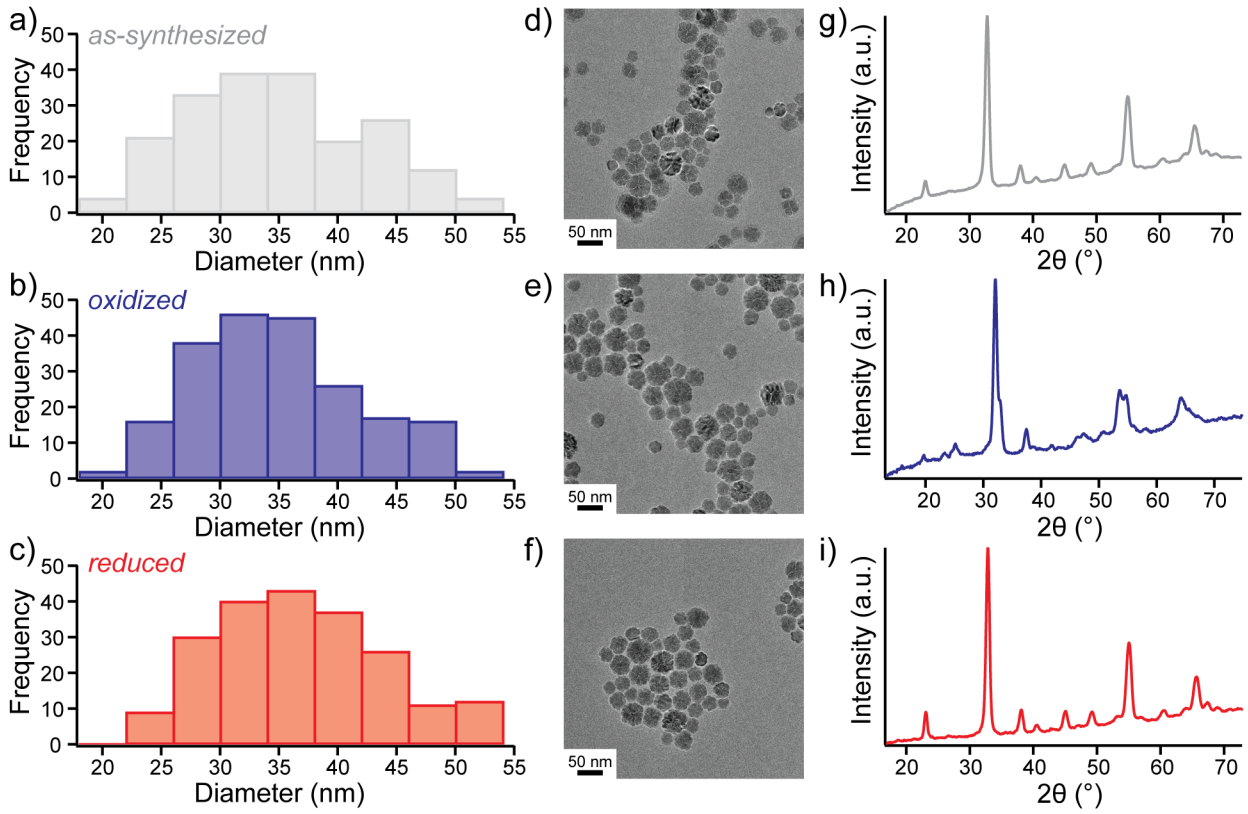

Figure B.1: Size distribution histograms, representative TEM images, and XRD patterns of as-synthesized NCs (a,d,g), NCs oxidized in air at 125°C for 2 hours (b,e,h), and NCs reduced after oxidation by annealing in nitrogen at 325°C for 1 hour (c,f,i). The average NC diameter of each sample is 31.0 ± 6.9 nm, 31.0 ± 7.5 nm, and 33.1 ± 7.4 nm, respectively, with over 200 NCs measured by TEM for each.

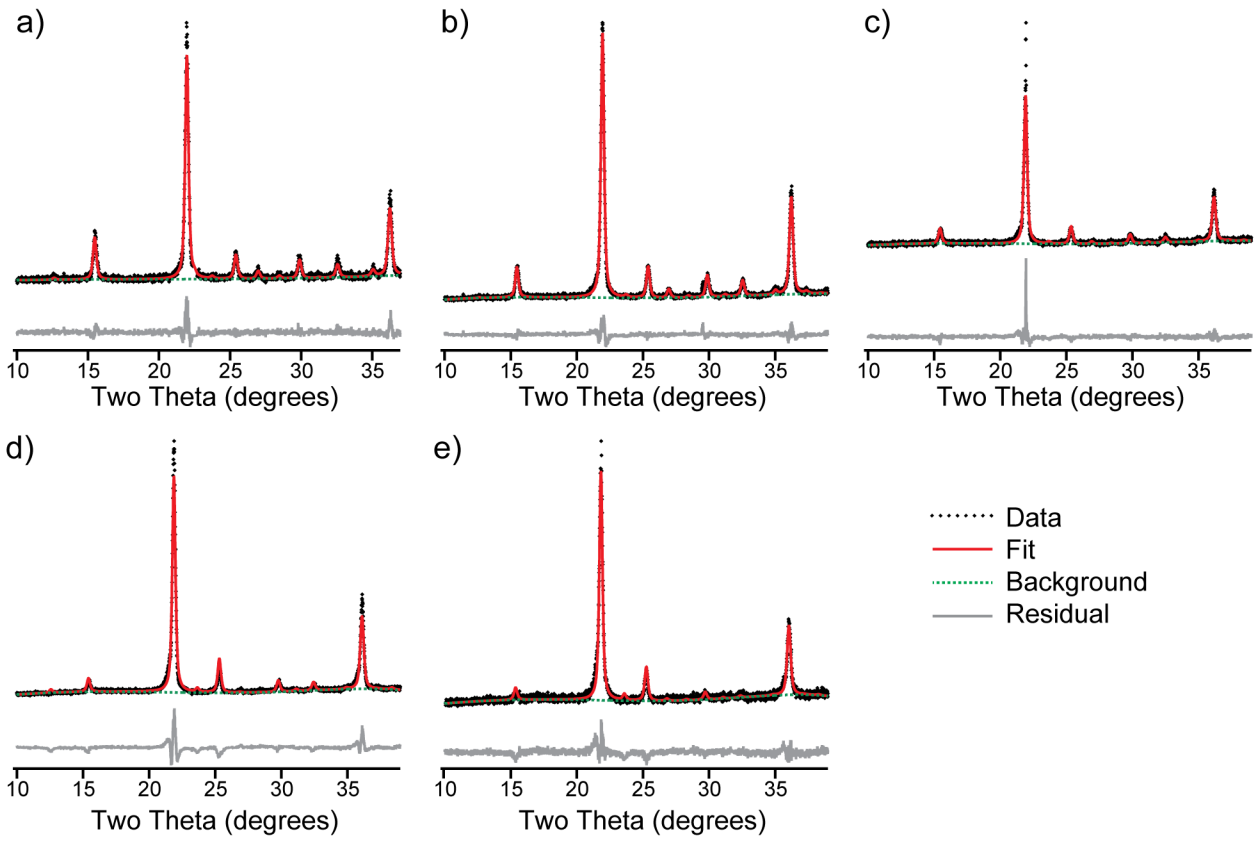

Figure B.2: Rietveld refinement fits and residuals for samples annealed in air at 125°C for a) 0, b) 10, c) 20, d) 30, and e) 40 minutes.

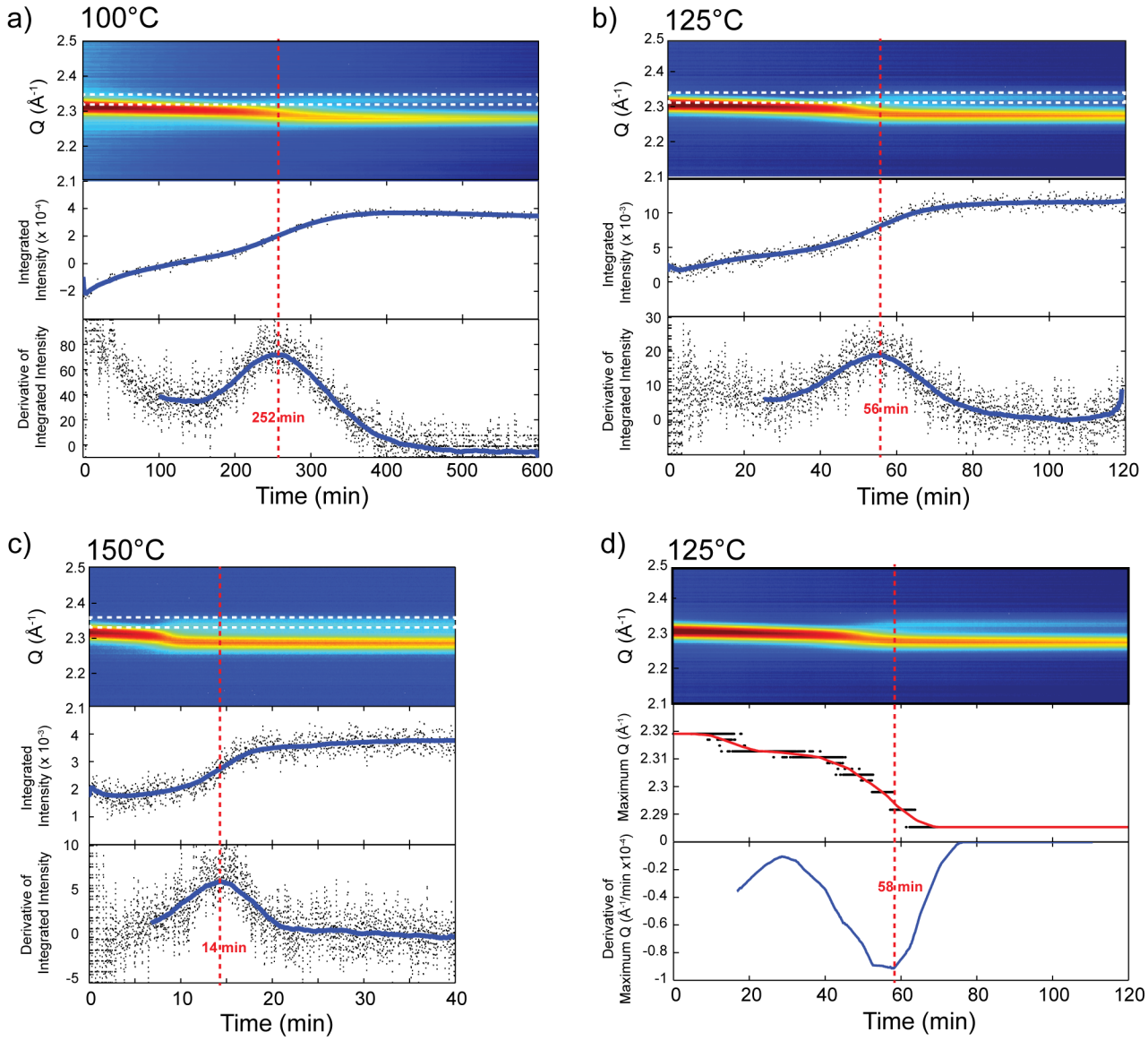

Figure B.3: Determination of transformation time from maximum first derivative of shoulder peak intensity (area between white dotted lines) with respect to time for isotherms at a) 100°C, b) 125°C, and c) 150°C. d) Transformation time could also be determined from the minimum first derivative of peak position with respect to time as shown for the isotherm at 125°C. Both methods yield similar results.

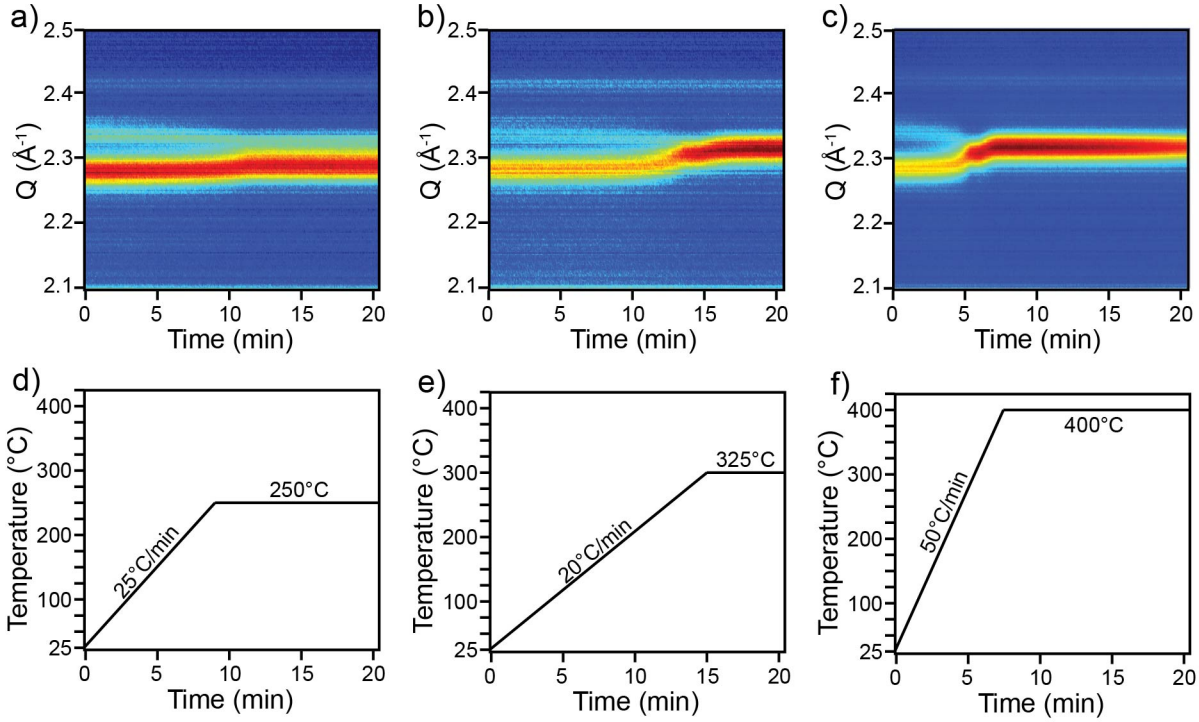

Figure B.4: Reduction of oxidized bixbyite as observed by *in situ* XRD under helium flow (a, b, and c) and corresponding temperature profiles (d, e, and f). The peak present at ~2.1 and 2.42 $Å^{-1}$ in all samples is from the beryllium dome.

The figure above shows *in situ* XRD scans from an already oxidized and transformed sample heated under helium flow at 250, 325, and 400°C. The characteristic peak and shoulder of the unknown phase merge into one peak, characteristic of the bixbyite phase. The position of the peak after reduction is dependent on temperature, with higher temperatures resulting in peak positions closer to that of stoichiometric bixbyite and faster reduction kinetics.

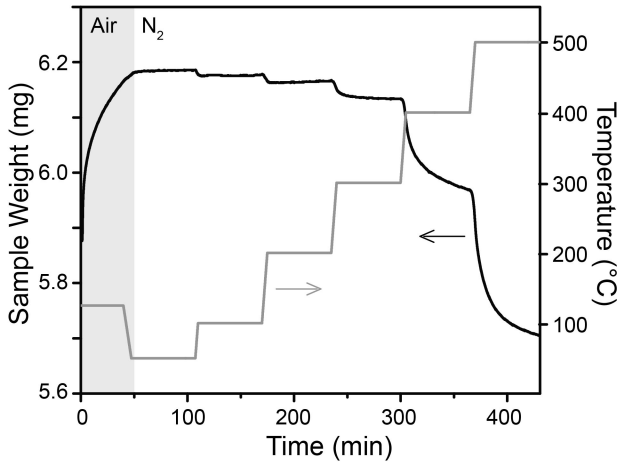

Figure B.5: TGA scan showing initial oxidation (125°C for 50 min) followed by reduction of bixbyite NCs. Weight loss was measured (left axis) as temperature was increased by intervals of 100°C up to 500°C, with the temperature shown on right axis. Ligands were decomposed prior to TGA scan, by annealing in a tube furnace at 400°C for 2 hours in nitrogen.

Under nitrogen flow, weight loss was measured as temperature was increased by steps of 100°C. Initial weight loss at 100 and 200°C is minimal, but increases with temperature such that the largest decrease in weight occurs at 500°C. The equilibrium concentration of oxygen interstitials is clearly dependent on both atmosphere and temperature, with higher temperatures resulting in lower oxygen interstitial content during the reduction process in inert gas.

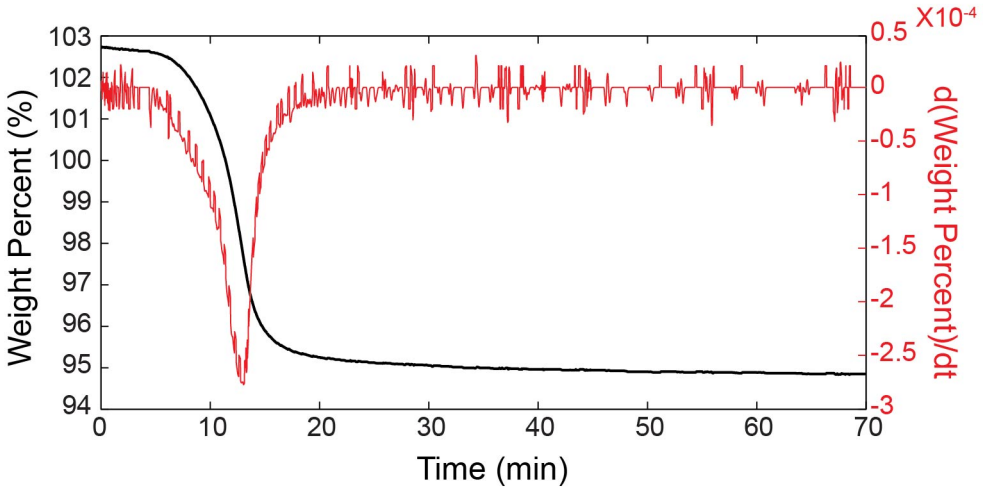

Figure B.6: Weight percentage (black/left) and derivative of weight percentage with respect to time (red/right) as a function of time while heating in nitrogen to 325°C. The maximum change in weight occurs at approximately 13 minutes, at which point the temperature is still ramping and is equal to 310°C. This is the same time at which a rapid change in lattice parameter is observed by *in situ* XRD, and thus, likely corresponds to a point at which a large amount of oxygen exits the lattice.

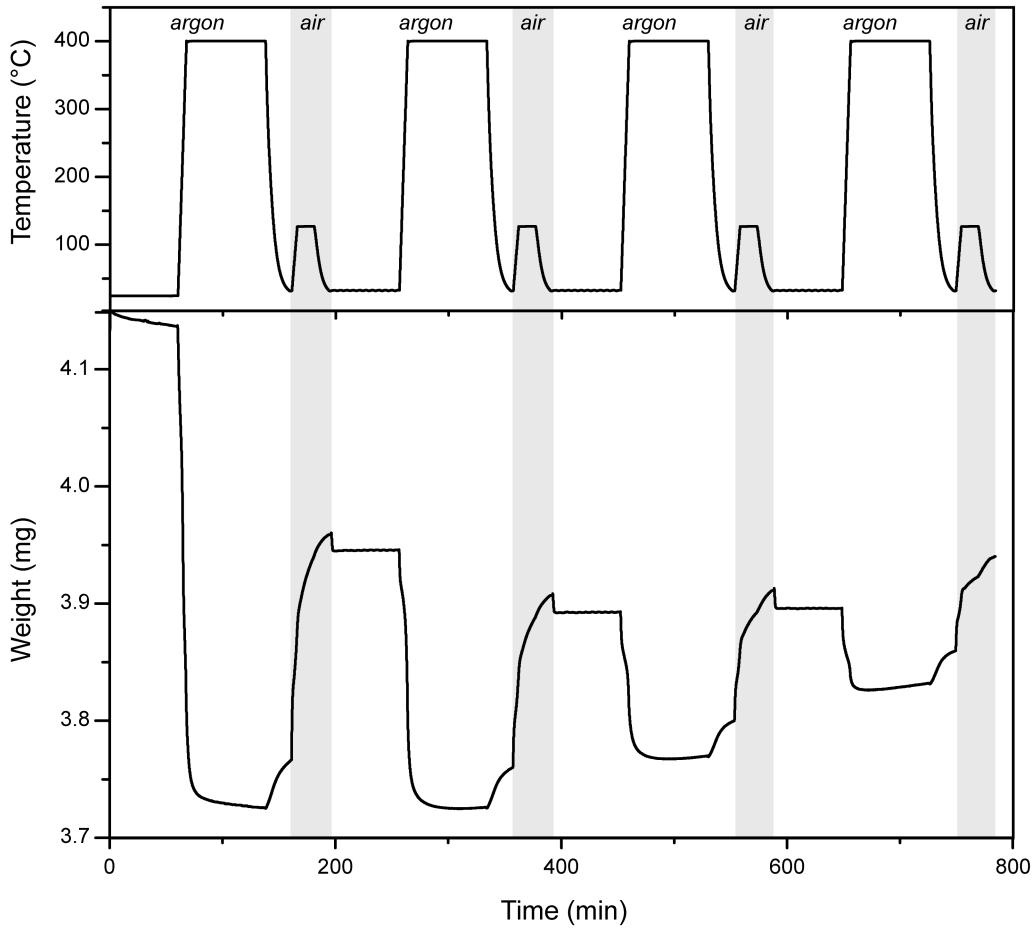

Figure B.7: TGA scan while cycling between argon flow at 400°C and air flow at 125°C with large initial weight loss due to ligand decomposition.

Table B.1: Exchange Correlation Functional Testing

	Volume (Å^3)			Band Gap (eV)			ΔE_0/f.u. vs. monoclinic (eV)		
Functional	Mon.	Cor.	Bix.	Mon.	Cor.	Bix.	Mon.	Cor.	Bix.
PBEsol (V_pv)	*202.75*	306.01	*841.13*	*0.285*	0.032	*0.155*	*0*	*0.067*	*0.071*
PBEsol (V_sv)	*202.32*	305.29	*839.37*	*0.293*	0.035	*0.155*	*0*	*0.069*	*0.079*
PBE	210.91	318.18	871.70	*0.666*	0.086	*0.532*	*0*	0.057	-0.003
PW	210.04	316.79	*868.96*	*0.562*	*0.007*	*0.432*	*0*	0.056	0.004
LDA	*194.37*	*294.51*	*803.16*	0.029	0.026	0.003	*0*	*0.100*	*0.184*
experiment	199.94	296.94	829.68	0.6	0	>0	0	>0	>cor.

A variety of exchange correlation functionals and pseudopotentials were tested to determine the one that most closely matched experimental values. The PBEsol and LDA functionals were found to perform the best with respect to unit cell volumes, with the results within ±5% of experiment italicized. These two functionals also described the energetics correctly, with monoclinic phase having the lowest energy per formula unit, followed by corundum phase, then finally bixbyite. However, the functionals which performed well with respect to volume and energy failed to describe the electronic properties of the materials correctly. At the very least, the semiconducting monoclinic and bixbyite phases should have a band gap greater than zero, and the metallic corundum phase should have a band gap of zero. The functionals satisfying these conditions are italicized, with the PW functional performing best. The PBEsol functional with V_sv pseudopotential was chosen for the remainder of the calculations, as structure and energetics are most important for this study. This testing was done with spin polarization for all phases and an antiferromagnetic moment set for the monoclinic phase, but not yet for bixbyite.[168] The U and J values used here were U=2.8 and J=0.93, values which have been used in previously in the literature.[169]

Table B.2: Magnetic Ordering in Bixbyite

Ordering		Volume (Å^3)	Band Gap (eV)	ΔE_0 (eV)
No spin polarization		772.25	0.000	-668.25
Ferromagnetic		839.37	0.155	-702.91
Antiferromagnetic	a	832.99	0.661	-704.14
	b	833.11	0.653	-704.19
	c	833.65	0.166	-703.35
	d	833.94	0.608	-704.00
Experiment		829.68	>0	

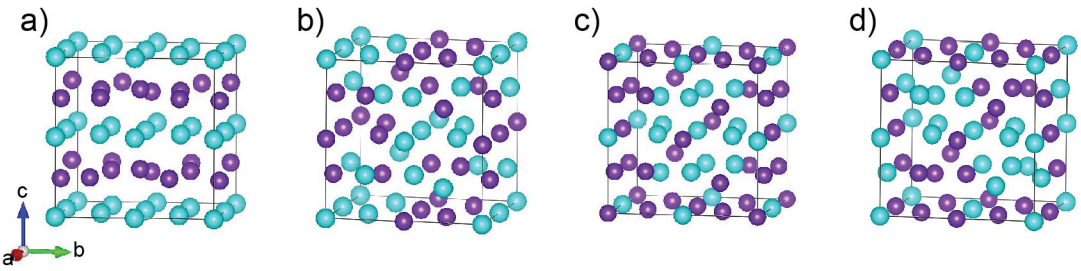

Antiferromagnetic ordering in bixbyite yields the largest band gaps and lowest energies. Several collinear orderings were tested, and the ones which converged are listed in Table B.2 and the subsequent figure, with blue atoms representing spin up and purple representing spin down. The ordering with the lowest overall energy, labeled b, was chosen. These tests were done with U and J values of 2.8 and 0.93, respectively. The chosen ordering is such that all nearest neighbor vanadium atoms in d-sites have opposing spins.

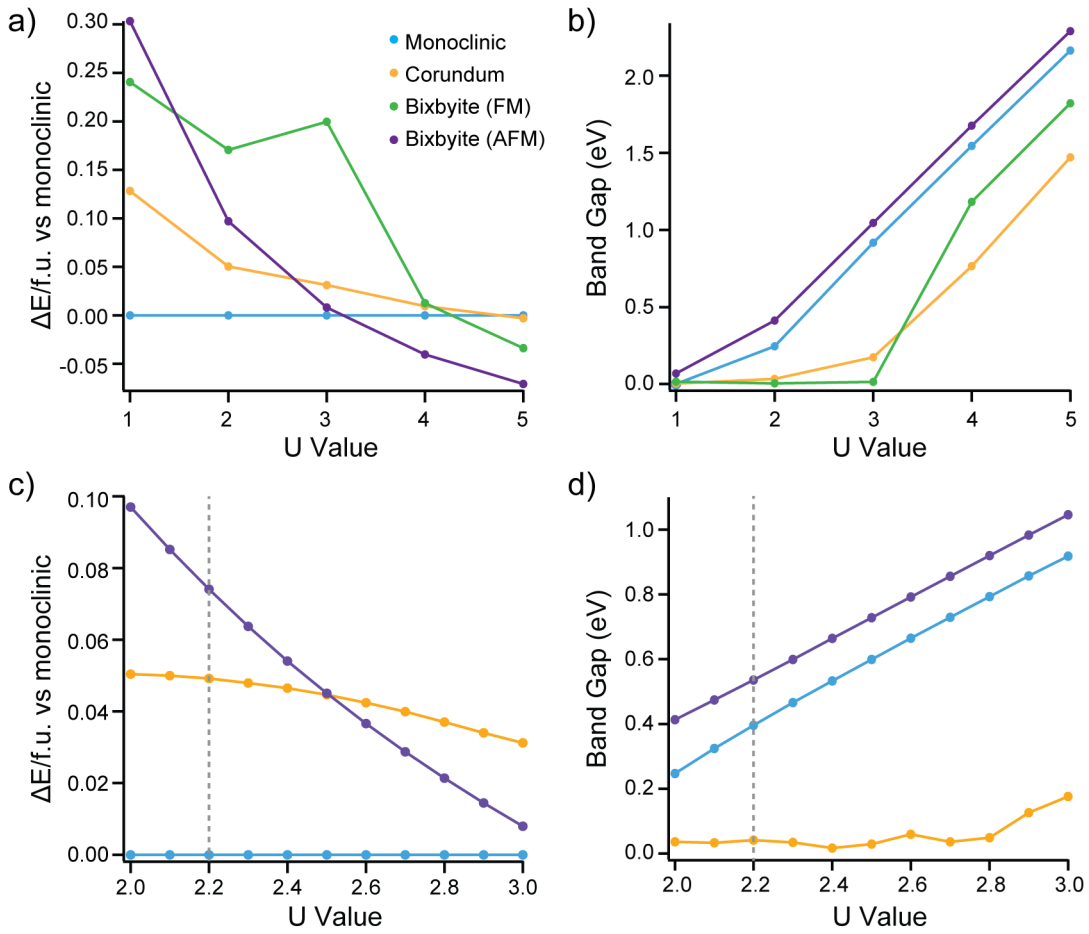

Figure B.8: a) The change in energy per formula unit versus the monoclinic phase and b) band gap plotted as a function of U value, with finer detail in c) and d)

When antiferromagnetic ordering is imposed on the bixbyite phase, its energy becomes lower than that of the monoclinic phase and thus its metastable nature is no longer described accurately. In order to remedy this, the U value correction scheme was further tested. The Liechtenstein scheme, where both U and J values are assigned, was ruled out after failing to describe the system at any combination of values. Thus a Dudarev scheme, requiring a single U value, was utilized instead. Polymorph stability (a) and band gap (b) were first determined over a coarse range of Dudarev-type U values between 1 and 5. In terms of polymorph stability, monoclinic phase should have the lowest energy, followed by corundum phase then bixbyite. This is true for values below 4 in the case of bixbyite without antiferromagnetic (AFM) ordering and below 3 for bixbyite with AFM ordering. Furthermore, U must be kept below 3 to accurately describe the metallic nature of corundum phase, however this also results in a band gap of zero for bixbyite without AFM ordering. Therefore, AFM ordering in bixbyite is not only favored energetically relative to bixbyite without AFM ordering, it is necessary to concurrently describe the electronic structure of corundum and bixbyite.

The analysis was repeated for U values between 2 and 3. Corundum should have a band gap of zero, ruling out U values above 2.8. U values of 2.5 and greater are ruled out because

bixbyite becomes more stable than corundum at these values. The monoclinic phase's band gap of 0.6 eV is matched at U=2.5, but this does not describe the energetics well. In order to best describe both energetics and band gap, the value of U=2.2 was chosen.

It is worth noting here that this is the first instance in which a U value of 2.2 eV is used to describe the vanadium sesquioxide system. In many papers, the U and J values of 2.8 and 0.93 eV are utilized. However these values no longer accurately describe the system when the bxibyite phase and its antiferromagnetic ordering are included. A vanadium U value of 3.25 eV, determined by fitting experimental binary formation enthalpies, was previously suggested by Wang *et al.*[121] Again, this fails to describe the system when used in conjunction with the PBEsol functional as it results in a non-zero band gap in corundum.

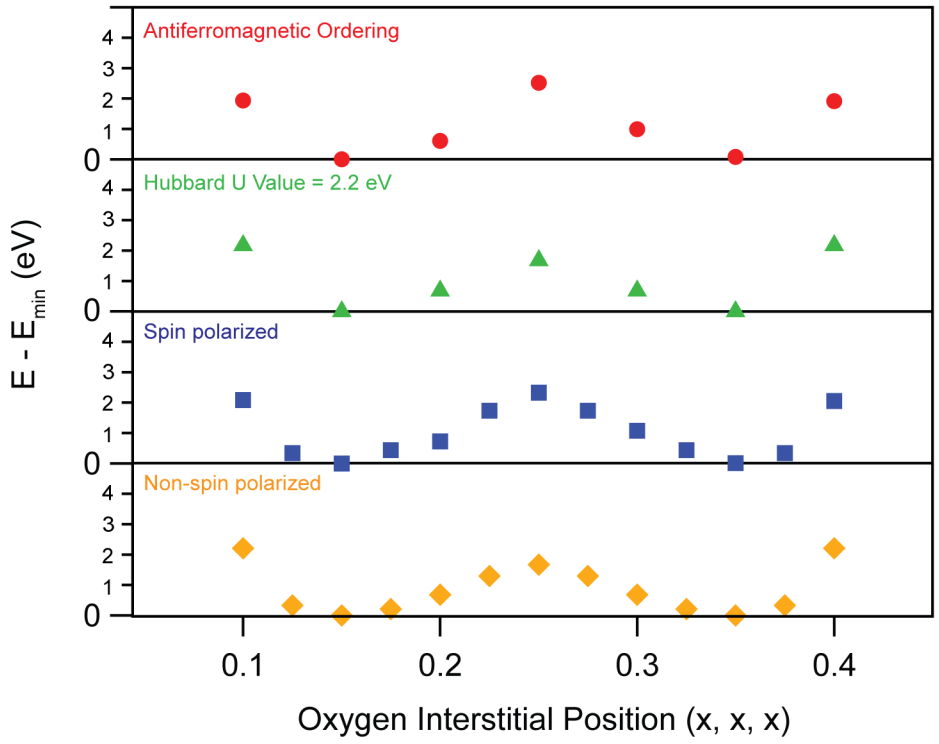

Figure B.9: Oxygen interstitial mapping along the body diagonal of the bixbyite lattice using different DFT parameters

This analysis was done in Figure 3.3 without spin polarization and with a different U and J value than was used for the rest of the analysis (U=2.8 and J=0.93 rather than U=2.2). Therefore, this analysis was repeated with spin polarization, antiferromagnetic ordering, and the U value of 2.2 eV for the case of interstitials placed along the body diagonal. The resulting energies (relative to the minimum energy value) are quite similar, with minima occurring at (0.15, 0.15, 0.15) and (0.35, 0.35, 0.35) in all cases.

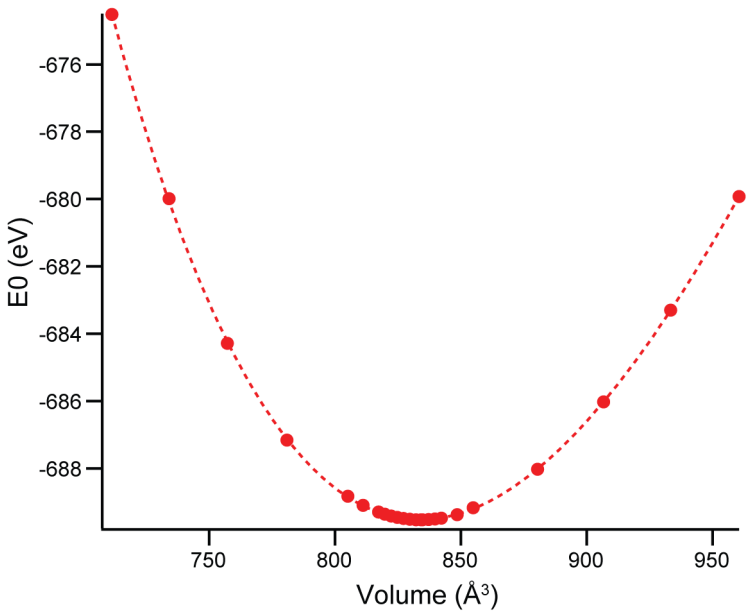

Figure B.10: Bixbyite unit cell energy as a function of volume. The data was fit to the Birch Murnaghan equation (dashed line) using the parameters in Table B.3. A U value of 2.2 eV was used in this analysis.

Table B.3: Birch Murnaghan Fitting Parameters

Parameters	Value
E_0 (eV)	-689.52
V_0 (Å^3)	834.19 ± 0.0307
B_0 (eV/Å^3)	1.29
B_0' (dB/dP)	4.78

To determine the equilibrium lattice parameter of the cubic bixbyite unit cell, the Birch Murnaghan equation was employed[114]:

$$E(V) = E_0 + \frac{9V_0B_0}{16}\left\{\left[\left(\frac{V_0}{V}\right)^{2/3} - 1\right]^3 B_0' + \left[\left(\frac{V_0}{V}\right)^{2/3} - 1\right]^2 \left[6 - 4\left(\frac{V_0}{V}\right)^{2/3}\right]\right\}$$

Where E_0 is the equilibrium energy of the cell, V_0 is the equilibrium volume, B_0 is the elastic modulus, and B_0' is the derivative of elastic modulus with respect to volume. Cell volume, V, was fixed and ion positions were relaxed, yielding cell energy, E. This was repeated for a range of volumes, and the resulting energy vs. volume curve was fit to the Birch Murnaghan equation to determine equilibrium volume and energy.

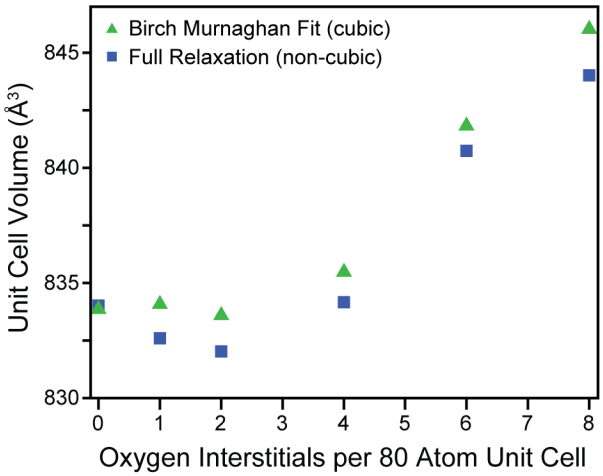

Figure B.11: Volume expansion as a function of oxygen interstitial concentration as calculated by DFT. A U value of 2.2 eV was used in this analysis.

The equilibrium unit cell volume of bixbyite with differing amounts of oxygen interstitials was obtained by full relaxation (leading to a subtle trigonal distortion) and by using a Birch Murnaghan fit to fix cubic shape (Figure B.10). At lower levels of oxygen interstitials, cell volume remains largely unchanged, while at higher levels, the volume rapidly increases. This non-linear trend agrees with experiment; however a larger number of oxygen interstitials is required before expansion occurs.

This appendix includes additional experimental methods and data pertaining to optical changes of VO_2 in lithium containing electrolyte and at 100°C, reversibility and cyclability of darkening and bleaching, comparison of optical changes in air vs argon and of nanocrystal vs planar films, and an EXAFS fit of unknown state to V_3O_5.

C.1.1 Planar Film Preparation

Planar films were prepared from vanadium oxide clusters previously described in the literature.[148] Briefly, ammonium metavanadate (0.5 mmol) (Sigma Aldrich, 99%) was dissolved in 12.5 mL of a 0.2 M oxalic acid solution (1:5 molar ratio) (Sigma Aldrich, 98%) and diluted to a total volume of 15.0 mL. Changing the volume of the oxalic solution added resulted in different vanadium oxide clusters (Figure C.7a). After stirring for 72 hours, the blue solution was concentrated to ~2 mL using nitrogen gas flow. Excess oxalic acid crashed out of the solution and was removed by filtration. The remaining solution was dried completely and a 75 mg/mL solution was prepared in a 90% ethanol, 10% water solution. The solution was then spin coated onto cleaned ITO or silicon substrates at 3000 rpm for 60 s followed by a drying spin at 4000 rpm for 30 s. Immediately following spin coating, films were placed on a 90°C hot plate for 2 min. The films were then annealed in a slightly oxidative environment (167-250 ppm O_2) at 525°C for 1 hour to produce a brown tinted VO_2 film (Figure C.7c), which was confirmed with XRD (Figure C.7d). Planar VO_2 film thickness was determined to be 71 nm.

C.1.2 Extended X-ray Absorption Fine Structure Fitting

The 'bleached' state, accessed by applying a -1.5 V potential to a VO_2 film at 100°C for 10 minutes, was shown by XANES to have a formally reduced vanadium charge ($< +4$), and is optically insulating. The Magnéli phase V_3O_5 (ICSD Coll. Code 16445) is known to be insulating at temperatures below 430 K, and was simulated to fit the EXAFS data collected for the bleached state.[170–172] Several other V-O Magnéli phases and VO_2 polymorphs were simulated to fit the EXAFS data for the bleached state, but no other phase was found to have

a physically meaningful R-factor fit below 0.10 while also demonstrating insulating behavior below 100°C.

EXAFS structural simulations were calculated using FEFF6 implemented in the IFEFFIT (1.2.11d) package of Artemis[173,174] from crystallographic information files obtained from ICSD Coll. Code 16445 (Figure C.9).[170] Fits were performed using simultaneous k^2 and k^3 weighting of the real component of the Fourier transforms across a fitting region of R=1-4 Å. The small dimensions and high likelihood of surface strain and defects in the nanocrystalline VO_2 films are expected to distort the mean free paths and thermal deviations in the EXAFS, so bounded constraints were placed on the mean-square radial displacement (i.e. Debye-Waller factor, σ^2), amplitude reduction factor ($S_0{}^2$) and 3rd cumulant to fit the EXAFS to the data with physically reasonable structural parameters. The simulated paths for V_3O_5 were generated using the Artemis package with the FEFF 'Aggregate' function, by generating paths from each of the four absorbing vanadium atoms in the structure and bundling the generated paths into a set of effective paths, using a 7.56 Å cluster. The coordination number was fixed using the calculated degeneracies from the FEFF path calculations, and the mean-free path deviations were fit using an isotropic expansion factor (α) for all paths to minimize the number of free parameters. Furthermore, the edge energy shift and amplitude reduction factor were both held constant across all paths. Experimental uncertainty was calculated by Artemis' built-in algorithm.

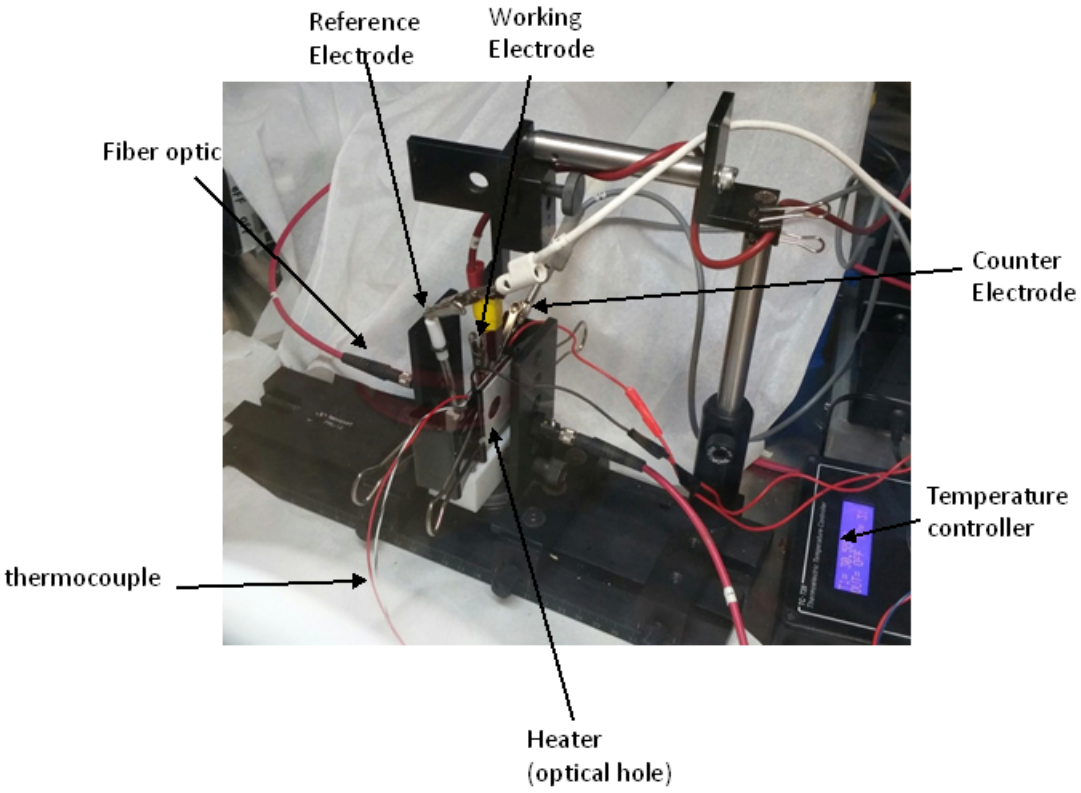

Figure C.1: Set-up used in VT-SEC experiments. The entire system was house in an argon glovebox to minimize any effects from oxygen and water. Experiments were also performed in an air environment (Figure C.6) by moving the entire SEC set-up out of the glovebox.

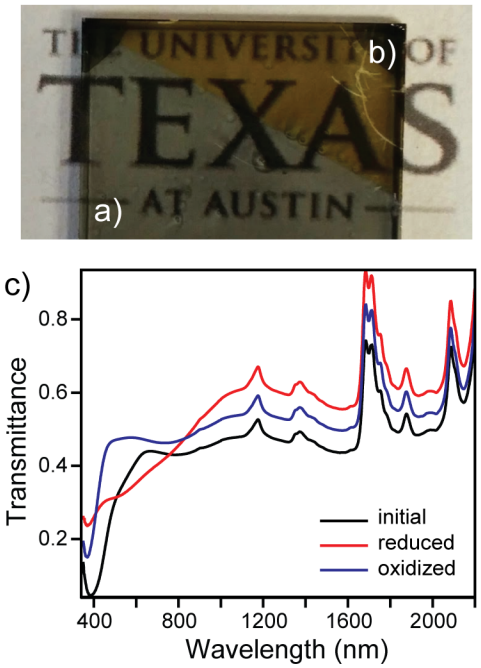

Figure C.2: Optical image of a VO_2 NC film a) with and b) without electrochemical reduction in an electrolyte consisting of 0.1M Li-TFSI. c) The electrochromic behavior in this case was irreversible as the Li^+ ions that intercalate into the VO_2 lattice are unable to deintercalate. Khan and co-workers observed similar behavior using ex-situ transmittance and conductivity measurements.[145]

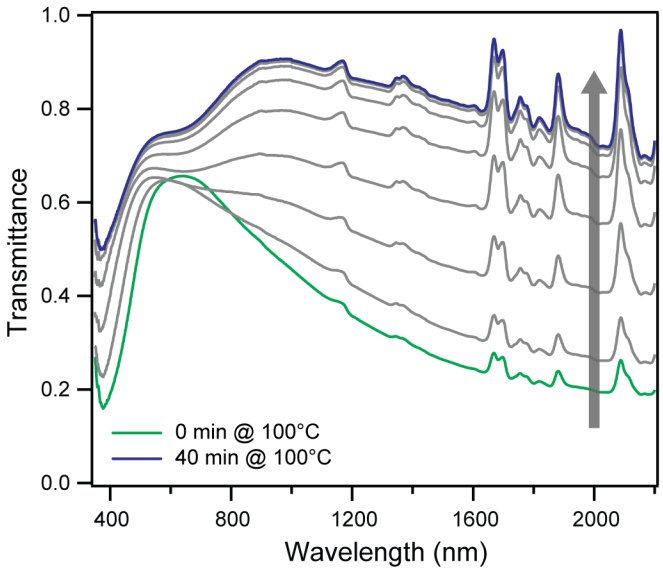

Figure C.3: Electrochromic behavior of VO_2 NC films at 100°C. Films were brought to the rutile phase thermally before applying a reducing potential with traces taken every 5 minutes until saturation. The bleaching in this case was achieved with much faster kinetics due to the increased rate of diffusion of oxygen out of the lattice and the conductive nature of the rutile NCs. Complete bleaching was observed after ≈40 minutes at -1.5 V vs NHE.

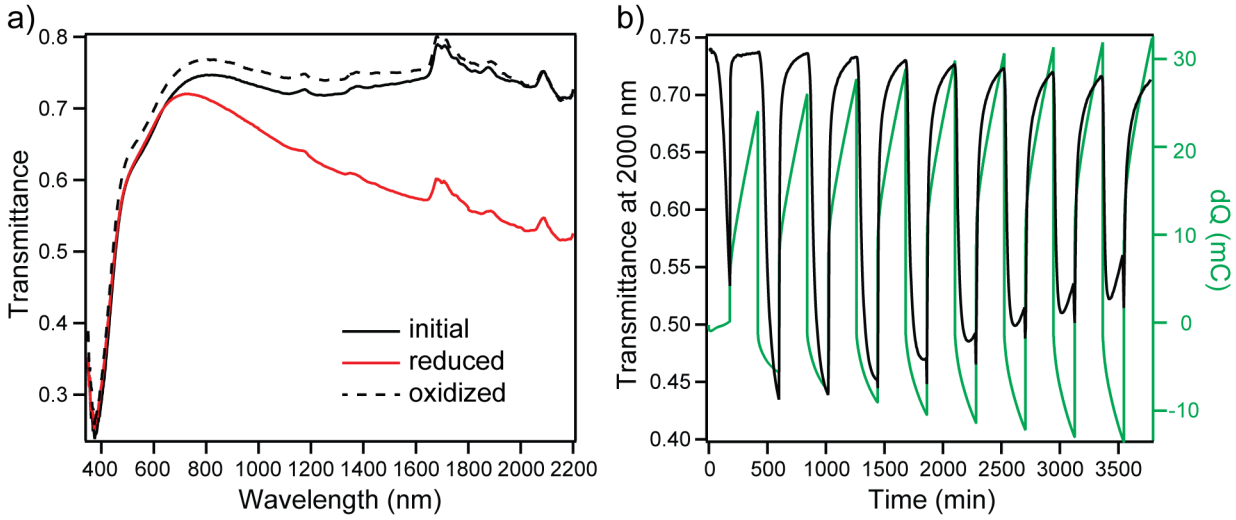

Figure C.4: a) Transmittance as a function of wavelength at 30°C showing initial monoclinic state, darkened state (reduced at -1 V for 3 hours), and recovered monoclinic state (oxidized at +1 V for 4 hours). b) Transmittance at 2000 nm and charge as a function of time as film is cycled between -1V vs NHE for 3 hours and +1V vs NHE for 4 hours at 30°C.

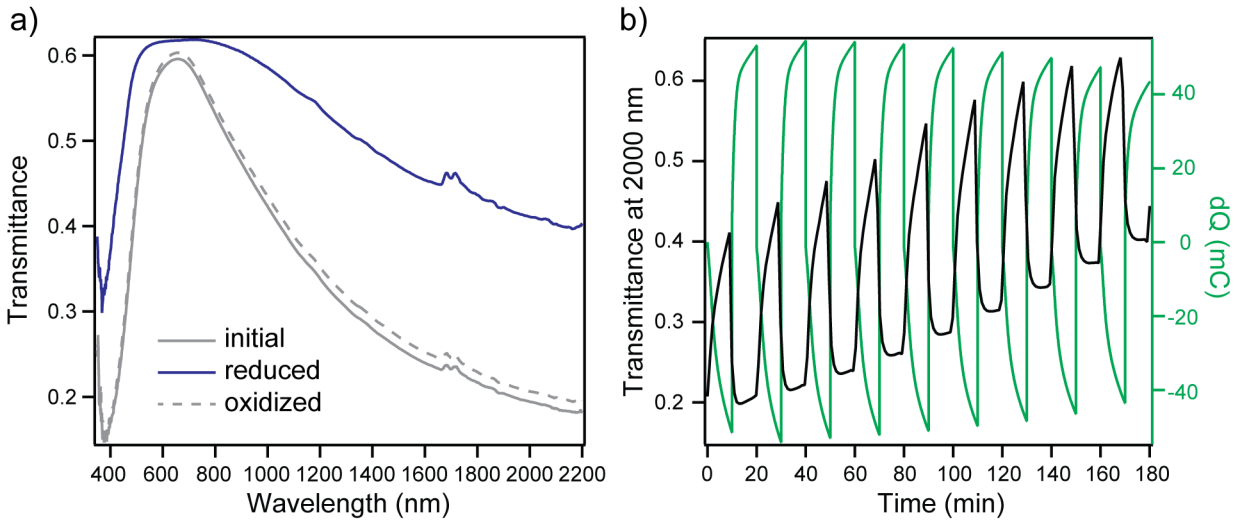

Figure C.5: a) Transmittance as a function of wavelength at 100°C showing initial rutile state, bleached state (reduced at -1.5 V for 10 min), and recovered rutile state (oxidized at +1 V for 10 min). b) Transmittance at 2000 nm as a function of time and charge as film is cycled between -1.5V and +1V vs NHE for 10 minutes each at 100°C.

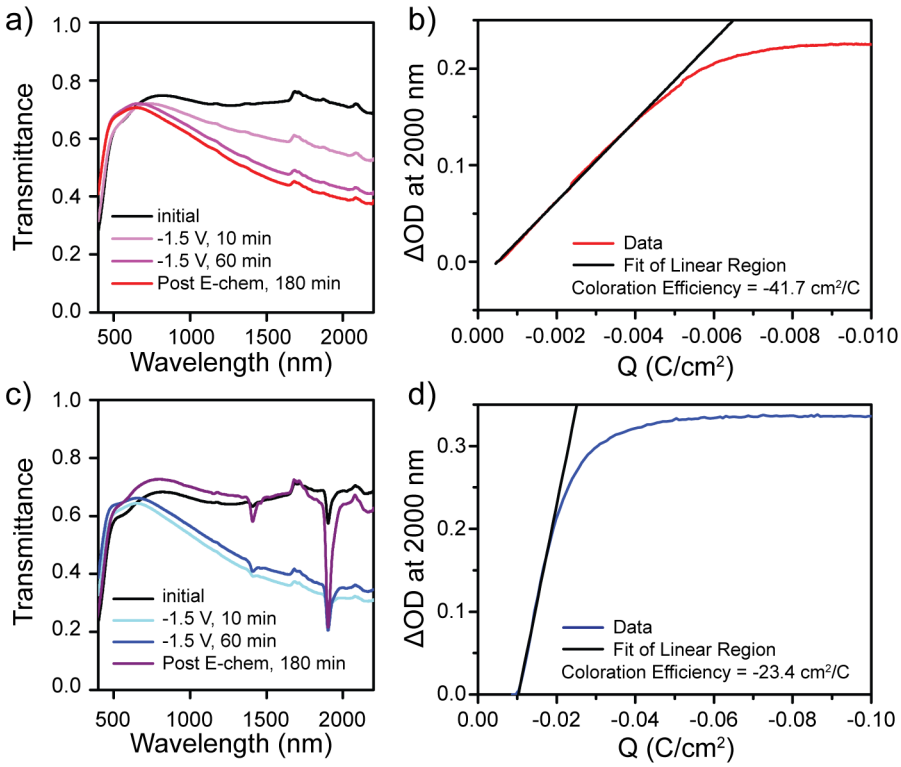

Figure C.6: Comparison of the electrochromic behavior of VO_2 NC films in an argon (a, b) and air (c, d) environment at 30°C. For experiments in an air environment, the 0.1M TBA-TFSI electrolyte was bubbled with air for 2 hours. The coloration efficiency was determined by taking the slope of the linear portion of the curve in parts b and d. While electrochromism was observed for films in both argon and air environments, when application of the reducing potential ended the NIR transmission slowly returned to its original state only in the air environment. We attribute this observation to the oxidation of the reduced state in the presence of oxygen. A lower coloration efficiency is calculated for the air environment as the oxygen is continuously oxidizing the film during the reduction process, consuming a large part of injected charge.

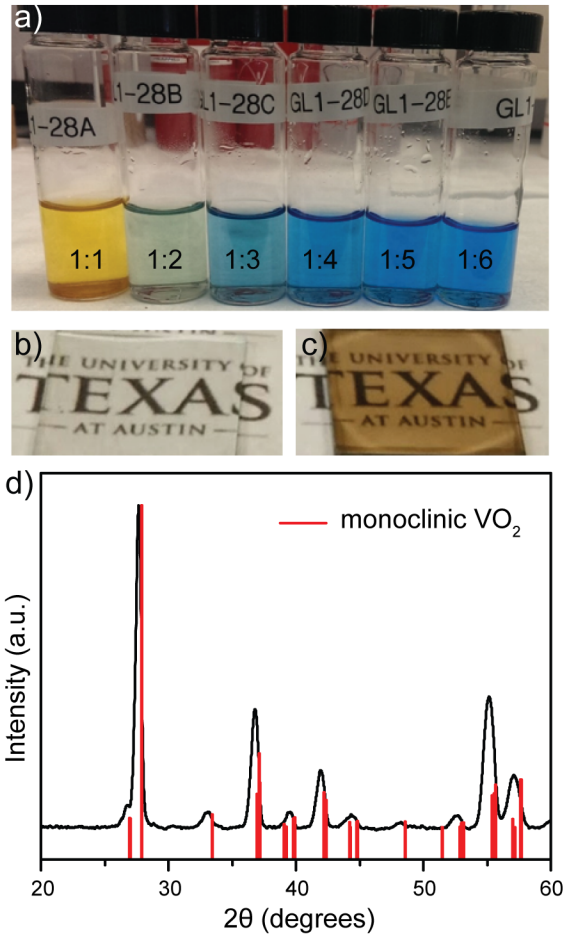

Figure C.7: Characterization of VO_2 films prepared from molecular clusters to generate planar films. a) Optical images of vanadium oxide molecular clusters prepared from noted ratios of ammonium metavanadate and oxalic acid. Films prepared on conductive substrates b) before and c) after annealing at 525°C under partial oxygen pressures. d) XRD scan after annealing confirming the monoclinic VO_2 structure.

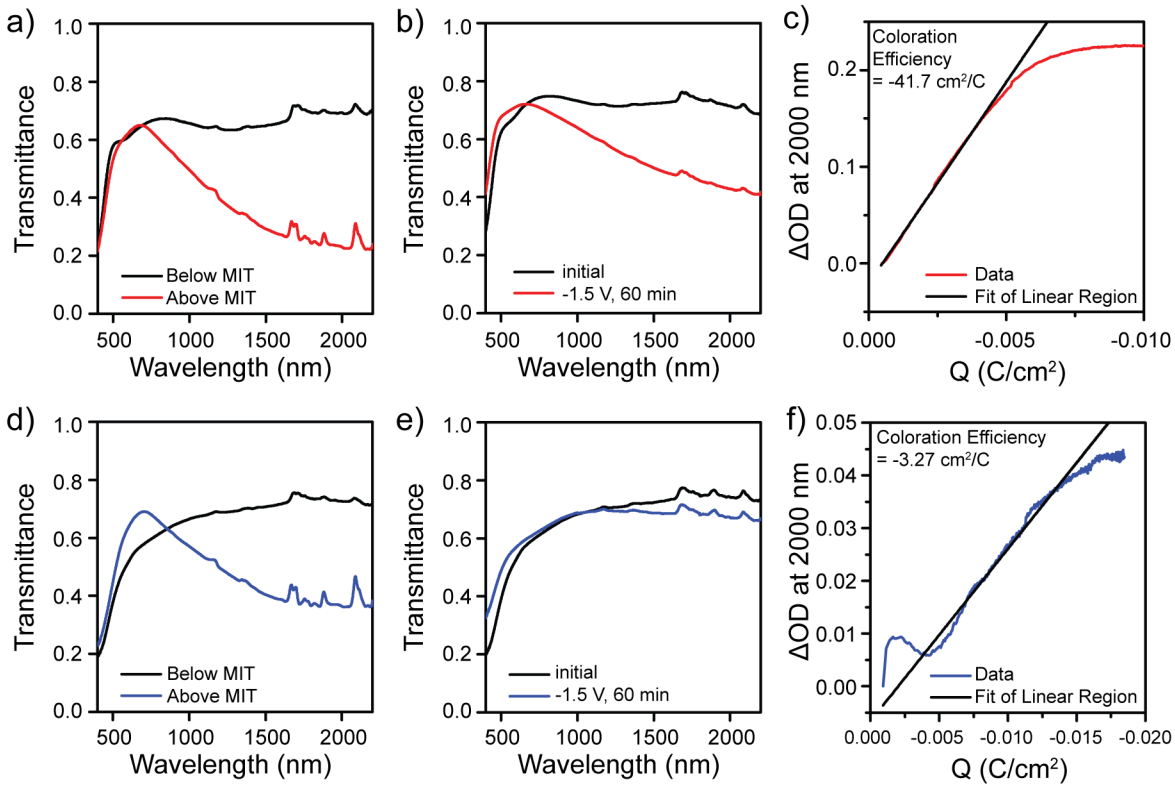

Figure C.8: Comparison of the thermochromic (a,d) and electrochromic (b,c,e,f) properties of nanocrystalline (a-c) and planar (d-f) VO_2 films. This data demonstrates the advantage of the nanostructured film as the increased surface area greatly enhances the gating effect.

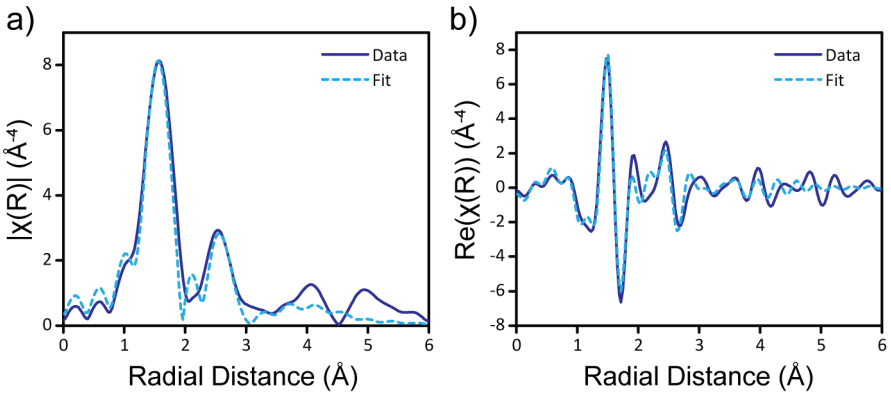

Figure C.9: EXAFS fits of V_3O_5 to the bleached state.

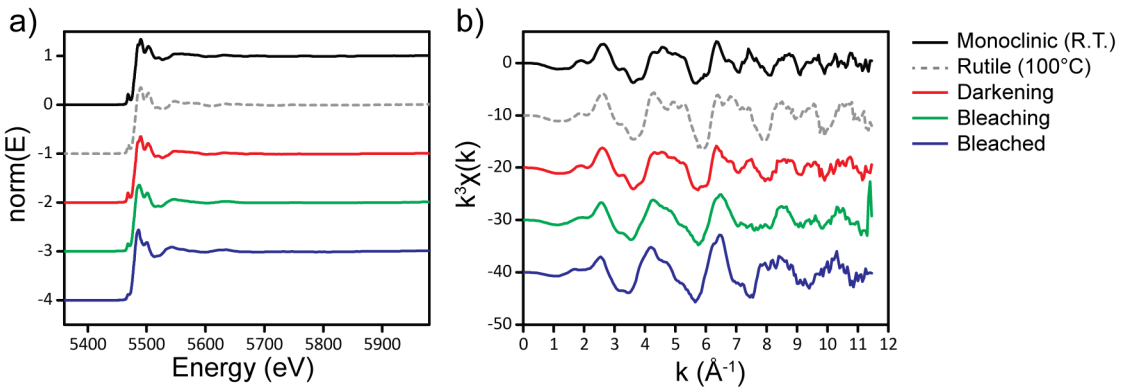

Figure C.10: Normalized XAS data and k^3 EXAFS data for monoclinic, rutile, darkening, bleaching, and bleached states.